Spring 2020

# Impact of turbulence models and shape parameterization on robust aerodynamic shape optimization

Aslihan Vuruskan



Department: Mechanical and Aerospace Engineering

# IMPACT OF TURBULENCE MODELS AND SHAPE PARAMETERIZATION ON ROBUST AERODYNAMIC SHAPE OPTIMIZATION

by

ASLIHAN VURUSKAN

A DISSERTATION

Presented to the Graduate Faculty of the

MISSOURI UNIVERSITY OF SCIENCE AND TECHNOLOGY

In Partial Fulfillment of the Requirements for the Degree

DOCTOR OF PHILOSOPHY

in

AEROSPACE ENGINEERING

2020

Approved by:

Dr. Serhat Hosder, Advisor
Dr. Kakkattukuzhy M. Isaac
Dr. David Riggins
Dr. Leifur Leifsson
Dr. Xiaoping Du

# ABSTRACT

Aerodynamic design optimization is typically performed at fixed flight conditions, without considering the variation and uncertainty in operating conditions. The objective of robust aerodynamic optimization is to design an aerodynamic configuration, which will keep its optimum performance under varying conditions such as the speed of aircraft. The primary goal of this study was to investigate the impact of turbulence models used in RANS simulations on the 2-D airfoil and 3-D wing designs obtained with gradient-based deterministic and robust optimization in transonic, viscous, turbulent flows. The main contribution of this research to the aerodynamic design area was to quantify the impact of turbulence models (Spalart-Allmaras and Menter's Shear Stress Transport) and shape parameterization techniques (Hicks-Henne bump functions, B-Spline curves and Free-Form Deformation) on the computational cost, optimal shape, and its performance obtained with robust optimization under uncertainty. The effect of changing the relative weight of mean drag reduction and robustness measures used in the objective function was also investigated for the 3-D robust design. The robustness of the final design obtained with stochastic optimization approach was demonstrated over the Mach number range considered as the uncertain operating condition in this study. The results of the 2-D study show that the shape parameterization technique has a larger impact on the computational cost than the turbulence models in both deterministic and robust design. The results of the 3-D study show that the effect of the weight distribution in the objective function is more significant than the effect of turbulence model on the final design obtained with robust optimization below the design Mach number value. In general, robust optimization tends to reduce the impact of the turbulence model selection on the optimum shape and performance over the uncertain Mach number range considered, whereas the effect of the turbulence model becomes significant at off-design conditions for the optimal shapes obtained with deterministic design.

# ACKNOWLEDGMENTS

I would like to sincerely thank my advisor, Dr. Serhat Hosder, for his support, time and patience throughout my entire graduate school career at Missouri University of Science and Technology. I would like to express my gratitude for the highest guidance and dedication Dr. Hosder provided to evolve me into a better researcher. I am very grateful for the opportunity he has provided by working with me and sharing his experience and expertise.

I would like to thank my committee members, Dr. Kakkattukuzhy M. Isaac, Dr. David Riggins, Dr. Xiaoping Du, and Dr. Leifur Leifsson, for their time, dedication and support to this research. I also would like to thank my fellow graduate students, Mario Santos, Andrew Hinkle and Martin Di Stefano, for their camaraderie.

I would like to thank the Department of Mechanical and Aerospace Engineering at the Missouri University of Science and Technology for providing the facilities, funding and educational opportunity. I would like to thank NASA for providing the funding for this research (Grant Number NNX14AN17A). It has been a great honor and pleasure to be awarded with a prestigious Amelia Earhart Fellowship by Zonta International Foundation. I would also like to thank Dr. Thomas Economon for his help and guidance on the SU2 Open-Source CFD code used in this study.

Finally, I sincerely thank my family and friends for their love, joy, patience and support. I have been very grateful to have these nameless heroes in this challenging and long journey and in my life.

# TABLE OF CONTENTS

Page

# LIST OF ILLUSTRATIONS

Figure Page

# LIST OF TABLES

# NOMENCLATURE

| Symbol | Description |
|---|---|
| $C_D$ | Drag coefficient |
| $C_L$ | Lift coefficient |
| $C_{L_{Target}}$ | Target lift coefficient |
| $C_p$ | Pressure coefficient |
| $M$ | Mach number |
| $N_s$ | Total number of samples |
| $n$ | Number of uncertain variables |
| $n_p$ | Oversampling ratio |
| $p$ | Order of response surface polynomial |
| $Re$ | Reynolds number |
| $x$ | Deterministic vector |
| $\alpha$ | Angle of attack |
| $\alpha^*$ | Stochastic response function |
| $\alpha_j$ | Deterministic component of $\alpha^*$ |
| $\mu_{C_D}$ | Mean of drag coefficient |
| $\mu_{C_{L_{Target}}}$ | Mean of target lift coefficient |
| $\xi$ | Random variable vector |

| | |
|---|---|
| $\sigma_{C_D}$ | Standard deviation of drag coefficient |
| $\sigma^2_{C_D}$ | Variance of drag coefficient |
| $\psi_j$ | Random variable basis function of $\alpha^*$ |
| $CRM$ | Common research model |
| $FFD$ | Free form deformation |
| $P_{i,j,k}$ | FFD box node |
| $B(x)$ | Bernstein polynomial |
| $W$ | Objective function weight |
| $C_{D_{ref}}$ | Drag coefficient reference factor |
| $C_{L_{ref}}$ | Lift coefficient reference factor |
| $N(u,v,w)$ | Normalised unit domain |
| $MBW$ | Mean-biased weighting |
| $EW$ | Equal weighting |
| $VBW$ | Variance-biased weighting |

# 1. INTRODUCTION

## 1.1. MOTIVATION FOR THE CURRENT STUDY

The deterministic aerodynamic design optimization is typically performed at fixed operation conditions without considering the variation and the uncertainty in these parameters, which may significantly affect the optimum performance of the deterministic aerodynamic design. For example, significant variation of drag coefficient can be observed in transonic flow with the change in Mach number and/or angle of attack. The objective of robust aerodynamic shape optimization is to obtain a design, which will keep its optimum performance under varying conditions or uncertain parameters. The robust optimization approach can also be thought similar to multi-point optimization in terms of the main goal, however the latter is still based on deterministic formulations at multiple discrete points whereas the former considers the stochastic nature of the problem by the integration of uncertainty modeling and propagation to the optimization process, which also uses a different objective function formulation involving the simultaneous minimization of the mean and the variance of the performance metric [1, 2]. The flowfield and adjoint solvers are evaluated at each iteration until the convergence is achieved, which may have significant impact on the computational cost of robust design. Therefore, it is important to select the proper turbulence model and shape parameterization technique with optimum parameters to achieve robust design with minimum computational cost while retaining the accuracy of the design at the desired level.

## 1.2. OBJECTIVE AND CONTRIBUTIONS OF THE CURRENT STUDY

The main objective of this study is to investigate the impact of two commonly used turbulence models (SA and SST) in Reynolds-Averaged Navier-Stokes simulations on two-dimensional and three-dimensional optimum design obtained with gradient-based deterministic and robust aerodynamic shape optimization in transonic, viscous, turbulent flow. In addition, the impact of three different shape parameterization techniques (B-Spline, Hicks-Henne, and FFD) is investigated on two-dimensional optimum design obtained with gradient-based deterministic and robust aerodynamic shape optimization. The impact of each turbulence model and shape parameterization technique is evaluated in terms of computational cost and difference in the shape and performance of the final design. The inherent variation of Mach number in transonic flow is modeled as the uncertain operating condition for the robust design study. The same shape parameterization techniques and turbulence models are first applied to the deterministic optimization of the same airfoil geometry (2-D) and the same wing geometry (3-D) at a selected mean Mach number to make comparison between the deterministic and robust optimization findings. In the robust optimization methodology, stochastic expansions obtained with point-collocation non-intrusive polynomial chaos (NIPC) technique are utilized for uncertainty quantification due to their computational accuracy and efficiency in stochastic aerodynamics problems.

The primary contribution of 2-D study to the aerodynamic design area is the evaluation of the impact of turbulence models with different shape parameterization techniques on the final design obtained with robust aerodynamic optimization under uncertainty. The results of 2-D study contributed to the design of optimum wing sections for transonic aircraft by improving the aerodynamic performance under uncertain operating conditions with a computationally efficient robust aerodynamic shape optimization methodology described in this work. The shape parameterization techniques, which gave the best optimization results (i.e. in terms of computational time and the performance of final design) from a previous study by the authors [3] are utilized for deterministic and robust design. The optimum

airfoil shapes, various aerodynamic quantities of interest (drag coefficient, lift coefficient, and pressure distribution), and the number of functional evaluations to converge obtained with different turbulence models and shape parameterization techniques are compared to evaluate their impact on the final design in robust optimization.

The primary contribution of 3-D study to the aerodynamic design area is the evaluation of the impact of turbulence models on three-dimensional wing design obtained with deterministic and robust aerodynamic shape optimization. This work is a follow-up to the 2-D study for the comparison of the findings between 2-D and 3-D deterministic and robust aerodynamic shape optimization. The optimum wing shapes, various aerodynamic quantities of interest (drag coefficient, lift coefficient, and pressure distribution), and the number of function evaluations to converge obtained with two turbulence models with three different weight contribution in the objective function cases are compared to investigate their impact on the final design in robust optimization.

## 1.3. DISSERTATION OUTLINE

The following section provides a literature review on aerodynamic shape optimization with the focus on previous studies relevant to the scope of this research. This section also contains the literature review of uncertainty quantification and shape parameterization techniques applied to airfoil/wing geometries. The computational fluid dynamics (CFD) model of the 2-D and 3-D problems, the information about the direct and adjoint solvers are provided in Section 3. Section 4 explains the turbulence models used in this work. Section 5 explains the optimization framework used for both robust and deterministic optimization, uncertainty quantification approach and robust optimization procedure. Section 6 consists of shape parameterization techniques, the problem definition and the related findings of deterministic and robust optimization of the 2-D study. Section 7 contains the shape parameterization technique, the problem definition and related findings of deterministic and robust optimization of the 3-D study. The conclusions and suggestions for future work are

presented in Section 8. Appendix A includes the grid convergence study of the RAE2822 airfoil. Appendix B contains the grid convergence study of the CRM wing. Appendix C includes the identification of the optimum factors for the 2-D shape parameterization techniques.

# 2. LITERATURE REVIEW

In this section, a review of previous studies on aerodynamic shape optimization of 2-D and 3-D problems are included. In particular, previous studies on the application of stochastic expansions as a means of uncertainty quantification in design optimization are discussed. In addition, the aerodynamic optimization studies focused on shape parameterization techniques and turbulence flows in transonic flow are presented.

In robust design studies, two different type of uncertainties, epistemic and aleatory (inherent) are considered in general [4, 5]. Epistemic uncertainty is reducible and due to lack of knowledge in computational models or parameters (e.g., turbulence model uncertainty in CFD simulation). Aleatory uncertainty [6] is irreducible and due to inherent variation of physical model (e.g., operating conditions). To characterize the uncertainty in a mathematical problem, aleatory uncertainties are typically presented with appropriate probability distribution function (e.g, uniform, normal, Weibull). In this study, we consider aleatory uncertainties in our robust optimization formulation both for 2-D and 3-D problems. In specific, the inherent variation of Mach number in transonic flow is modeled as an aleatory uncertainty with uniform distribution.

Uncertainty quantification is an important component of robust optimization to obtain the necessary statistics (such as the mean and the variance) of aerodynamic coefficients and their sensitivities with respect to design variables, which has to be repeated at each optimization iteration. The traditional uncertainty quantification methods based on sampling such as the Monte-Carlo approach become too expensive and impractical to use due to the large sample size requirement for the convergence of statistics. This is especially the case when high-fidelity Computational Fluid Dynamics (CFD) and adjoint solutions are utilized in aerodynamic design optimization. To remedy the computational cost associated with Monte-Carlo approach for design with uncertainty, various approaches are

proposed in previous studies to reduce the number of function evaluations to improve the efficiency of the robust design [7, 8, 9, 10]. To address the computational cost of uncertainty quantification in robust aerodynamic design with high-fidelity CFD models, we utilize the Point-Collocation Non-Intrusive Polynomial Chaos, an advanced uncertainty modeling and propagation method based on stochastic expansions, which has been shown to be very efficient and accurate in previous uncertainty quantification studies involving transonic and hypersonic aerodynamic flows [11, 12, 13].

In the literature, RANS and Euler based aerodynamic shape optimization are applied to different geometries and flow regimes. Euler equations are used to minimize the induced-drag of non-planar geometries and examine the optimal shape of flying wings for subsonic and transonic speeds [14, 15]. The previous studies also include the application of two and three-dimensional Navier-Stokes equations using discrete and continuous adjoint approach for the aerodynamic shape optimization problems [16, 17, 18].

Many authors proposed preliminary methods to obtain an insensitive design to the uncertainties in order to remedy the weakness of single-point optimization under varying conditions [19, 20, 21]. The majority of proposed techniques contains the gradient-based optimizer to solve the aerodynamic shape optimization problem [22, 23, 24, 25, 26]. In literature, the authors studied high-fidelity and multi-fidelity aerodynamic shape optimization with the consideration of large number of high fidelity function evaluations and large number of dimensions [27, 28]. Multi-modality, multi-point and multi-objective techniques in gradient-free aerodynamic shape optimization are also investigated in the previous studies [29, 30, 31, 32], however no study focused on a parametric investigation of the gradient-based robust optimization with stochastic expansions for RANS-based two and three dimensional aerodynamic shape optimization, which is addressed by this PhD research.

In the 2-D study, the best optimization results based on the shape parameterization technique (i.e. in terms of computational time and the performance of final design) from a previous study by Vuruskan and Hosder [3] are used for deterministic and robust design.

The findings experienced with each turbulence model for robust design is compared with the deterministic optimization results including the previous work reported in the literature [33, 34, 35, 36, 37]. The Spalart-Allmaras (SA) and the Menter's Shear Stress Transport (SST) models are studied to investigate their impact on the final design. SA and SST models are among the most commonly used one-equation and two-equation turbulence models, respectively in terms of accuracy, efficiency and design cycle time according to studies presented in the literature [38, 39]. SA model is shown to be robust and efficient in the modeling of many wall-bounded transonic, turbulent flows including aerodynamic shape optimization studies [40, 41]. Hicks-Henne bump functions, B-Spline curves and Free-Form Deformation (FFD) are utilized as shape parameterization techniques in 2-D study. In the previous studies, these parameterization techniques are shown to be effective to represent the initial geometry with less number of design variables and suitable for deforming the geometry presented by the set of curves or control points [42, 43].

The CRM transonic wing case from the AIAA Aerodynamic Design Optimization Discussion Group test problem database is studied for both the deterministic and robust optimization with two turbulence models (SA and SST) by using FFD shape parameterization technique [44, 45]. The previous studies focusing on the optimization of CRM wing or body/wing configuration mostly utilized a single turbulence model [46, 47, 48]. The multi-point optimization of CRM wing is performed in the studies [49, 50] which include the deterministic optimization formulation with discrete points. In addition, the multi-modality and high-fidelity optimization of CRM wing are presented in the previous studies [51, 52]. The FFD shape parametrization technique which is used in 3-D wing study of this work have been used frequently on the aerodynamic shape optimization of 3-D geometries because it is flexible and highly accurate to parameterize the complex geometries [46, 47, 48, 53, 54].

# 3. COMPUTATIONAL FLUID DYNAMICS MODEL

In this section, the computational fluid dynamics (CFD) model of 2-D and 3-D studies are explained. In this study, deterministic and robust optimization are performed to minimize the drag coefficient of RAE2822 airfoil and CRM wing at transonic flow conditions at a specified lift coefficient value. Robust design is also targeted to minimize the variation of the drag coefficient under uncertainty (i.e., variation in Mach number).

## 3.1. COMPUTATIONAL FLUID DYNAMICS MODEL FOR RAE2822 AIRFOIL

In the 2-D study, the open-source CFD code SU2 [55, 56] is utilized for the solution of the flow field and to obtain the adjoint-based sensitivities. In both deterministic and robust optimization studies, SU2 is used to solve steady, 2-D, Reynolds-Averaged Navier-Stokes (RANS) equations with standard form of SA and SST turbulence models. In SA model, one equation is solved to obtain turbulent (eddy) viscosity for aerodynamic wall-bounded flow problems. In SST model, two equations are solved to obtain the turbulent (eddy) viscosity. The more information on these turbulence models is given in the next section.

In the solutions obtained with SU2, finite volume method was utilized to discretize RANS Equations. Jameson-Schmidt-Turkel scheme [57] with second-order scalar upwind discretization and Venkatakrishnan's limiter was used to model the convective fluxes. The viscous terms are calculated with least-squares approach with second-order spatial accuracy. The GMRES method was utilized to solve the linear system with an error tolerance value of $10^{-4}$, and Euler implicit method was applied for time integration to reach the steady state solution. The adjoint solver was utilized to obtain the sensitivities of lift and drag coefficients with respect to the design variables at each optimization iteration. The solution convergence criterion for all cases was set to have a maximum number of 5000 iterations or

a reduction in the residuals by six orders of magnitude. SU2 mesh deformation script (SU2 MDC) was utilized to deform mesh after modifying the airfoil shape based on the updated design variables at each optimization iteration.

The unstructured mesh (O-grid) used in the CFD model (Figure 3.1) was constructed around RAE2822 airfoil with 22,842 elements in total. 40 and 192 edges are used for the far-field boundary and the surface of the airfoil, respectively. The airfoil was placed at a distance of 100-chord length away from the far-field boundary. Hybrid mesh with quadrilaterals was utilized at the vicinity of airfoil surface and continued with triangular mesh in the remaining region of control volume. The first grid point normal to wall was located $10^{-5}$ chord length away from the airfoil surface and its non-dimensionalized distance ($z^+$) was determined to be approximately 1. A grid convergence study is performed for the RAE2822 airfoil and for each turbulence model at a Mach number of 0.734, Re number of $Re = 6.5 \times 10^6$, $\alpha$ of 2.92° for SA and $\alpha$ of 3.06° for SST model. The results of this study are presented in Appendix A. Original (baseline) grid used in this study is called as medium grid in the grid convergence study whose topology is fixed while generating the two finer and one coarser mesh level. The grid convergence study showed that the grid level utilized in this study has sufficient accuracy in resolving the quantities of interest used in aerodynamic shape optimization of the RAE2822 transonic airfoil.

Deterministic optimization was performed at a Mach number of $M = 0.734$, Reynolds number of $Re = 6.5 \times 10^6$ and at a target lift coefficient of $C_{L_{Target}} = 0.824$ which was obtained at an angle of attack of $\alpha = 2.92°$ for SA and $\alpha = 3.06°$ for SST model with the initial airfoil geometry. In robust optimization, Mach number was modeled as a uniformly distributed random variable with interval $[0.725, 0.743]$ including its nominal (mean) value of 0.734. The angle of attack was varied as a design variable to match the lift constraint in both the deterministic and robust optimization processes.

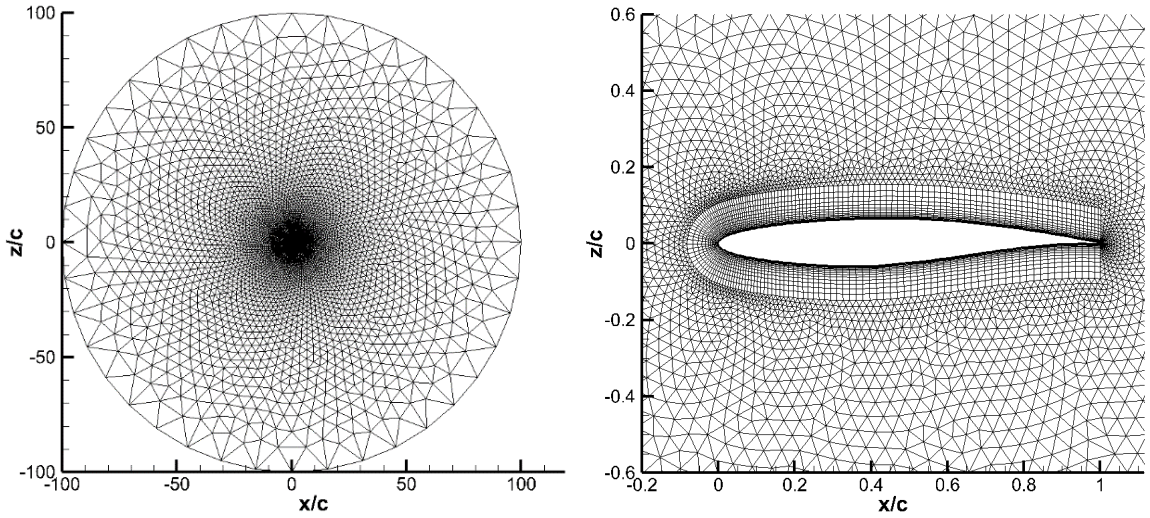


(a) (b)

Figure 3.1. (a) Computational grid. (b) The view of the grid at the vicinity of the airfoil surface.

## 3.2. COMPUTATIONAL FLUID DYNAMICS MODEL FOR THE CRM WING

In the 3-D study, SU2 code is used to solve steady, 3-D, Reynolds-Averaged Navier-Stokes (RANS) equations with two turbulence models (i.e. SA or SST). Similar to 2-D study, finite volume method was utilized to discretize RANS Equations in the solutions obtained with SU2. Jameson-Schmidt-Turkel scheme with second-order scalar upwind discretization and Venkatakrishnan's limiter were used to model the convective fluxes. The viscous terms were calculated with least-squares approach with second-order spatial accuracy. The GMRES method was utilized to solve the linear system with an error tolerance value of 1E-04, and Euler implicit method was applied for time integration to reach the steady state solution. The adjoint solver was utilized to obtain the sensitivities of lift and drag coefficients with respect to the design variables at each optimization iteration. The solution convergence criterion for all cases was set to have a maximum number of 15000

iterations or a reduction in the residuals by six orders of magnitude. SU2 mesh deformation script (SU2 MDC) was utilized to deform mesh after modifying the wing shape with respect to updated design variables at each optimization iteration.

The structured mesh (O-grid) used in the CFD model (Figure 3.2) was constructed around the NASA Common Research Model (CRM) wing [58] with 450,560 elements, which was determined to have sufficient resolution after a grid convergence study (Appendix B) and included 120, 92 and 40 edges chordwise, spanwise and off-wing directions, respectively. The wing was placed at a distance of 25-span lengths away from the far-field boundary. The coordinates are scaled by the mean aerodynamic chord, therefore the reference chord is 1.0. The first grid point was located 1E-05 reference chord length away from the wing surface and its non-dimensionalized distance ($z^+$) is approximately 2.2.

Deterministic optimization was performed at a Mach number of $M = 0.85$, Reynolds number of $Re = 5 \times 10^6$ and at a target lift coefficient of $C_{L_{Target}} = 0.65$ which was obtained at angle of attack of $\alpha = 3.56°$ for SA and $\alpha = 3.81°$ for SST with the initial wing geometry. In robust optimization, Mach number was modeled as a uniformly distributed random variable with interval $[0.827, 0.873]$ including its nominal (mean) value of 0.85. The angle of attack was varied as a design variable to match the lift constraint in both the deterministic and robust optimization processes.

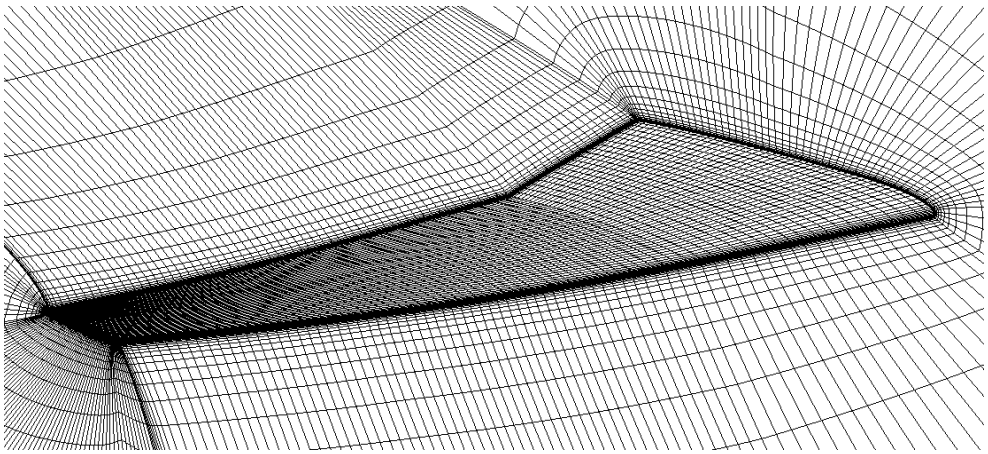

Figure 3.2. The view of the grid in the vicinity of the wing.

# 4. TURBULENCE MODELS

In this section, the two RANS turbulence models used in this study are outlined. In the description of the turbulence models, the nomenclature of turbulence modeling resource (TMR) website of NASA Langley Research Center is utilized [59].

## 4.1. SPALART-ALLMARAS ONE-EQUATION MODEL (SA)

The SA model is developed from the Nee-Kovasznay model [60] with several compressibility and near-wall corrections [61]. SA model is simpler, computationally less expensive and more robust than the multi-equation turbulence models. Therefore, it is a commonly used turbulence models in wall-bounded external aerodynamic flow applications. The model is given by

$$\begin{aligned}\frac{\partial \hat{\nu}}{\partial t} + u_j \frac{\partial \hat{\nu}}{\partial x_j} &= c_{b1}(1 - f_{t2})\hat{S}\hat{\nu} - \left[c_{w1} f_w - \frac{c_{b1}}{\kappa^2} f_{t2}\right]\left(\frac{\hat{\nu}}{d}\right)^2 \\ &+ \frac{1}{\sigma}\left[\frac{\partial}{\partial x_j}\left((\nu + \hat{\nu})\frac{\partial \hat{\nu}}{\partial x_j}\right) + c_{b2}\frac{\partial \hat{\nu}}{\partial x_i}\frac{\partial \hat{\nu}}{\partial x_i}\right]\end{aligned} \tag{4.1}$$

The complete formulation of the model is given by Spalart and Allmaras [61]. The turbulent eddy viscosity is computed from:

$$\mu_t = \rho \hat{\nu} f_{v1} \tag{4.2}$$

where

$$f_{v1} = \frac{\chi^3}{\chi^3 + c_{v1}^3}, \quad \chi = \frac{\hat{\nu}}{\nu} \tag{4.3}$$

and $\rho$ is the density, $\nu = \mu/\rho$ is the molecular kinematic viscosity, and $\mu$ is the molecular dynamic viscosity. Additional definitions are given by the following equations:

$$\hat{S} = \Omega + \frac{\hat{\nu}}{\kappa^2 d^2} f_{v2} \tag{4.4}$$

where $\Omega = \sqrt{2W_{ij}W_{ij}}$ is the magnitude of the vorticity, $d$ is the distance from the field point to the nearest wall, and

$$\begin{gathered} f_{v2} = 1 - \frac{\chi}{1 + \chi f_{v1}}, \quad f_w = g\left[\frac{1 + c_{w3}^6}{g^6 + c_{w3}^6}\right]^{1/6}, \quad g = r + c_{w2}(r^6 - r) \\ r = \min\left[\frac{\hat{v}}{\hat{S}\kappa^2 d^2}, 10\right], \quad f_{t2} = c_{t3}\exp(-c_{t4}\chi^2), \quad W_{ij} = \frac{1}{2}\left(\frac{\partial u_i}{\partial x_j} - \frac{\partial u_j}{\partial x_i}\right) \end{gathered} \tag{4.5}$$

The constants are;

$$\begin{gathered} \sigma = 2/3, \quad c_{b1} = 0.1355, \quad c_{b2} = 0.622, \quad \kappa = 0.41 \\ c_{w1} = \frac{c_{b1}}{\kappa^2} + \frac{1 + c_{b2}}{\sigma}, \quad c_{w2} = 0.3, \quad c_{w3} = 2, \quad c_{v1} = 7.1 \end{gathered} \tag{4.6}$$

The turbulent eddies are absent very near to the wall, therefore $\hat{v}$ is zero on the viscous walls. Some fraction of the laminar viscosity at the far-field is implemented as the far-field boundary condition for the turbulent viscosity.

## 4.2. MENTER SHEAR-STRESS TRANSPORT TWO-EQUATION MODEL (SST)

Menter's SST model is a two-equation model that contains traditional $k - \omega$ and $k - \epsilon$ models [62, 63]. The goal is to utilize the $k - \omega$ model at the near-region which is the most accurate, and to take the advantage of the freestream independence of the $k - \epsilon$ model in the outer part of the boundary layer. The model is given by

$$\frac{\partial(\rho k)}{\partial t} + \frac{\partial(\rho u_j k)}{\partial x_j} = P - \beta^* \rho\omega k + \frac{\partial}{\partial x_j}\left[(\mu + \sigma_k \mu_t)\frac{\partial k}{\partial x_j}\right] \tag{4.7}$$

$$\frac{\partial(\rho\omega)}{\partial t} + \frac{\partial(\rho u_j \omega)}{\partial x_j} = \frac{\gamma}{v_t}P - \beta\rho\omega^2 + \frac{\partial}{\partial x_j}\left[(\mu + \sigma_\omega \mu_t)\frac{\partial \omega}{\partial x_j}\right] + 2(1 - F_1)\frac{\rho\sigma_{w2}}{\omega}\frac{\partial k}{\partial x_j}\frac{\partial \omega}{\partial x_j} \tag{4.8}$$

The complete formulation is given by Menter [62, 63]. The closure coefficients include

$$\gamma_1 = \frac{\beta_1}{\beta^*} - \sigma_{w1}\frac{\kappa^2}{\sqrt{\beta^*}} \tag{4.9}$$

$$\gamma_2 = \frac{\beta_2}{\beta^*} - \sigma_{w2}\frac{\kappa^2}{\sqrt{\beta^*}} \tag{4.10}$$

where $\beta_1 = 0.075$, $\beta_2 = 0.0828$, $\beta^* = 0.09$, $\sigma_{w1} = 0.5$, $\sigma_{w2} = 0.856$, and $\kappa = 0.41$. $P$, $\tau_{ij}$, and $S_{ij}$ are given by:

$$P = \tau_{ij}\frac{\partial u_i}{\partial x_j} \tag{4.11}$$

$$\tau_{ij} = \mu_t\left(2S_{ij} - \frac{2}{3}\frac{\partial u_k}{\partial x_k}\delta_{ij}\right) - \frac{2}{3}\rho k\delta_{ij} \tag{4.12}$$

$$S_{ij} = \frac{1}{2}\left(\frac{\partial u_i}{\partial x_j} + \frac{\partial u_j}{\partial x_i}\right) \tag{4.13}$$

The turbulent eddy viscosity is computed from:

$$\mu_t = \frac{\rho a_1 k}{\max(a_1\omega, SF_2)} \tag{4.14}$$

where $S = \sqrt{2S_{ij}S_{ij}}$, $a_1 = 0.31$. Each of the constant is a blend of inner (1) and outer (2) constant, blended via

$$\phi = F_1\phi_1 + (1 - F_1)\phi_2 \tag{4.15}$$

where $\phi_1$ represents constant 1, and $\phi_2$ represents constant 2. Additional functions are given by

$$\begin{gathered} F_1 = \tanh(\arg_1^4), \quad \arg_1 = \min\left[\max\left(\frac{\sqrt{k}}{\beta^*\omega d}, \frac{500v}{d^2\omega}\right), \frac{4\rho\sigma_{\omega 2}k}{CD_{k\omega}d^2}\right] \\ v_t = \frac{\mu_t}{\rho}, \quad CD_{k\omega} = \max\left(2\rho\sigma_{\omega 2}\frac{1}{\omega}\frac{\partial k}{\partial x_j}\frac{\partial \omega}{\partial x_j}, 10^{-20}\right) \\ F_2 = \tanh(\arg_2^2), \quad \arg_2 = \max\left(2\frac{\sqrt{k}}{\beta^*\omega d}, \frac{500v}{d^2\omega}\right) \end{gathered} \tag{4.16}$$

where $\rho$ is the density, $v_t$ is the turbulent kinematic viscosity, $\mu$ is the dynamic viscosity, $d$ is the distance from the field point to the nearest wall, and $\omega$ is the vorticity magnitude.

# 5. UNCERTAINTY QUANTIFICATION APPROACH AND ROBUST OPTIMIZATION PROCEDURE

## 5.1. OPTIMIZATION FRAMEWORK

Figure 5.1 shows the optimization framework developed for deterministic or robust optimization to minimize the objective function of the aerodynamic design problem. The inputs of the framework are flow and adjoint solver parameters setting, the numerical algorithms and physics models, the specification of the shape parameterization technique, design variables associated with the shape parameterization technique used, angle of attack (if used as a design variable), uncertain variables and their distributions (uniform or normal), objective function and constraints. The optimized shape and its aerodynamic characteristics are served as outputs of the framework.

To generate the initial geometry (e.g., airfoil or 3-D wing), current options available in the framework include the use of externally provided point data or B-Spline control points. Hicks-Henne bump functions, B-Spline curves, and Free-Form Deformation are the current shape parameterization techniques for two-dimensional problems. Free-Form Deformation is the current shape parameterization technique for three-dimensional problems. As shown in a previous aerodynamic optimization study by the authors [3, 64], parameterization with Hicks-Henne bump functions and B-Spline curves were able to produce optimum airfoil shapes with no shocks or weaker shocks in transonic flow which is the main contributor to the drag coefficient. Currently, the optimum airfoil shapes or wings with no shock or weaker shocks in transonic flow can be produced by utilizing Free-Form Deformation technique in the framework.

In this study, the open-source CFD code SU2 is utilized for the solution of the flow field and obtaining the adjoint-based sensitivities used in gradient-based optimization. Moreover, SU2 mesh deformation script is utilized to deform the mesh after modifying

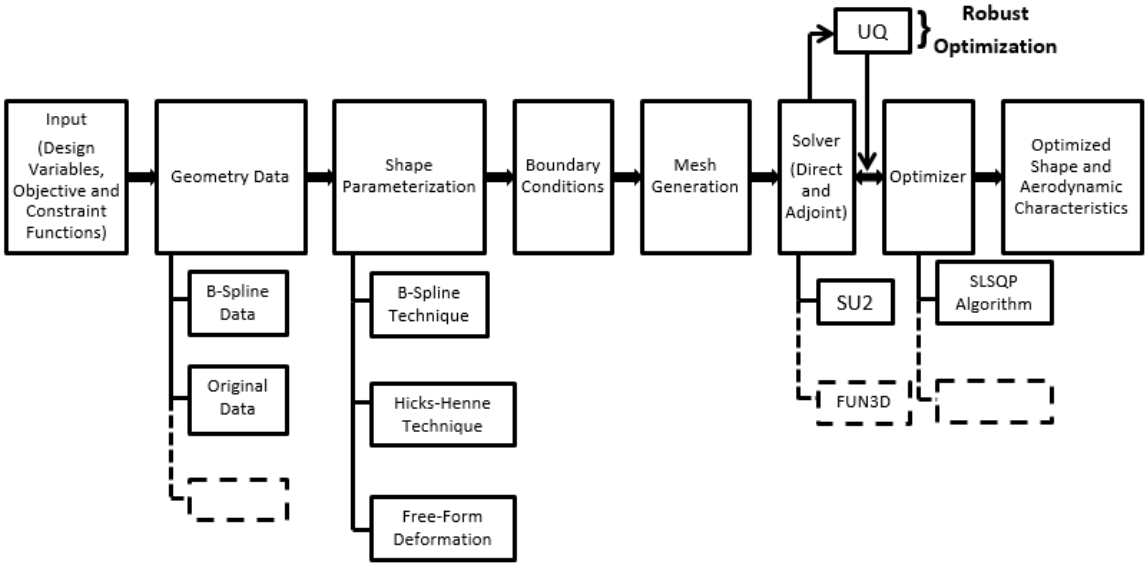


Figure 5.1. Optimization framework.

the wing shape based on the updated design variable values. The framework is created modular so that various CFD software for flow and adjoint solutions can be utilized in the place of SU2 such as the FUN3D code from NASA. Another advantage of the framework is the flexibility for the integration of different optimization algorithms, which currently uses the SLSQP algorithm [65, 66]. Uncertainty quantification module integrated to the optimization algorithm provides the modeling of input uncertainties and the propagation of uncertainty with polynomial chaos expansions (PCE) for robust optimization.

## 5.2. UNCERTAINTY QUANTIFICATION APPROACH

The robust optimization approach described in the next section utilizes the Point-Collocation Non-Intrusive Polynomial Chaos (NIPC) method as the uncertainty quantification approach to obtain the statistical metrics (the mean and variance) used in the optimization formulation. The Point-Collocation NIPC is based on the polynomial chaos theory. With this theory, an uncertain response function $R$ (e.g., lift, drag, or pressure coefficient)

can be represented with a series expansion:

$$R(\vec{x}, \vec{\xi}) \approx \sum_{j=0}^{P} \alpha_j(\vec{x}) \Psi_j(\vec{\xi}) \tag{5.1}$$

where the random basis function of $j^{th}$ mode is represented by $\Psi_j(\vec{\xi})$ which is a polynomial function of n-dimensional standard random variable vector ($\vec{\xi}$), and the coefficient $\alpha_j$ which is a function of the deterministic variable vector ($\vec{x}$), (e.g., the deterministic design variables). Random basis functions are in the form of multi-dimensional Hermite Polynomials when the distribution of uncertain variable is defined as Gaussian which is first studied by Wiener [67]. The application of polynomial chaos theory on the continuous non-normal input uncertainty is extended by using the set of polynomials known as Askey scheme [68]. The Legendre and Laguerre polynomials are included in Askey Scheme and used as optimal basis functions for uniform and exponential input uncertainty distribution respectively. Multivariate basis functions can be utilized for the different distribution of random variables in the same problem [69]. Different stochastic problems studied with polynomial chaos can be found in literature [70, 71, 72].

In theory, Equation 5.1 should include infinite number of terms, but for practical implementation of the polynomial chaos expansion, a discrete sum is taken over a number of output modes ($N_t = P + 1$). The total number of samples used to generate the response surface, $N_s$, is;

$$N_s = n_p \cdot (P + 1) = n_p \left[ \frac{(n + p)!}{n!p!} \right] \tag{5.2}$$

where $p$ is the polynomial order, $n$ is the number of uncertain variables, and $n_p$ is the oversampling ratio for the Point-Collocation NIPC.

The first step of Point-Collocation NIPC method is to replace a stochastic response or random function with its polynomial chaos expansion given by Equation 5.1. Then, $N_s$ vectors are chosen in random space and the deterministic code is evaluated at these points.

$$\begin{pmatrix} R(\vec{x}, \vec{\xi}_0) \\ R(\vec{x}, \vec{\xi}_1) \\ \vdots \\ R(\vec{x}, \vec{\xi}_{N_s-1}) \end{pmatrix} = \begin{pmatrix} \Psi_0(\vec{\xi}_0) & \Psi_1(\vec{\xi}_0) & \dots & \Psi_P(\vec{\xi}_0) \\ \Psi_0(\vec{\xi}_1) & \Psi_1(\vec{\xi}_1) & \dots & \Psi_P(\vec{\xi}_1) \\ \vdots & \vdots & \ddots & \vdots \\ \Psi_0(\vec{\xi}_{N_s-1}) & \Psi_1\vec{\xi}_{N_s-1}) & \dots & \Psi_P(\vec{\xi}_{N_s-1}) \end{pmatrix} \begin{pmatrix} \alpha_0 \\ \alpha_1 \\ \vdots \\ \alpha_P \end{pmatrix} \tag{5.3}$$

The linear system of equations is solved for the coefficients ($\alpha_j$) of the stochastic expansion. At a minimum, $N_t$ deterministic function evaluations are needed for the solution of Equation 5.3. Least-squares method can be used for the over-determined system of equations which has more samples ($N_s$) than $N_t$. Based on the conclusions from a previous study [3], an oversampling ratio of 2.0 is used in this study.

## 5.3. ROBUST OPTIMIZATION PROCEDURE

Figure 5.2 presents the flowchart for robust optimization procedure. The inputs to the framework for robust optimization are the deterministic design variables ($\vec{s}$) (i.e. the angle of attack, function amplitudes or control points), uncertain variables (i.e. Mach number, $M(\vec{\xi})$), objective and constraint functions and NIPC order (Step 1). In this study, constraints are used to bound the design variables while modifying the geometry.

In step 2, the number of samples ($N_s$) are calculated based on the order of polynomial function ($p$), the number of random dimensions ($n$), and over sampling ratio ($n_p$) in Equation 5.2. In this study, the number of random variables is 1 (the Mach number); the polynomial order is chosen as $p = 2$, and an oversampling ratio of $n_p = 2$ is used. These parameters give the total number of samples required to create the stochastic response surface as $N_s = 6$. These samples were chosen uniformly in the given uncertain Mach number interval [0.725,

0.743], since the Mach number is modeled as a uniform uncertain variable in this study. After the determination of the sample points (i.e., the Mach numbers), the direct and adjoint solvers are evaluated at these sample points to calculate the lift and drag coefficients and their sensitivities. Then, the stochastic expansions are created for each force coefficient via Point-Collocation NIPC;

$$R(\vec{\xi}, \vec{s}) = \sum_{j=0}^{P} \alpha_j(\vec{s})\psi_j(\vec{\xi}) \tag{5.4}$$

where $R$ is the response surface (drag and lift), $\psi_j$ is the basis function (Legendre polynomial for this study). Here, $\vec{s}$ is deterministic variable vector (design variables) and $\vec{\xi}$ is the standard random variable vector (a single uniform random variable for this study where $M = M(\vec{\xi})$). In step 3, the stochastic expansions are utilized to calculate the mean (Equation 5.5) and the variance (Equation 5.6) of the force coefficients. In specific, the first coefficient of the expansion gives the mean and the variance is obtained by evaluating Equation 5.6, where $\langle ... \rangle$ indicates the inner product integral over the support region of the uncertain variable.

$$\mu(\vec{s}) = \langle R \rangle = \sum_{k=0}^{P} \alpha_k(\vec{s})\psi_k(\vec{\xi}) = \alpha_0(\vec{s}) \tag{5.5}$$

$$\sigma^2(\vec{s}) = \sum_{k=1}^{P} \alpha_k^2(\vec{s})\langle \psi_k^2 \rangle \tag{5.6}$$

Sensitivities obtained with the adjoint solver at each sample point are utilized to calculate the sensitivity of the mean (Equation 5.7) and the variance (Equation 5.8) with respect to each design variable [73]:

$$\frac{d\mu}{d\vec{s}} = \frac{d\alpha_0(\vec{s})}{d\vec{s}} = \left\langle \frac{dR}{d\vec{s}} \right\rangle \tag{5.7}$$

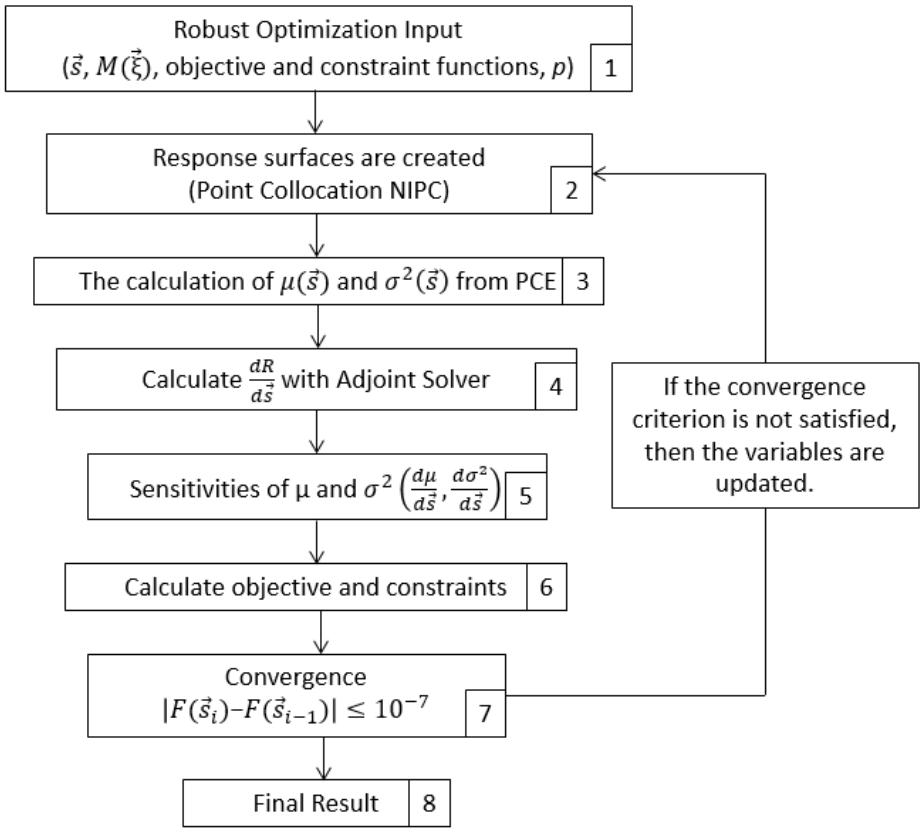


Figure 5.2. Robust optimization flowchart.

$$\frac{d\sigma^2}{d\vec{s}} = 2\sum_{k=1}^{P} \alpha_k(\vec{s})\left\langle \frac{dR}{d\vec{s}}, \psi_k \right\rangle \tag{5.8}$$

Then, the objective function involving the statistics of the force coefficients is calculated (Box 6) and checked against the specified convergence criterion (Box 7). If it is satisfied, the current shape is declared as the optimized shape (Box 8). If the difference between the current and previous objective function is higher than the specified tolerance ($10^{-7}$), the mean and the variance of aerodynamic coefficients and their sensitivities are inserted into the SLSQP algorithm to update the design variables and the entire optimization procedure is repeated between steps 2 and 7 until the convergence is achieved. It is important to note that at each optimization iteration the required number of direct solver and adjoint solver evaluations is equal to $N_s$, which is equal to 6 for the current robust optimization problem.

In other words the computational cost of robust optimization will be $N_s$ times higher than the deterministic optimization cost for the same number of optimization iterations to converge. Although it is more expensive compared to the deterministic design, the robust optimization approach based on stochastic expansions will be much more efficient than a robust optimization approach which utilizes a traditional sampling method such as Monte Carlo for the evaluation of the statistical quantities at each iteration.

# 6. 2-D ROBUST AERODYNAMIC SHAPE OPTIMIZATION

## 6.1. SHAPE PARAMETERIZATION TECHNIQUES

In 2-D study, three shape parameterization techniques (B-Spline curves, Hicks-Henne bump functions, and Free-Form Deformation) are studied. A description of each technique is presented below.

**6.1.1. Parameterization with B-Spline Curves.** With this technique, the shape is represented by B-Spline curves and surfaces. Control points are defined as design variables, and the shape is modified by moving the control points in $z$ direction at the same $x$ location. The B-Spline function of order $k$ is expressed with

$$C(t) = \sum_{i=0}^{n} P_i N_{i,k}(t), \quad t_0 \leq t \leq t_{max}, \quad k \leq n+1 \tag{6.1}$$

where $N_{i,k}(t)$ are the B-Spline basis functions and $P_i$ is the position vector of $i^{th}$ control point. Knot vectors are known as $t = t_i$. The basis functions are calculated with Equations (6.2) and (6.3):

$$N_{i,1} = \begin{cases} 1, & \text{if } t_i \leq t \leq t_{i+1} \\ 0, & \text{elsewhere} \end{cases} \tag{6.2}$$

and

$$N_{i,k}(t) = \frac{t - t_i}{t_{i+k-1} - t_i} N_{i,k-1}(t) + \frac{t_{i+k} - t}{t_{i+k} - t_{i+1}} N_{i+1,k-1}(t) \tag{6.3}$$

for $k = 2, 3, ..., K$ for all $i$ values. The order of basis functions can be any positive integer number. In optimization problems, the control points are defined as design variables. The illustration of B-spline shape parameterization technique is presented in Figure 6.1.

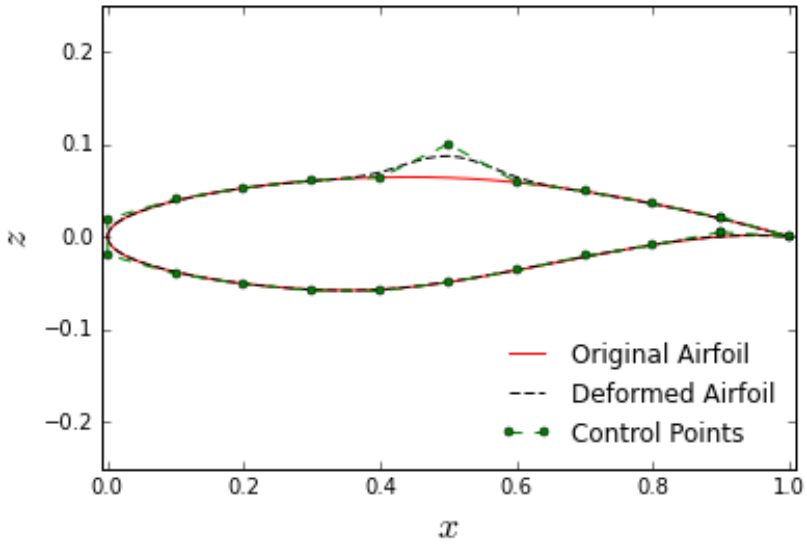


Figure 6.1. Illustration of B-Spline shape parametrization technique.

B-Spline curves provide local control on the geometry, and the degree of polynomial function can be limited based on user specification without changing the number of control points.

**6.1.2. Parameterization with Hicks-Henne Bump Functions.** Hicks and Henne [74, 75] proposed to use bump functions for airfoil design. They are summed and added to the initial shape for the perturbation of the geometry. In this parameterization technique, function amplitude is used as a design variable. The new airfoil shape can be defined as:

$$z(x) = z(x)_{baseline} + \sum_{n=1}^{N} \delta_n f_n(x) \tag{6.4}$$

where $z(x)_{baseline}$ is $z$ values of the initial shape at each $x$ location, $\delta_n$ is the function amplitude, $N$ is the number of bump function, and

$$f_n(x) = [sin(\pi x^{\frac{log0.5}{logt_1}})]^{t_2}, \quad 0 \leq t_1 \leq 1 \tag{6.5}$$

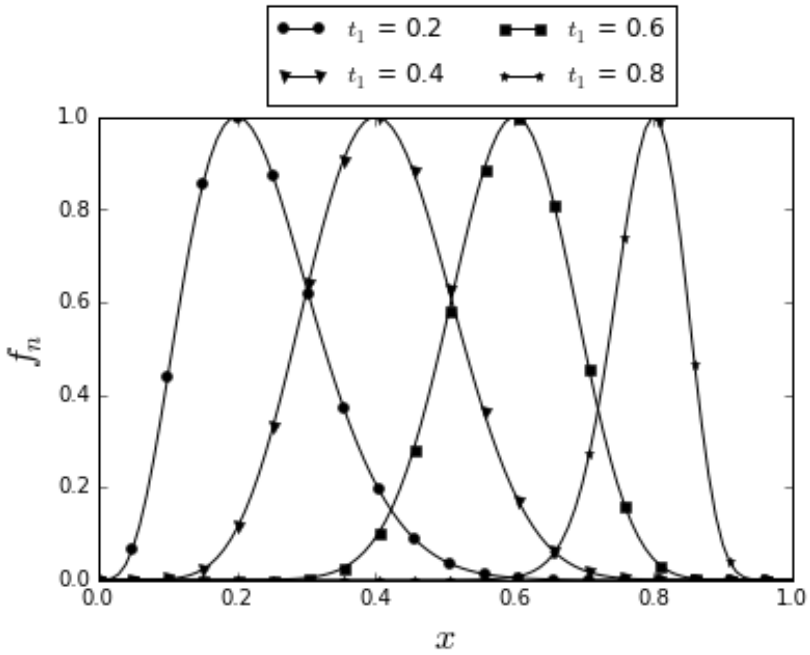


Figure 6.2. Hicks-Henne bump functions with $t_2 = 10$.

where $t_1$ is the location of maximum function value (function amplitude) and $t_2$ represents the width of the bump function. In the optimization problems, function amplitudes are defined as design variables. Hicks-Henne bump functions with $t_2 = 10$ with different $t_1$ values are shown in Figure 6.2.

Hicks-Henne bump functions can refine certain regions or the entire region of the airfoil surface. Bump functions are located between $x = 0.0001$ and 0.9999 in this study. The width of the function and the number of function amplitudes (design variables) can have a significant effect on the optimized shape.

**6.1.3. Parameterization with Free-Form Deformation.** Free-Form Deformation (FFD) is based on a domain deformation technique proposed by Sederberg and Parry [76] instead of deforming the surface itself. With this approach, the airfoil is embedded into the rectangular lattice by constraining the control points to a plane shown in Figure 6.3. A two-dimensional space of $(m + 1) \times (n + 1)$ uniformly distributed Bezier surface control points, $P_{i,j}$, are located around the airfoil, and the control lattice is created. The two-

dimensional space is normalised to the unit domain $N(u, v) \in [0, 1] \times [0, 1]$ by the following transformation equation:

$$u(x) = \frac{x - x_{min}}{x_{max} - x_{min}}, \quad v(z) = \frac{z - z_{min}}{z_{max} - z_{min}} \tag{6.6}$$

where $[x_{min}, x_{max}]$ and $[z_{min}, z_{max}]$ are the intervals of the control lattice in $x$ and $z$ directions, respectively. The deformation of the airfoil is defined as:

$$X(u(x), v(z)) = \sum_{j=0}^{n} \sum_{i=0}^{m} B_{i,m}(u(x)) B_{j,n}(v(z)) P_{i,j} \tag{6.7}$$

where $B_{i,m}(u(x))$ and $B_{j,n}(v(z))$ are Bernstein polynomials and $P_{i,j}$ is the control point. The control point position is calculated with the following equation:

$$P_{i,j} = \left( x_{min} + \frac{i}{m}(x_{max} - x_{min}), z_{min} + \frac{j}{n}(z_{max} - z_{min}) \right). \tag{6.8}$$

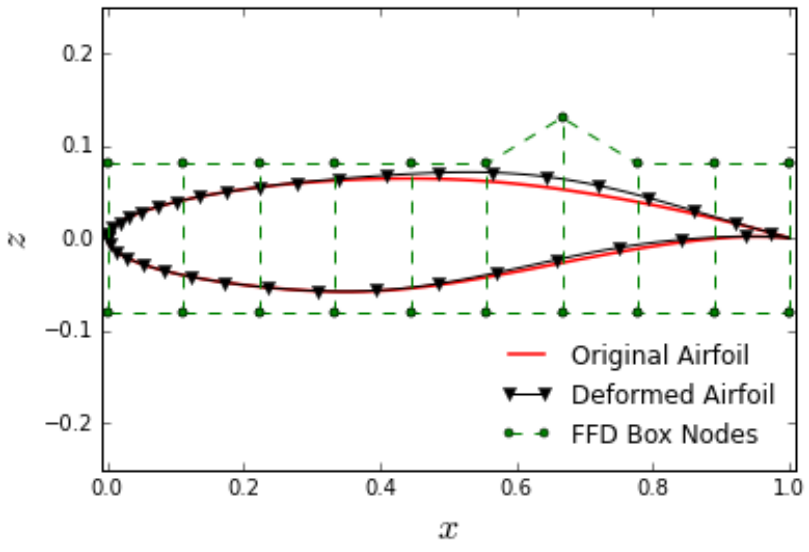


Figure 6.3. Two-dimensional FFD box.

The Bernstein polynomial, $B_{i,m}(u(x))$, is defined as:

$$B_{i,m}(u(x)) = \binom{m}{i}(u(x))^i(1-u(x))^{(m-i)}, \quad i = 0, ..., n \tag{6.9}$$

where $\binom{m}{i}$ is a binomial coefficient.

FFD is a versatile and strong technique, and local deformation over the geometry is possible with the FFD technique. It is compatible with different surfaces of any formulation or polynomial degree.

## 6.2. DETERMINISTIC OPTIMIZATION

In this study, deterministic optimization results are performed to make a comparison between the performance of the same shape parameterization techniques and the turbulence models used in robust optimization in terms of their effectiveness and computational cost. The objective of deterministic optimization is to reduce the drag coefficient $C_D$ of the airfoil at a specified Mach number subject to a specified minimum lift coefficient $C_L$ and area constraint.

**6.2.1. Problem Statement.** The optimization of RAE2822 airfoil is performed for steady, viscous, turbulent flow at a Mach number of 0.734 and Re number of $6.5 \times 10^6$. The shape parameterization techniques included B-Spline curves with 20 control points, Hicks-Henne bump functions with 256 bump functions and $t_2 = 10$ (the width of the function), and FFD with 2x40 control lattice with the size of $[-0.1, 0.1]$ in $z$ direction. The uniform distribution (UD) is implemented for the spacing of design variables over the geometry for each parameterization technique. The settings for each shape parameterization technique were determined by a parametric study [3] described in Appendix C, which gave the most effective deterministic optimum design with minimum computational cost.

The angle of attack is defined as a design variable for all cases, and the $C_L$ constraint is included in the objective function, setting the target $C_L$ as 0.824. For B-Spline curves, the angle of attack is constrained within the interval $[-10.0°, 10.0°]$, and the non-dimensionalized vertical position of each control point is limited with the interval $[-0.1, 0.1]$. For Hicks-Henne bump functions, the angle of attack is constrained within the interval $[2.0°, 4.0°]$, and the function amplitude limit is set $[-0.01, 0.01]$ at each iteration. For FFD, the angle of attack is also constrained within the $[2.0°, 4.0°]$, and the size of control lattice is set $[-0.01, 0.01]$ at each iteration. The boundary of each control point is set $[0.5z_i, 1.5z_i]$ where $z_i$ is the $z$ coordinate of $i^{th}$ control point at each iteration. It has been noticed that the angle of attack value remained between 2.0° and 4.0° at each iteration that was obtained with B-Spline curves, which is the first parameterization technique applied for the optimization of RAE2822 airfoil. The same optimization problem is repeated by constraining the angle of attack within the interval $[2.0°, 4.0°]$, and it was verified that the optimal shape, the aerodynamic coefficients of the optimal shape, and the number of iterations to converge were the same. Therefore, the angle of attack constraint of $[2.0°, 4.0°]$ was used for the studies with Hicks-Henne bump functions and FFD techniques.

The optimization algorithm started with the original airfoil shape and with 2.92° and 3.06° as the initial values of the angle of attack for the SA and SST turbulence model, respectively. The weights are specified in the objective function within the interval [0, 1] according to following relation:

$$\sum_{i=1}^{n} W_i = 1 \tag{6.10}$$

where $W_i$ is the weight of the $i^{th}$ term in the objective function, including $n$ number of terms. A weighted objective function is defined to include the $C_L$ constraint along with the main objective of the minimization of the $C_D$:

$$minimize \quad W_1 \left( \frac{C_D}{C_{D_{ref}}} \right)^2 + W_2 \left( \frac{C_{L_{Target}} - C_L}{C_{L_{ref}}} \right)^2 \tag{6.11}$$

where the weights $W_1$ and $W_2$ are 0.5, the reference factor of the drag coefficient, $C_{D_{ref}}$, is 0.007, and the reference factor of the lift coefficient, $C_{L_{ref}}$, is 0.224. The reference factors are used as normalization factors to bring the magnitude of the $C_L$ and $C_D$ terms to the same level, and the weights are utilized to adjust the contribution of each term to the objective function. The contribution of each term to the objective function in terms of their percentage is investigated on test cases, and the optimum combination of the weights is selected based on the test case results. It is important to note that the pitching moment coefficient constraint is excluded in the problem formulation for both the deterministic and robust aerodynamic optimization; therefore, higher tail lift and trim drag will be required due to a higher nose-up pitching moment.

**6.2.2. Deterministic Optimization Results.** The lift coefficient ($C_L$) of the original shape is 0.824 for each turbulence model. The drag coefficient ($C_D$) is 0.0209, obtained at $\alpha = 2.92°$ with the SA model and 0.0217, obtained at $\alpha = 3.06°$ with the SST model. The area of the airfoil is non-dimensionalized by $c^2$, which is 0.0778 for the original geometry. The numerical results of the optimized shapes are given in Table 6.1. In this table, the angle of attack for the optimum shapes is given as $\alpha$, and $\alpha_{C_{L_{Target}}}$ is the angle of attack obtained with the optimum shapes at the target $C_L$. $C_L$ is included in the objective function, and the area constraint is satisfied at each iteration. Therefore, the number of iterations presented in the table is equal to the total number of CFD (flow solver + adjoint solver) evaluations required for convergence. As observed in Table 6.1, the smallest difference in drag reduction between each turbulence model is observed for the FFD, whereas the largest difference is obtained with the B-Spline parameterization. Another finding is that the number of iterations (i.e. computational cost) required to converge is almost constant with respect to different turbulence models for the B-Spline and Hicks-Henne techniques. With the FFD technique, the SST turbulence model requires the least number of iterations

Table 6.1. Deterministic optimization results.

| Optimization Case | $C_L$ | $C_D$ | $\Delta C_D$ (counts) | Area | # of Iterations | $\alpha$ (°) | $\alpha_{C_{L_{Target}}}$ (°) |
|---|---|---|---|---|---|---|---|
| Original (SA) | 0.824 | 0.0209 | - | 0.0778 | - | 2.92 | - |
| Original (SST) | 0.825 | 0.0217 | - | 0.0778 | - | 3.06 | - |
| B-Sp, 20cp, SA | 0.821 | 0.0128 | 81 | 0.0795 | 63 | 3.34 | 3.38 |
| B-Sp, 20cp, SST | 0.813 | 0.0130 | 87 | 0.0790 | 62 | 3.47 | 3.62 |
| H-H, 256bf, SA | 0.823 | 0.0133 | 76 | 0.0813 | 21 | 2.94 | 2.95 |
| H-H, 256bf, SST | 0.827 | 0.0137 | 80 | 0.0815 | 22 | 3.08 | 3.06 |
| FFD, 2x40, SA | 0.807 | 0.0128 | 81 | 0.0794 | 14 | 2.93 | 3.08 |
| FFD, 2x40, SST | 0.809 | 0.0137 | 80 | 0.0793 | 7 | 3.07 | 3.28 |

to converge, which corresponds to a significant reduction of computational cost. The slight deviations from the target $C_L$ is observed for the optimal shapes for the B-Spline and Hicks-Henne techniques with both turbulence models, and for the FFD technique with the SST model due to the inclusion of $C_L$ in the objective function.

Figure 6.4(a) and 6.4(b) present the original and optimal shapes and their pressure distributions obtained with B-Spline as the shape parameterization technique for different turbulence models. There is a slight difference on the upper surface of the optimal shapes between $x/c = 0.6$ and 0.8, which is also reflected in the pressure distributions. The strength of the shock wave is reduced on the optimal shapes for both turbulence models.

The original and optimal shapes and their $C_p$ distributions obtained with the Hicks-Henne technique for different turbulence models are shown in Figure 6.5. The optimal shapes and the pressure distributions show a similar trend for each turbulence model. The shock wave strength is reduced with both turbulence models; however, a slight difference in $C_p$ can be observed downstream of the shock between the two turbulence models.

Figure 6.6 includes the original and optimal shapes and their $C_p$ distributions with the FFD technique for different turbulence models. Figure 6.6(a) shows that the optimal shapes obtained with each turbulence model are very similar. Figure 6.6(b) presents $C_p$

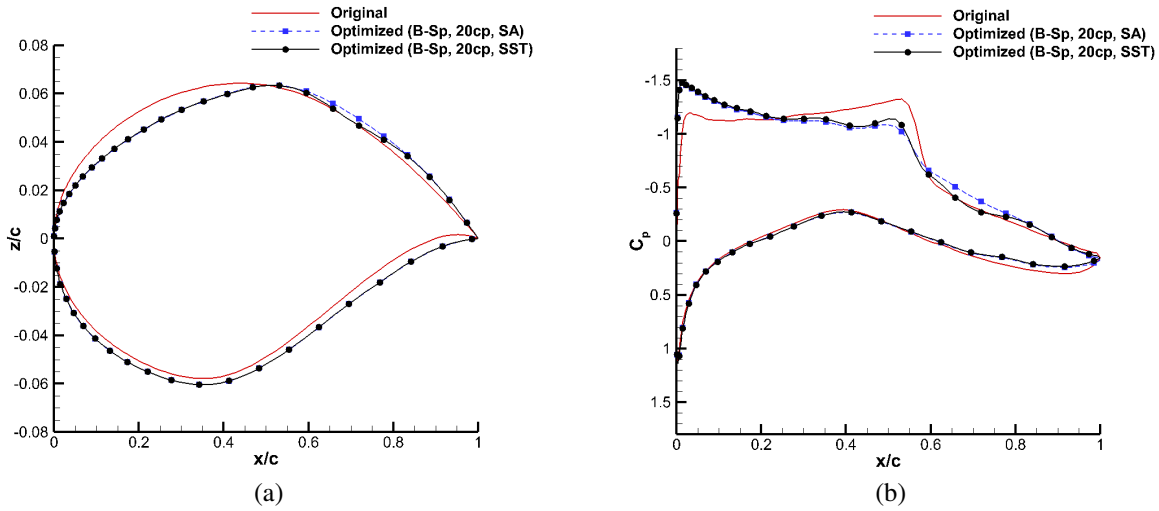


(a) (b)

Figure 6.4. Deterministic optimization results obtained with the B-Spline approach with the SA and SST models. a) Airfoil shapes. b) Pressure distributions.

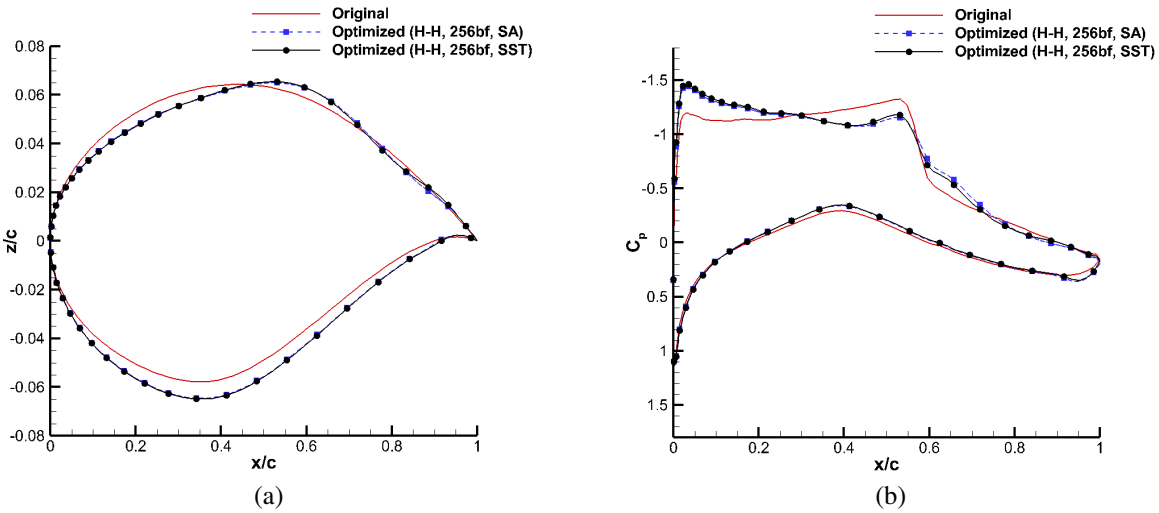


(a) (b)

Figure 6.5. Deterministic optimization results obtained with the Hicks-Henne approach with the SA and SST models. a) Airfoil shapes. b) Pressure distributions.

distributions of optimal shapes, which are similar except for the shock region and the downstream of the shock. With FFD, the SA model seems to produce a weaker shock, even though the airfoil shapes are very similar.

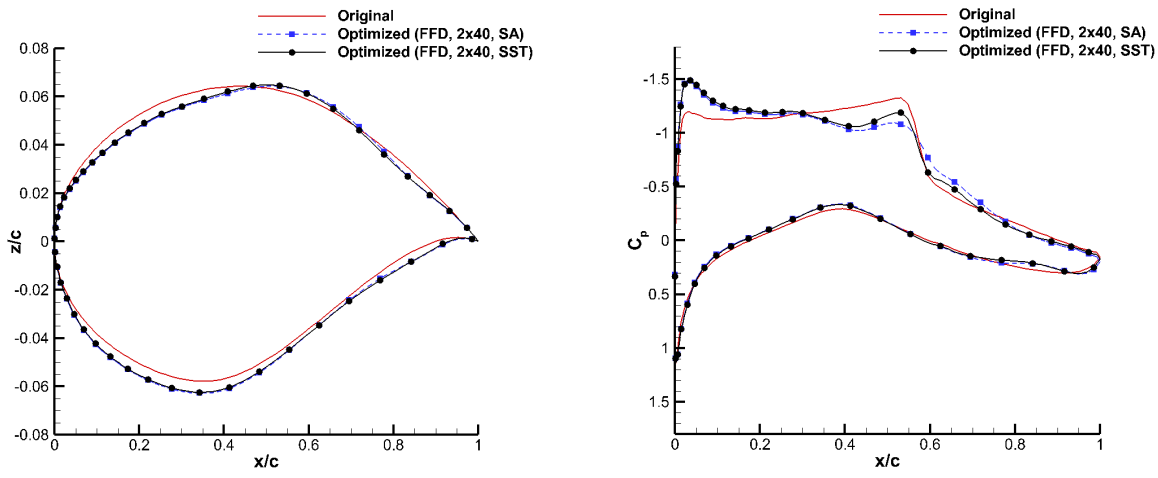


Figure 6.6. Deterministic optimization results obtained with the FFD approach with the SA and SST models. a) Airfoil shapes. b) Pressure distributions.

Figure 6.7 shows the original and optimal shapes obtained by using different shape parameterization techniques with the SA turbulence model and the corresponding pressure distributions. The airfoil shapes obtained with each shape parameterization technique show differences in different regions, which also affects the pressure distribution. This difference is especially recognized for the top surface B-Spline results when compared to the results of two other shape parameterization techniques. Figure 6.8 shows the original and optimal shapes obtained by using different shape parameterization techniques with the SST turbulence model and the corresponding $C_p$ distributions. Similar to the results of the SA model, the optimal shapes are different, with B-Spline having the largest difference for the top surface.

Overall, the results presented in this section show that, for deterministic optimization, shape parameterization techniques have a larger impact on the optimum shape and the number iterations required to converge than the effect of the specific turbulence model used.

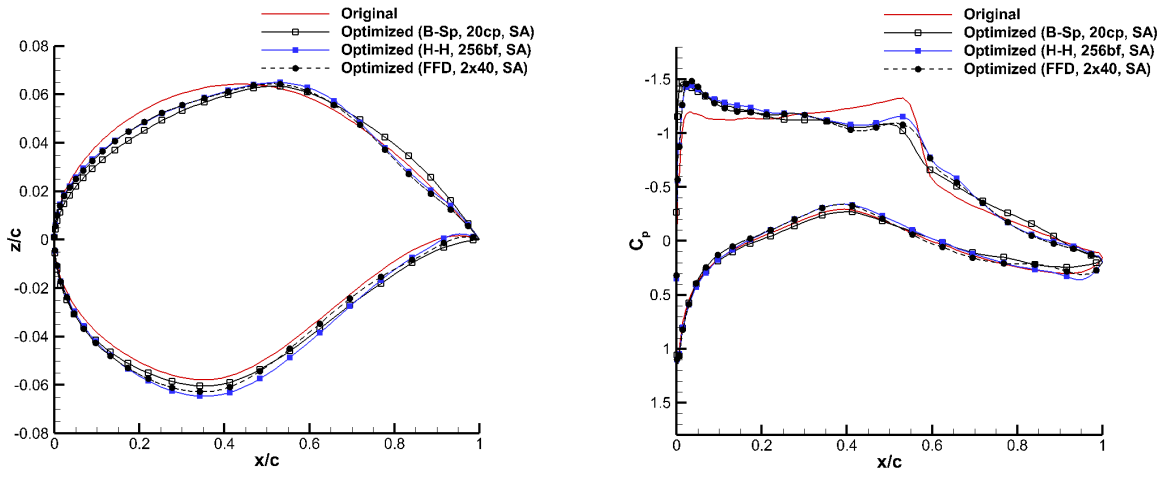


Figure 6.7. Deterministic optimization results obtained with the SA model with different shape parameterization techniques. a) Airfoil shapes. b) Pressure distributions.

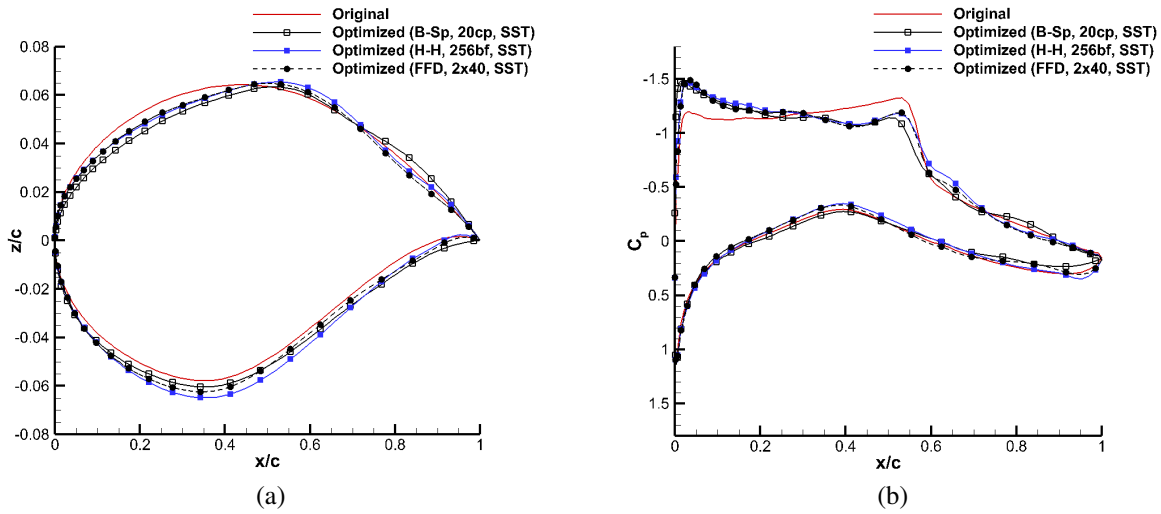


Figure 6.8. Deterministic optimization results obtained with the SST model with different shape parameterization techniques. a) Airfoil shapes. b) Pressure distributions.

## 6.3. ROBUST OPTIMIZATION

The impact of turbulence models and shape parameterization techniques on the computational cost, optimal shape and its performance obtained with robust optimization under uncertainty is investigated.

**6.3.1. Problem Statement.** The robust design procedure is applied to the same RAE2822 case studied for deterministic optimization; however, the Mach number is considered a uniformly distributed uncertain variable within the interval [0.725, 0.743]. The settings for each shape parameterization technique were determined in a previous parametric study [3] described in Appendix C, which gave the most effective robust optimum design with the minimum computational cost. Specifically, the shape parameterization techniques include: (1) B-Spline curves with 20 control points, (2) Hicks-Henne with 256 bump functions and $t_2 = 10$ (the width of the function) with the function amplitude limit set to [-0.01, 0.01] at each iteration, and (3) FFD with 2x20 control lattice with the size of $[-0.1, 0.1]$ in $z$ direction. For FFD, the boundaries of each control point are set as $[0.25z_i, 1.75z_i]$ where $z_i$ is the $z$ coordinate of $i^{th}$ control point. For robust design, a cosine distribution (CoD) is used for the spacing of design variables over the geometry for B-Spline curves and Hicks-Henne bump functions. Uniform distribution is utilized for the FFD technique. The $x$ location of the design points based on this cosine distribution are obtained with Equation (6.12):

$$\frac{x}{c} = \frac{(1 - cos\beta)}{2}, \quad 0 \leq \beta \leq \pi. \tag{6.12}$$

For robust optimization, the weighted objective function is formulated to minimize the mean and the variance of $C_D$ simultaneously, while keeping the mean of target $C_L$ constant:

$$minimize \quad W_1 \left( \frac{\mu_{C_D}}{\mu_{C_{D_{ref}}}} \right) + W_2 \left( \frac{\sigma_{C_D}}{\sigma_{C_{D_{ref}}}} \right)^2 + W_3 \left( \frac{\mu_{C_{L_{\text{Target}}}} - \mu_{C_L}}{\mu_{C_{L_{ref}}}} \right)^2 \tag{6.13}$$

where the weights $W_1$, $W_2$, and $W_3$ are 0.333, 0.333, and 0.334, respectively. $\mu_{C_{D_{ref}}}$ is $3.33 \times 10^{-3}$, $\sigma_{C_{D_{ref}}}$ is 0.001, and $\mu_{C_{L_{ref}}}$ is 0.150. The weights identify the contribution of each term to the objective function and the reference values are utilized to bring the magnitude of values in each term to the same level. The contribution of each term to the objective function is investigated on the test cases, and the weights of the optimum case are

utilized for this study. The contribution of each term to the objective function is investigated in terms of their percentage on the test cases, and the weights of the optimum case are utilized for this study. The mean of target $C_L$ is defined as 0.824, and the optimization algorithm is started with $\alpha = 2.92^\circ$ for the SA turbulence model and $\alpha = 3.06^\circ$ for the SST turbulence model as an initial value. In this formulation, the first term is related to the optimization of the mean performance (i.e., the minimization of the mean of the drag coefficient), the second term is intended to minimize the variance of the design under the variation of the Mach number (i.e., the minimization of the variance of the drag coefficient), and the third term is used for the implementation of the $C_L$ constraint.

**6.3.2. Robust Optimization Results.** The statistical performance metrics of the robust optimization at a target $C_L$ of 0.824 are given in Table 6.2. Similar to deterministic design, $C_L$ is included in the objective function, and the area constraint is satisfied at each iteration in robust design. Consequently, since the number of samples required to obtain the mean and the variance of $C_D$ and $C_L$ with stochastic expansions is $N_s$ (6 for this study), the number of total CFD evaluations is $N_s$ times the number of iterations required to converge for robust design. The highest $\mu_{C_D}$ and $\sigma_{C_D}$ reduction is observed for the Hicks-Henne technique with the SST model corresponding to 84 and 32 drag counts, respectively. Another observation is that the number of iterations (i.e. computational cost) required to converge significantly varies based on the shape parameterization technique. On the other hand, it stays constant for each turbulence model for the Hicks-Henne and FFD parameterizations. Among all shape parameterization techniques, FFD requires the minimum number of iterations to converge for both turbulence models. It should be noted that the computational time per iteration for each shape parameterization technique is approximately the same regardless of the number of design variables, since sensitivities are obtained from an adjoint-solution and the design variables in this study are considered deterministic.

Table 6.2. Robust optimization results for airfoils obtained at $\mu_{C_L} = 0.824$ with the Hicks-Henne (H-H), B-Spline (B-Sp), and FFD shape parameterization techniques and the SA and SST turbulence models.

| Optimization Case | $\mu_{C_D}$ | $\sigma_{C_D} \times 10^3$ | $\Delta\mu_{C_D}$ (cts) | $\Delta\sigma_{C_D}$ (cts) | Area | # of Iterations | $\alpha$ (°) |
|---|---|---|---|---|---|---|---|
| Original (SA) | 0.02125 | 2.88 | - | - | 0.07785 | - | 2.92 |
| Original (SST) | 0.02222 | 3.51 | - | - | 0.07785 | - | 3.06 |
| B-Sp, 20cp, SA | 0.01466 | 0.65 | 66 | 22 | 0.07919 | 88 | 3.48 |
| B-Sp, 20cp, SST | 0.01482 | 0.93 | 74 | 26 | 0.07874 | 74 | 3.43 |
| H-H, 256bf, SA | 0.01375 | 0.30 | 75 | 26 | 0.08179 | 36 | 2.96 |
| H-H, 256bf, SST | 0.01380 | 0.33 | 84 | 32 | 0.08113 | 37 | 3.09 |
| FFD, 2x20, SA | 0.01348 | 0.68 | 69 | 22 | 0.07975 | 13 | 2.93 |
| FFD, 2x20, SST | 0.01413 | 0.60 | 81 | 29 | 0.08039 | 14 | 3.07 |

By examining the results of the Hicks-Henne and FFD techniques individually, one can see a small difference in $\sigma_{C_D}$ between the SA and SST models. However, a significant difference in the same quantity can be noticed when the values obtained with these two shape parameterization techniques for the same turbulence model are compared. This may imply that the shape parameterization has more impact on the robustness of the final design than the specific turbulence model used.

The original and optimized shapes obtained with B-Spline parameterization with each turbulence model can be seen in Figure 6.9. There is a large difference between the optimized shapes and the original RAE2822 shape; however, the optimized shapes with different turbulence models are very similar. Figure 6.10 presents the $C_p$ distributions of original and optimized shapes with the B-Spline technique with each turbulence model at a target $C_L$ of 0.824 at $M_{nominal}$ (0.734) and $M_{max}$ (0.743), corresponding to the mean and maximum of the Mach number interval that is considered in this study. At both Mach numbers, the pressure distributions obtained with different turbulence models are close to each other and the strength of the shock wave is reduced over the optimized shapes. The shock wave is weakened more at $M_{nominal}$ than at $M_{max}$.

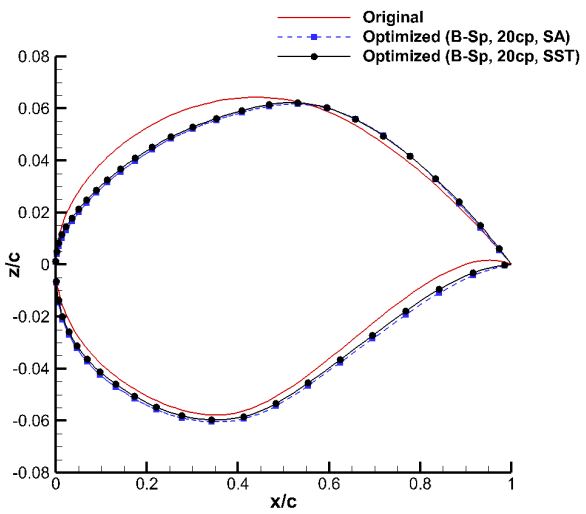


Figure 6.9. The comparison of original and optimized shapes (B-Spline, Robust design).

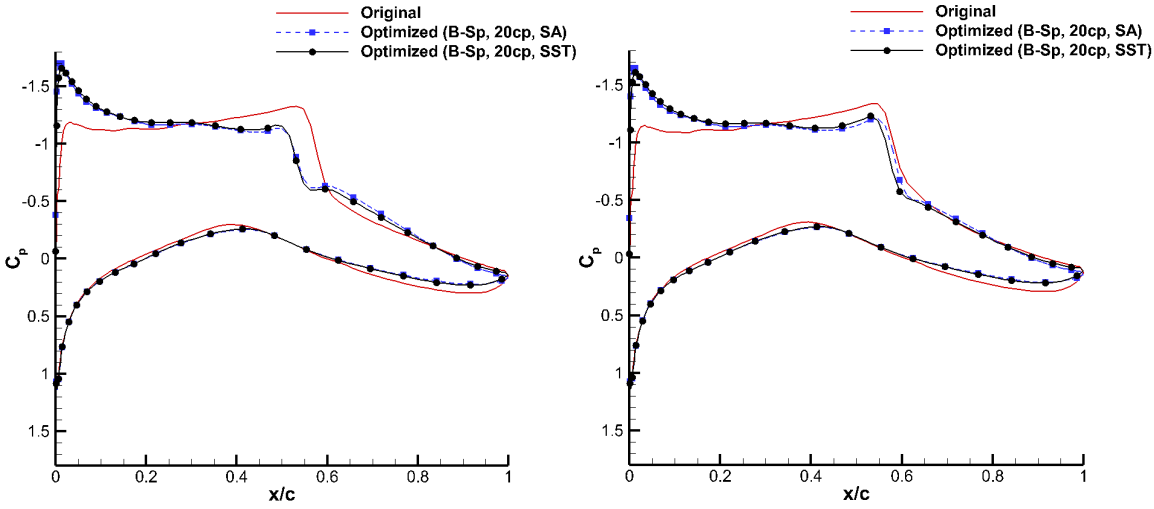


Figure 6.10. The $C_p$ distributions for the original and the optimum shapes at $C_L = 0.824$ (B-Spline, Robust design). a) $C_p$ at $M_{nominal}$. b) $C_p$ at $M_{max}$.

Figure 6.11 shows the original and optimized shapes with the Hicks-Henne technique with each turbulence model. There is a slight difference between the two optimized shapes on the lower surface between the leading edge and $x/c = 0.4$. The pressure distributions of original and optimized shapes with Hicks-Henne parameterization with two turbulence models at $M_{nominal}$ and $M_{max}$ for $C_L = 0.824$ are shown in Figure 6.12. At both Mach

numbers, the strength of the shock wave is reduced with optimized shapes. Similar to B-Spline cases, the shock wave is weakened more at $M_{nominal}$ than at $M_{max}$. The slight difference between optimum shape pressure distributions can be seen on the lower surface where the shapes are different.

Figure 6.13 presents the original and optimized shapes with the FFD technique with both turbulence models. As observed for the other two shape parameterization techniques, the different turbulence models provide very similar optimized shapes with the FFD technique. Figure 6.14 shows the $C_p$ distributions of original and optimized shapes with the FFD technique with two turbulence models at $M_{nominal}$ and $M_{max}$ for $C_L = 0.824$. At $M_{nominal}$, the $C_p$ distributions of the optimized shapes with different turbulence models are slightly different at the shock location than they are at $M_{max}$.

The original and optimized shapes with the B-Spline, Hicks-Henne and FFD techniques with the SA model are presented in Figure 6.15. Three optimized shapes can be seen to be different than the original shape. The optimized shapes with the Hicks-Henne and FFD techniques are thicker than the optimized shape with the B-Spline technique, which is significantly different than the other two optimum shapes. In addition, optimized shapes

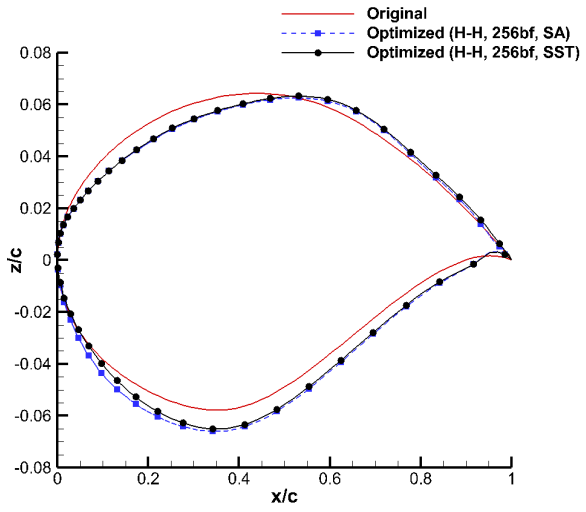


Figure 6.11. The comparison of original and optimized shapes (Hicks-Henne, Robust design).

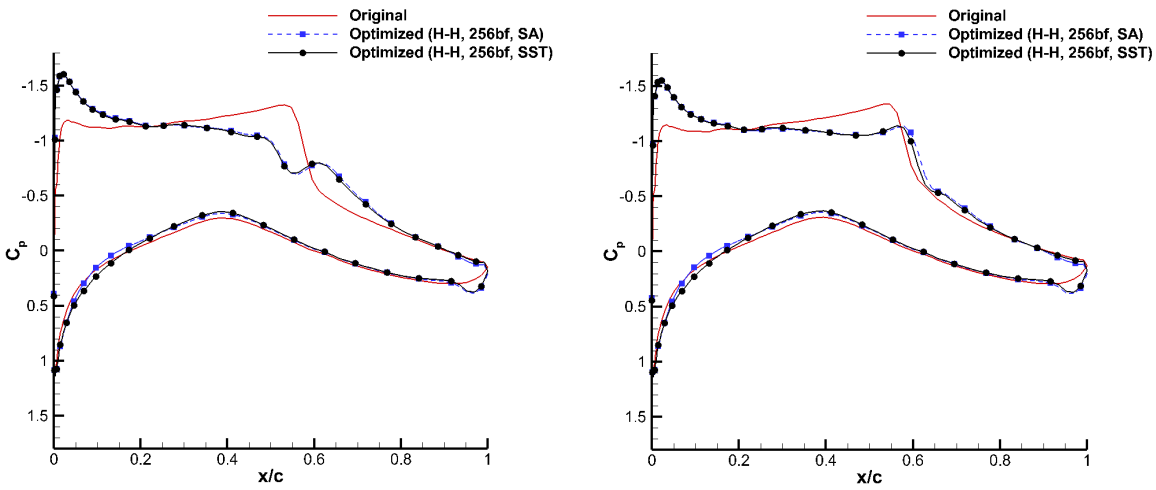


Figure 6.12. The $C_p$ distributions for the original and the optimum shapes at $C_L = 0.824$ (Hicks-Henne, Robust design). a) $C_p$ at $M_{nominal}$. b) $C_p$ at $M_{max}$.

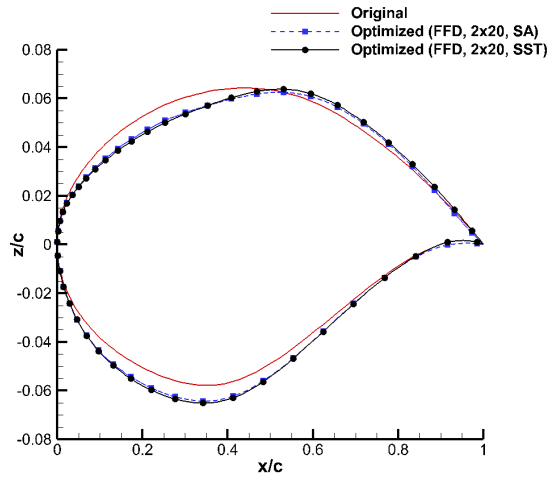


Figure 6.13. The comparison of original and optimized shapes (FFD, Robust design).

with Hicks-Henne and FFD parameterizations are very similar in the vicinity of the leading edge for both upper and lower surfaces; however, the Hicks-Henne shape deviates from the other two shapes at the trailing edge with a larger camber. Figure 6.16 shows the pressure distributions of the original and optimized shapes with the B-Spline, Hicks-Henne, and

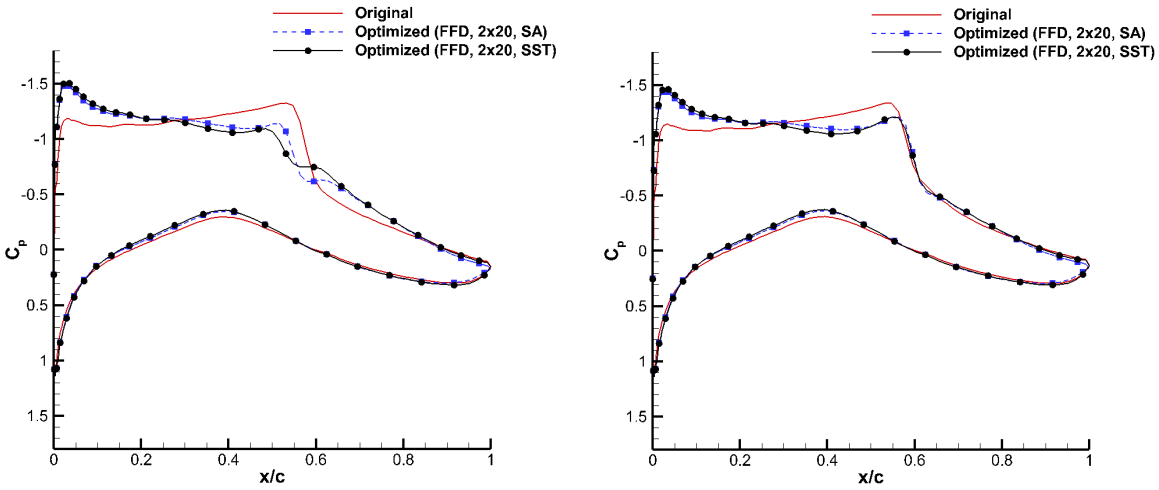


Figure 6.14. The $C_p$ distributions for the original and the optimum shapes at $C_L = 0.824$ (FFD, Robust design). a) $C_p$ at $M_{nominal}$. b) $C_p$ at $M_{max}$.

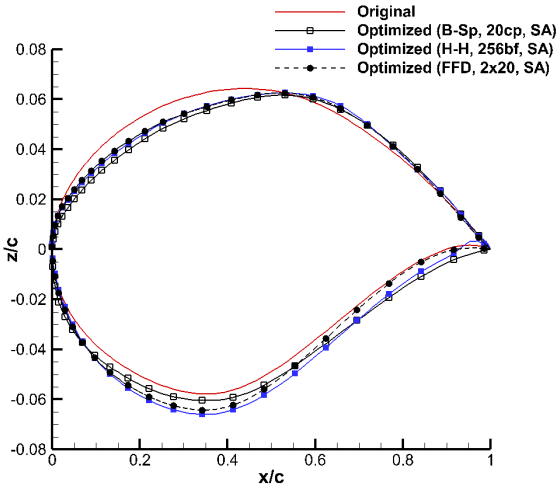


Figure 6.15. The comparison of original and optimized shapes (SA model, Robust design).

FFD techniques with the SA model at $C_L = 0.824$ for $M_{nominal}$ and $M_{max}$. The effect of the trailing edge camber on the pressure distribution can be seen for the Hicks-Henne shape. The pressure distributions vary mostly in the shock region and on the lower surface.

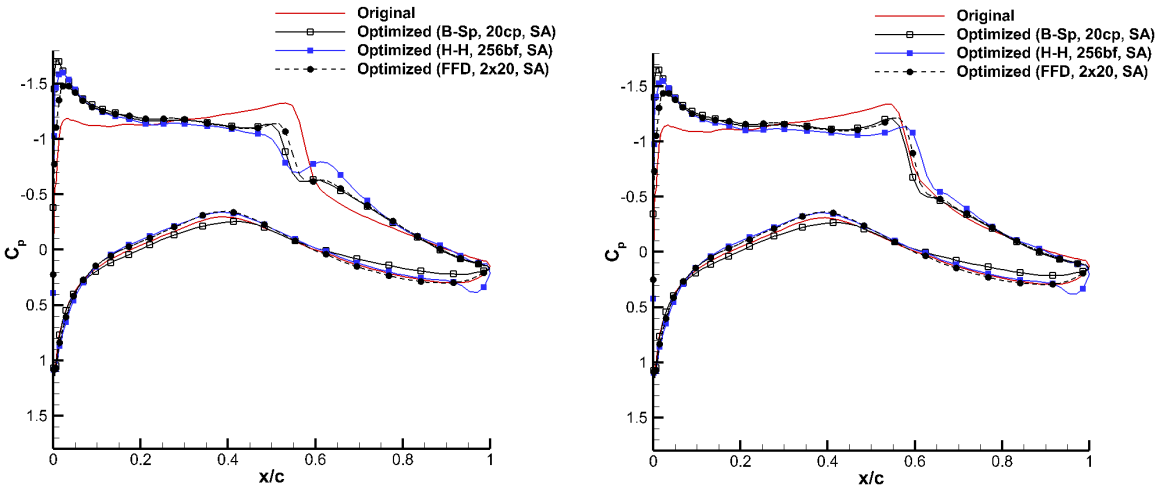


Figure 6.16. The comparison of the $C_p$ distributions for the original and optimum shapes at $C_L = 0.824$ (SA model, Robust design). a) $C_p$ at $M_{nominal}$. b) $C_p$ at $M_{max}$.

The original and optimized shapes with the B-Spline, Hicks-Henne, and FFD techniques with the SST model are presented in Figure 6.17. Three optimized shapes are different than the original shape. Similar to the SA results, the optimized shapes with the Hicks-Henne and FFD techniques are thicker than the optimized shape with the B-Spline technique. The Hicks-Henne shape has a high trailing edge camber. Figure 6.18 shows the pressure distributions of the original and optimized shapes with the B-Spline, Hicks-Henne, and FFD techniques with the SST model at $M_{nominal}$ and $M_{max}$ at $C_L = 0.824$. Similar to the SA model results, the $C_p$ distributions of optimized shapes with three shape parameterization techniques differ in the shock region and on the lower surface.

Overall, the detailed shape and pressure distribution analyses performed in this section indicate that the effect of the shape parameterization on the optimum shape and the associated aerodynamic characteristics is larger than the effect of the turbulence model in robust optimization. This is consistent with the observations made for deterministic optimization.

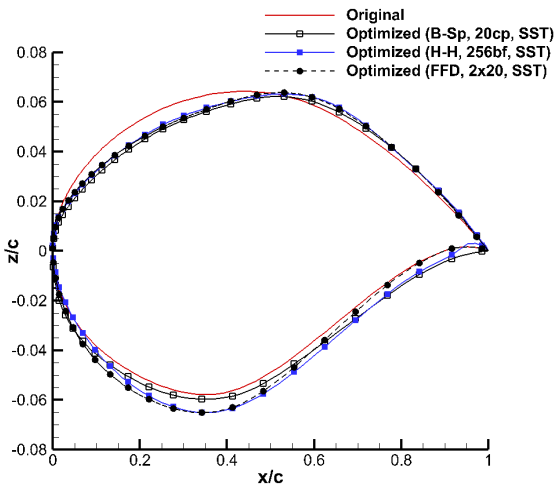


Figure 6.17. The comparison of original and optimized shapes (SST model, Robust design).

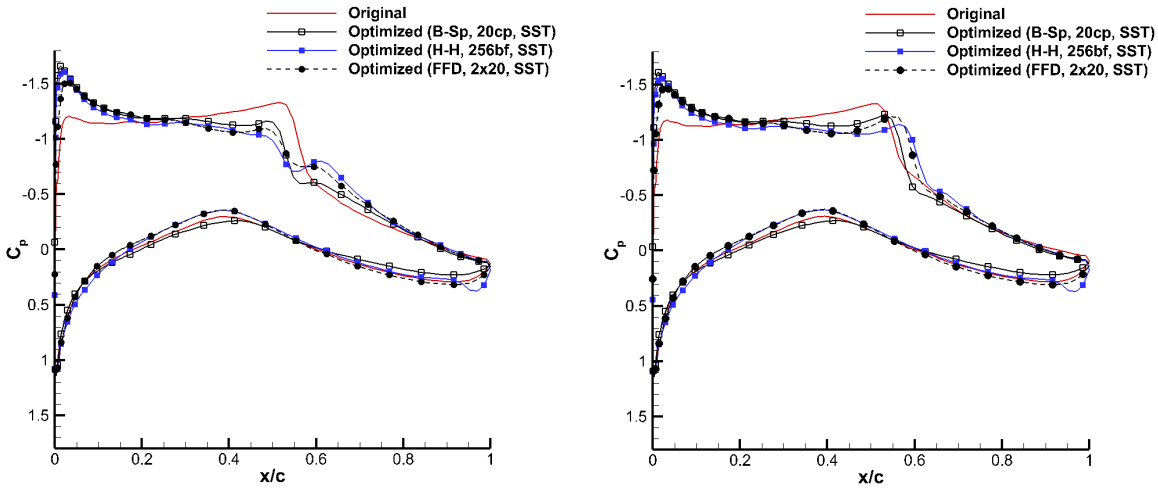


Figure 6.18. The comparison of the $C_p$ distributions for the original and optimum shapes at $C_L = 0.824$ (SST model, Robust design). a) $C_p$ at $M_{nominal}$. b) $C_p$ at $M_{max}$.

## 6.4. COMPARISON BETWEEN ROBUST AND DETERMINISTIC OPTIMIZATION

In deterministic aerodynamic design, the airfoil shape was optimized to minimize the drag coefficient at a target $C_L$ for a certain Mach number with the angle of attack taken as a design variable. However, the performance of the optimized shape can significantly

degrade if the Mach number deviates from its design point value in transonic flow. In robust aerodynamic design, the objective was to minimize the mean ($\mu_{C_D}$) and the variance ($\sigma^2_{C_D}$) of the drag coefficient at a target mean lift coefficient value ($\mu_{C_{L_{\text{Target}}}}$) to achieve robustness in the performance to the variation of the Mach number over a specified range. The number of iterations required to converge is greater with robust design than it is when using deterministic optimization with the Hicks-Henne and B-Spline techniques for both turbulence models and with the FFD technique for the SST model. The number of total CFD evaluations is equal to the number of iterations required to converge in deterministic design, whereas the number of total CFD evaluations is $N_s$ times the number of iterations required to converge for robust design, as explained in Section 4. Therefore, the computational cost of robust design per optimization iteration is six times higher than the cost of deterministic optimization. In this section, the difference between the performance of the deterministic and robust designs is demonstrated over the uncertain Mach number range. The effects of the shape parameterization technique and the turbulence model are also investigated.

In Figure 6.19, the drag coefficient of the original airfoil shape, deterministic design, and robust design are presented for the Hicks-Henne shape parameterization for both turbulence models. The drag coefficient values of each shape are evaluated at the target $C_L$ value of 0.824. The $C_D$ of baseline RAE2822 shape is the highest over the entire Mach number range for each turbulence model. At $M = 0.734$, which is the deterministic design point, the $C_D$ of the deterministic design is approximately 85 drag count for both SA and SST turbulence models. There is a significant drop in $C_D$ until it reaches the deterministic design Mach number and then a significant rise occurs as the Mach number increases. This trend clearly shows that the deterministic optimization performs relatively poorly at the off-design Mach numbers. The increase in $C_D$ is more dramatic with the SST model than it is with the SA model which indicates that the turbulence model plays a significant role in deterministic design at higher off-design Mach numbers. On the other hand, the airfoil obtained with the robust optimiza-

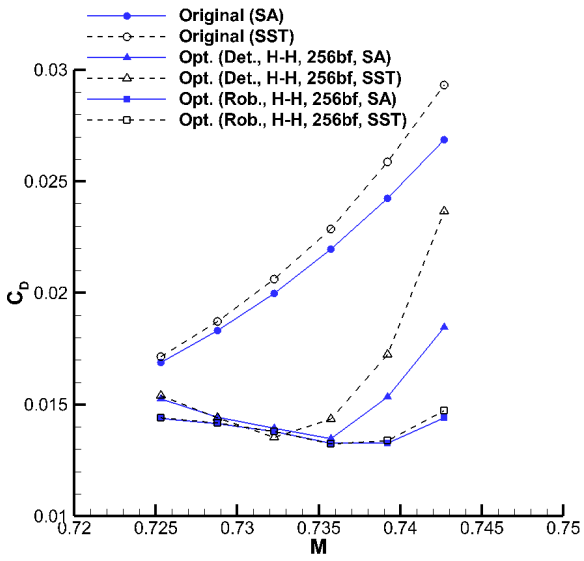


Figure 6.19. $C_D$ comparison of original and optimum shapes (deterministic and robust) under varying Mach number at $C_L = 0.824$ (Hicks-Henne technique).

tion approach exhibits a relatively flat $C_D$ curve over the Mach number range, with a slight increase starting from $M = 0.74$. The shape obtained with robust optimization achieves 40 drag count reduction with the SA model and 89 drag count reduction with the SST model, compared to deterministic design at $M_{max} = 0.743$. Overall, robust design performs better than deterministic design in terms of robustness and mean performance over the Mach number range that is considered.

In Figure 6.20, the drag coefficients of the original, deterministic design, and robust design are presented for the B-Spline shape parameterization for both turbulence models. The drag coefficient values of each shape are evaluated at the target $C_L$ value of 0.824. The $C_D$ of deterministic design decreases until $M = 0.732$ and then increases dramatically for each turbulence model. The robust design follows a relatively flat $C_D$ curve unlike the deterministic design over the Mach number range. At $M_{max} = 0.743$, the shape obtained with robust optimization achieves 8 drag count reduction with the SA model and 34 drag count

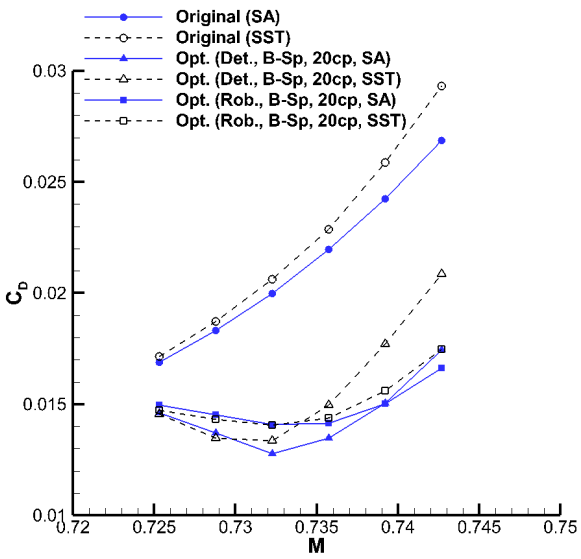


Figure 6.20. $C_D$ comparison of original and optimum shapes (deterministic and robust) under varying Mach number at $C_L = 0.824$ (B-Spline technique).

reduction with the SST model compared to deterministic design. Similar to the Hicks-Henne technique, robust design has better performance than deterministic design in terms of robustness over the Mach number range considered for both turbulence models.

In Figure 6.21, the drag coefficient of the original, deterministic design (uniformly distributed 2x40 control lattice), and robust design (uniformly distributed 2x20 control lattice) is presented under varying Mach numbers with two turbulence models. Similar to the Hicks-Henne and B-Spline parameterizations, the drag coefficient values of each shape were evaluated at the target $C_L$ value of 0.824, and the $C_D$ of baseline RAE2822 shape is the highest of all Mach number values at each turbulence model. The $C_D$ of deterministic design increases significantly after $M = 0.732$ for each turbulence model. Similar to the Hicks-Henne and B-Spline techniques, robust design exhibits a relatively flat $C_D$ curve compared to deterministic design over the Mach number range. At the maximum Mach number of 0.743, the shape obtained with robust optimization achieves 35 drag count reduction with the SA model and 87 drag count reduction with the SST model compared to deterministic design.

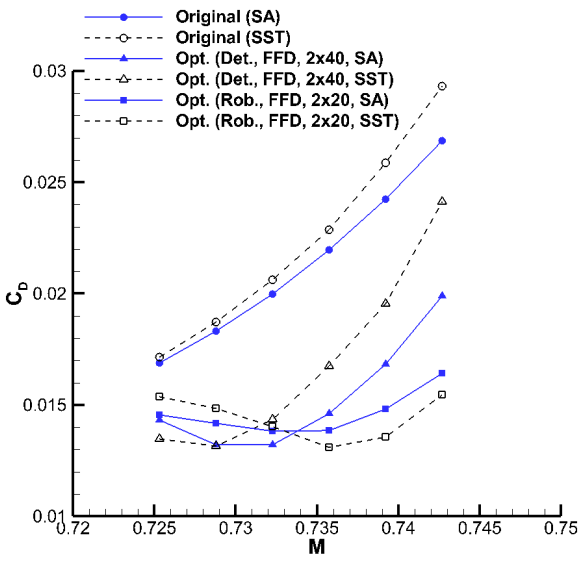


Figure 6.21. $C_D$ comparison of original and optimum shapes (deterministic and robust) under varying Mach number at $C_L = 0.824$ (FFD technique).

From Figure 6.22, it can be seen that the robust design obtained with the Hicks-Henne shape parameterization gives the best result in terms of the mean performance and robustness obtained over the Mach number range that is considered for both turbulence models. As a general observation, Figures 6.19 to 6.22 indicate that robust design tends to reduce the impact of the turbulence model selection on the optimum shape and performance, whereas the turbulence model becomes important for the deterministic design at off-design conditions. The effect of the shape parameterization technique on robust design is much more significant than the effect of the turbulence model. In Figure 6.23, the comparison of original and optimized shapes for both deterministic and robust design with Hicks-Henne parameterization, which is identified as the best approach for robust design, is presented for the SA model. For both designs, optimized shapes are similar in the vicinity of the leading edge; however, downstream geometries differ both for the upper and the lower surfaces. Robust design provides better performance under the variation of the Mach number, which is also reflected in the difference between the optimized shapes. Area constraint is satisfied with both designs.

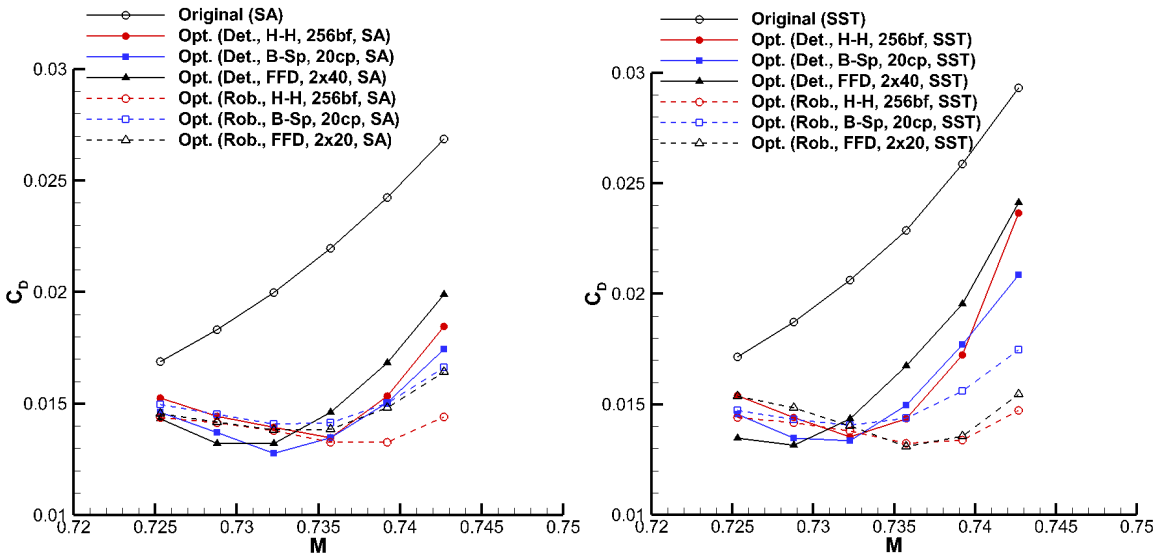


Figure 6.22. $C_D$ comparison of the original and optimum shapes (deterministic and robust) under varying Mach number at $C_L = 0.824$. a) SA model. b) SST model.

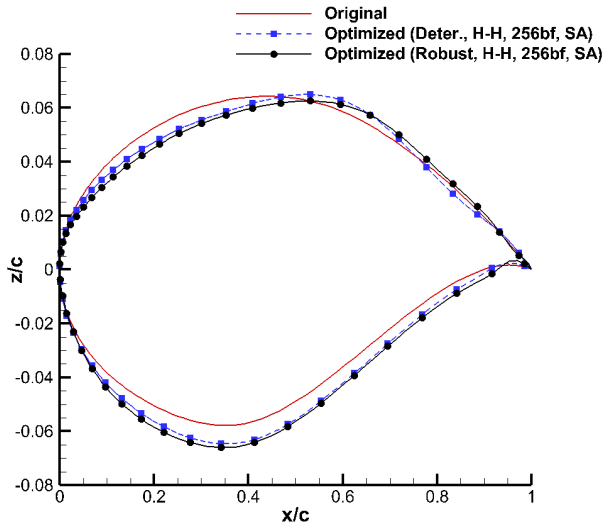


Figure 6.23. The comparison of original and optimized (deterministic and robust) shapes.

Figure 6.24 shows the Mach number contours over optimized (deterministic and robust) and original shapes of RAE2822 at $M_{nominal}$ and $M_{max}$ at $C_L = 0.824$ for the best robust design case which was obtained with the Hicks-Henne parameterization and the

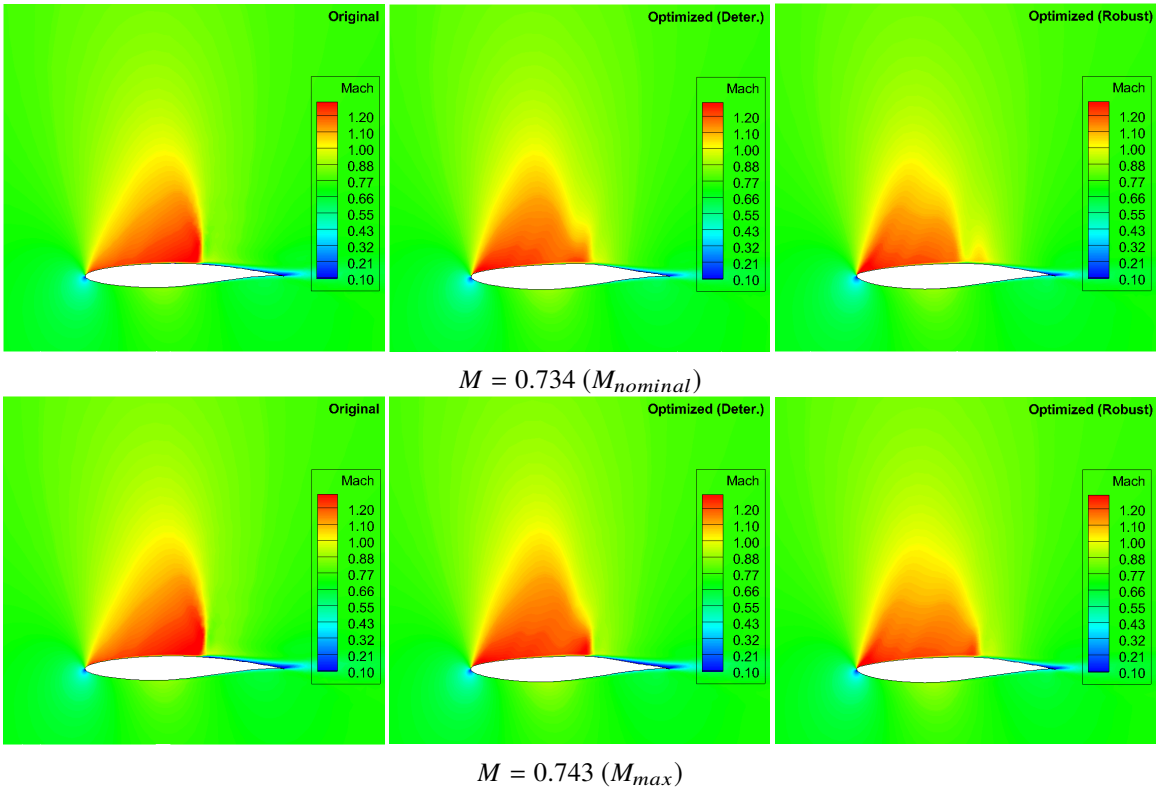


Figure 6.24. The Mach number contours at $C_L = 0.824$ over optimized and original shapes for the best robust design case (Hicks-Henne, SA model).

SA model. The strength of the shock wave is reduced with both deterministic and robust designs. However, the shock wave is weakened more with the robust design than it is with the deterministic design, especially at $M_{max}$. In Figure 6.25, the comparison of $C_p$ distributions of the optimal and original shapes at $M_{nominal}$ and $M_{max}$ are presented. These figures also verify the observations made from the presented contour plots.

Overall, the flatness of the $C_D$ over the varying Mach number with two turbulence models and three shape parameterization techniques in robust design shows that the robustness is significantly improved when compared to deterministic design. However, the robustness comes at the expense of a slight increase in $\mu_{C_D}$ when compared to the $C_D$ values obtained with the deterministic optimization.

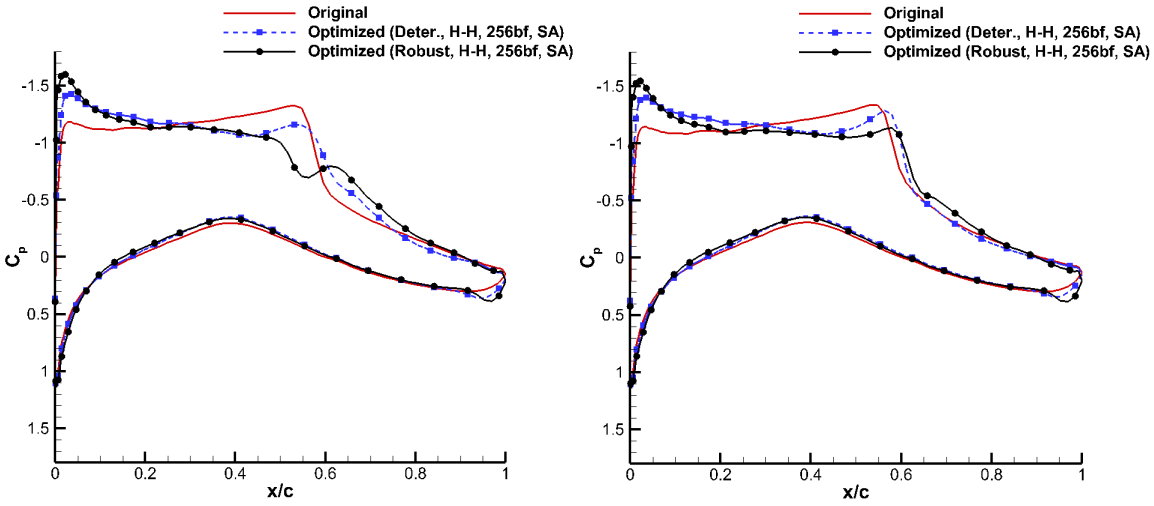


Figure 6.25. The comparison of $C_p$ over original and optimized shapes at $C_L = 0.824$ for the best robust design case (Hicks-Henne, SA model). a) $C_p$ at $M_{nominal}$. b) $C_p$ at $M_{max}$.

# 7. 3-D ROBUST AERODYNAMIC SHAPE OPTIMIZATION

## 7.1. SHAPE PARAMETERIZATION TECHNIQUE

In 3-D wing study, Free-Form Deformation (FFD) is utilized as shape parameterization technique. With this approach, the wing is embedded into the lattice box by constraining the control points to a plane. A three-dimensional space of $(l+1)\times(m+1)\times(n+1)$ uniformly distributed Bezier surface control points, $P_{i,j,k}$, are located around the wing and the control lattice box is created. The three-dimensional space is normalized to the unit domain $N(u,v,w)\in[0,1]\times[0,1]\times[0,1]$ by the following transformation equation;

$$u(x)=\frac{x-x_{min}}{x_{max}-x_{min}},\quad v(y)=\frac{y-y_{min}}{y_{max}-y_{min}},\quad w(z)=\frac{z-z_{min}}{z_{max}-z_{min}} \tag{7.1}$$

where $[x_{min},x_{max}]$, $[y_{min},y_{max}]$, and $[z_{min},z_{max}]$ are the intervals of control lattice in $x,y$, and $z$ directions, respectively. The deformation of the wing is defined as;

$$X(u(x),v(y),w(z))=\sum_{i=0}^{l}\sum_{j=0}^{m}\sum_{k=0}^{n}B_{i,l}(u(x))B_{j,m}(v(y))B_{k,n}(w(z))P_{i,j,k} \tag{7.2}$$

where $B_{i,l}(u(x))$, $B_{j,m}(v(y))$ and $B_{k,n}(w(z))$ are Bernstein polynomials and $P_{i,j,k}$ is the control point. The control point position is calculated with the following equation;

$$P_{i,j,k}=\left(x_{min}+\frac{i}{l}(x_{max}-x_{min}),y_{min}+\frac{j}{m}(y_{max}-y_{min}),z_{min}+\frac{k}{n}(z_{max}-z_{min})\right) \tag{7.3}$$

Bernstein polynomial, $B_{i,l}(u(x))$, is defined as;

$$B_{i,l}(u(x))=\binom{l}{i}(u(x))^{i}(1-u(x))^{(l-i)},\quad i=0,\ldots,l \tag{7.4}$$

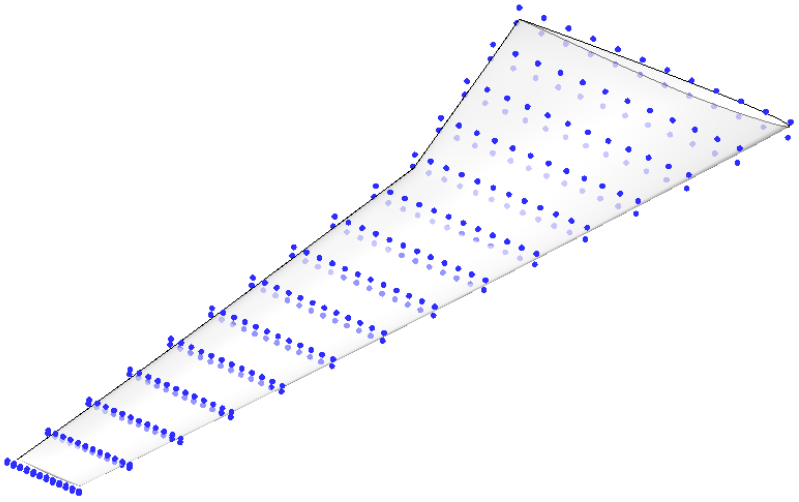

Figure 7.1. FFD lattice box with control points.

where $\binom{l}{i}$ is a binomial coefficient. The FFD box with the control points is shown in Figure 7.1.

FFD is a flexible and string shape parameterization method. Local deformation over the 3-D geometry is possible with the FFD technique.

## 7.2. DETERMINISTIC OPTIMIZATION

In deterministic optimization, the impact of turbulence models is investigated in terms of computational cost, the difference in the shape and performance of the final design. The deterministic optimization results are performed to make a comparison with the turbulence models used in robust optimization in terms of effectiveness and computational cost. The objective of deterministic optimization is to reduce the drag coefficient $C_D$ of the wing at a specified Mach number subject to a specified minimum lift coefficient $C_L$, and thickness constraints.

**7.2.1. Problem Statement.** The optimization of CRM wing is performed for steady, viscous, turbulent flow at a Mach number of 0.85 and Re number of $5 \times 10^6$. The shape parameterization technique is FFD with $24 \times 15 \times 2$ control lattice box used in the

previous studies [46]. FFD control lattice box used in this optimization problem is shown in Figure 7.1. The uniform distribution (UD) is implemented for the spacing of design variables over the geometry.

The angle of attack is defined as a design variable for all cases and $C_L$ constraint is included in the objective function, setting the target $C_L$ as 0.65. The angle of attack is constrained within the $[2.0°, 5.0°]$ range and the size of control lattice box is set to $[-1.0, 1.0]$ in $z$ direction at each iteration. Ten thickness constraints located at $[0.0\%, 11.1\%, 22.2\%, 33.3\%, 44.4\%, 55.5\%, 66.7\%, 77.8\%, 88.9\%, 100\%]$ of the span are defined with the non-dimensional values of $[0.223, 0.173, 0.131, 0.104, 0.0901, 0.0782, 0.067, 0.0569, 0.0471, 0.0374]$. The planform shape of the wing (wingspan, sweep angle and spanwise chord distribution) is kept the same at each optimization iteration. To prevent the change in spanwise twist distribution, the FFD control nodes at both upper and lower surfaces at the leading and trailing edges are fixed. The optimization algorithm is started with $\alpha = 3.56°$ for the SA model and $\alpha = 3.81°$ for the SST model as an initial value in order to match the target $C_L$. The weights are specified in the objective function within the interval $[0, 1]$ according to Equation 6.10. A weighted objective function is defined to include the $C_L$ constraint besides the main objective of the minimization of the $C_D$:

$$minimize \quad W_1 \left( \frac{C_D}{C_{D_{ref}}} \right)^2 + W_2 \left( \frac{C_{L_{Target}} - C_L}{C_{L_{ref}}} \right)^2 \tag{7.5}$$

where the weights $W_1$ and $W_2$ are 0.5, the reference scaling factor of the drag coefficient, $C_{D_{ref}}$, is 0.012 and the reference scaling factor of lift coefficient, $C_{L_{ref}}$, is 0.071. The reference factors are used as normalization factors to bring the magnitude of $C_L$ and $C_D$ terms to the same level so that the weights can be conveniently utilized to adjust the contribution of each term to the objective function. The contribution of each term to the objective function in terms of their percentage is investigated on test cases and the optimum combination of the weights is selected based on the test case results. It is important to

note that the pitching moment coefficient constraint is excluded in the current problem formulation; therefore, higher tail lift and trim drag may be required for the optimum configuration due to higher nose-up pitching moment.

**7.2.2. Deterministic Optimization Results.** The lift coefficient $C_L$ of the original shape is 0.65 for each turbulence model. It is determined based on a parametric study, which was performed to identify a target $C_L$ with significant difference in the drag coefficient obtained with each turbulence model over a Mach number range including the point value at which the deterministic optimization is performed. The $C_D$ comparison of original shapes under varying Mach number at a $C_L$ of 0.5, 0.6, and 0.65 is given in Figure 7.2. The selection of turbulence model plays an important role at a $C_L$ of 0.65, however the $C_D$ difference between two turbulence models is small at the $C_L$ of 0.5 and 0.6. Therefore, deterministic and robust optimization is performed at the target $C_L$ of 0.65 to investigate the impact of turbulence models in terms of computational cost, the difference in the shape and the performance of final design.

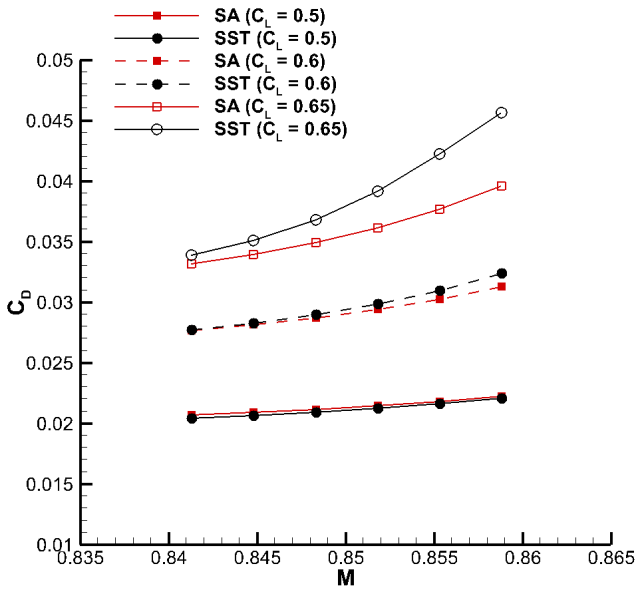


Figure 7.2. $C_D$ comparison of original shapes under varying Mach number at a $C_L$ of 0.5, 0.6, and 0.65.

The drag coefficient $C_D$ is 0.0356 obtained at $\alpha = 3.56°$ with SA and 0.0379 obtained at $\alpha = 3.81°$ with SST model. The numerical results of the optimized shapes are given in Table 6.1. In this table, the angle of attack for the optimum shapes is given as $\alpha$ and the angle of attack obtained with the optimum shapes at the target $C_L$ is $\alpha_{C_{L_{Target}}}$. The angle of attack obtained with the optimum shapes at the target $C_L$ is 3.51° for SA model and 3.71° for SST model. The lift coefficient $C_L$ is included in the objective function, and the thickness constraints satisfied at each iteration; therefore, the number of iterations presented in the table is equal to the total number of CFD (flow solver + adjoint solver) evaluations required for convergence. As it can be seen in the table that the difference in the drag reduction with SST is higher than SA model. This is expected as the $C_D$ of the original wing with SST model is 23 drag counts higher than the $C_D$ of original wing with SA model. This difference is reduced to 9 drag counts for the optimal shapes, which indicates that the impact of selection of turbulence model is reduced at the specified $C_L$. The computational cost is almost constant with respect to turbulence models.

Figure 7.3 shows the wing sections at eight spanwise locations for the original and optimal shapes obtained with each turbulence model. There is a noticeable difference between the optimal and original shapes at each station. The upper and lower surfaces of the optimal shapes are very similar for each turbulence model at stations A-D, however

Table 7.1. Deterministic optimization results obtained with SA and SST models at $C_L$ = 0.65.

| Optimization Case | $C_D$ | $\Delta C_D$ (cst) | $\alpha(°)$ | $\alpha_{C_{L_{Target}}}$ | # of Iterations |
|---|---|---|---|---|---|
| Original (SA) | 0.0356 | - | 3.56 | - | - |
| Original (SST) | 0.0379 | - | 3.81 | - | - |
| Optimum (SA) | 0.0302 | 54 | 3.58 | 3.51 | 21 |
| Optimum (SST) | 0.0311 | 68 | 3.82 | 3.71 | 18 |

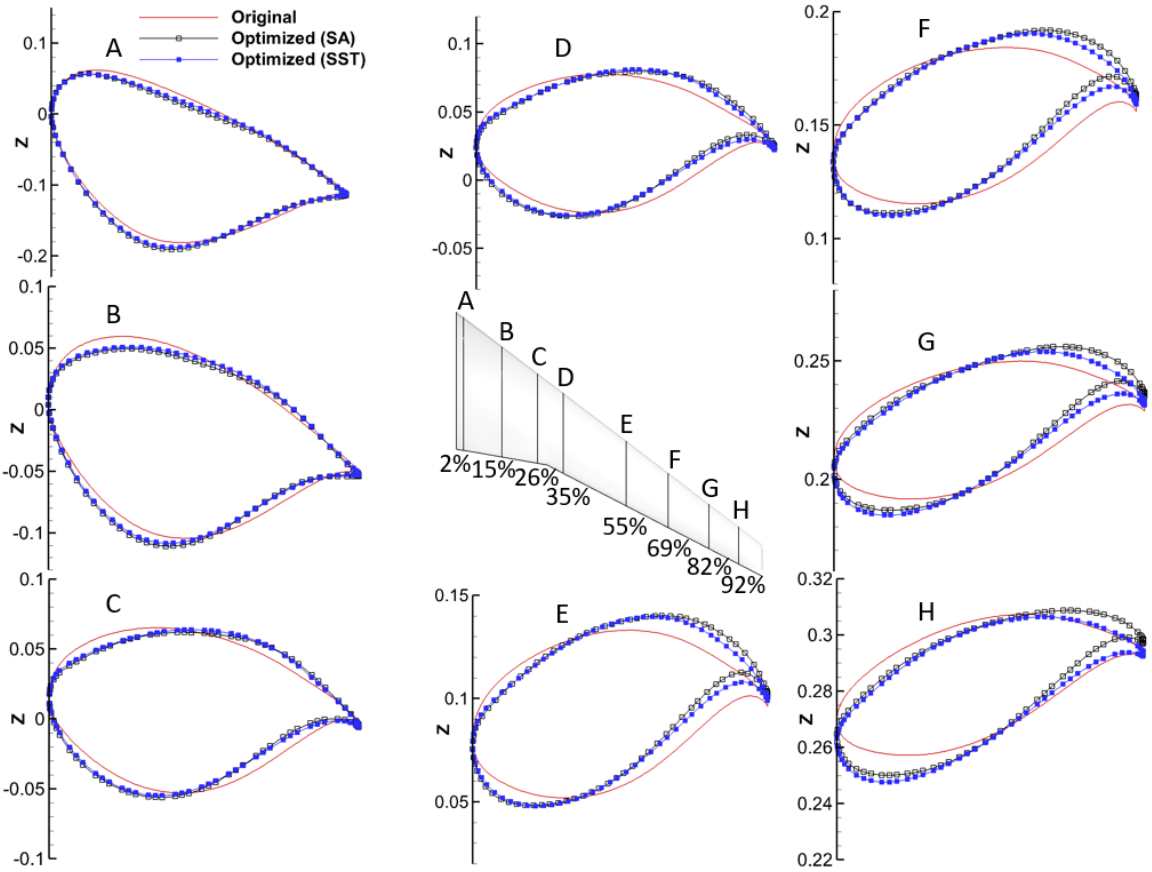


Figure 7.3. The comparison of the optimal and original shapes at selected spanwise stations.

the upper and lower surface of the optimal shapes nearby the trailing edge show slightly different trend at stations E-H. In addition, the upper and lower surface of the optimal shapes nearby the leading edge shows slightly different trend at stations G and H.

The comparison of $C_p$ distribution of the optimal and original shape for CRM wing at different spanwise stations are presented in Figure 7.4. The shock wave strength over the original shape is weakened for the optimized shapes, in particular at stations C, D and E. The difference in pressure distribution between two turbulence models is decreased significantly at stations C-F.

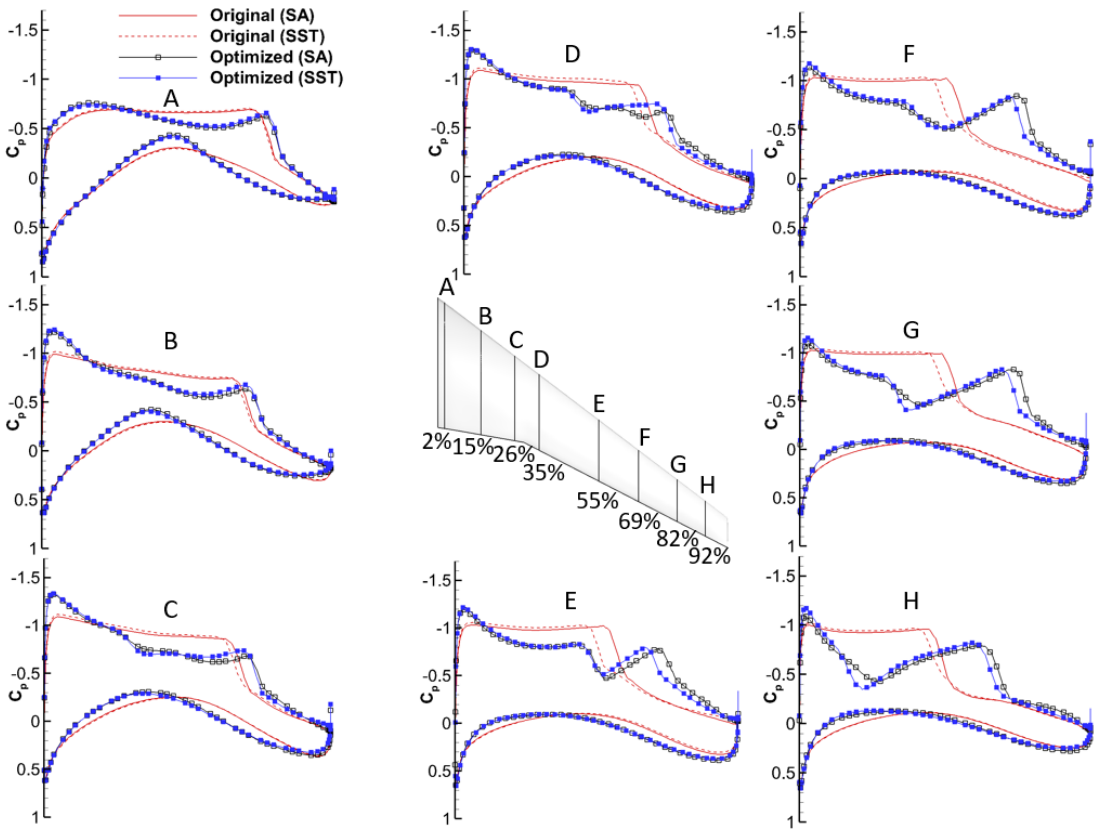


Figure 7.4. The comparison of $C_p$ distribution of the optimal and original shapes at selected spanwise stations.

The $C_p$ distribution contours of the optimal and original shapes are shown in Figure 7.5. The shock wave strength is significantly reduced for the optimal shapes with both turbulence models. A weak shock wave is observed in the vicinity of the trailing edge nearby the tip of wing with SA model.

Overall, the results presented in this section show that the difference in aerodynamic characteristic due to the selection of turbulence model is reduced significantly with deterministic optimization at the design Mach number. Also, the computational cost stays nearly constant with different turbulence models.

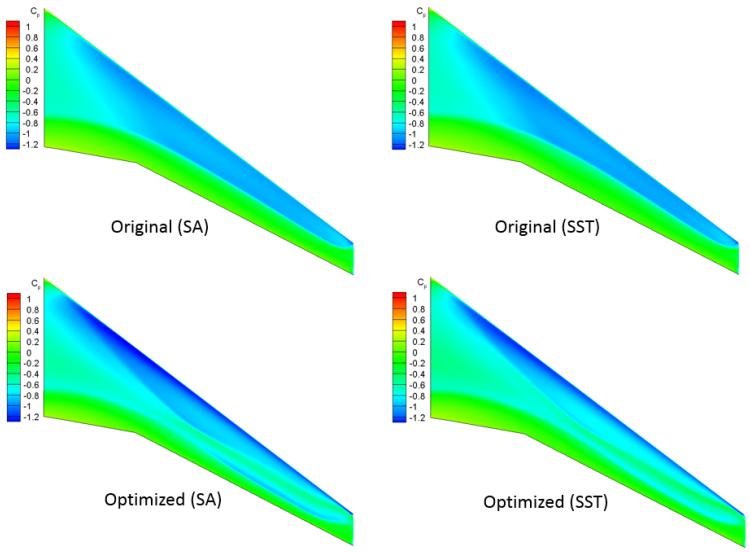


Figure 7.5. The contour showing the $C_p$ distribution over the optimized and original shapes of the CRM wing.

## 7.3. ROBUST OPTIMIZATION

The impact of turbulence models and the weight distribution in the objective function on the computational cost, optimal shape and its performance obtained with robust optimization under uncertainty is investigated.

**7.3.1. Problem Statement.** The robust design procedure is applied to the same CRM wing studied for deterministic optimization; however, Mach number is considered a uniformly distributed uncertain variable within the interval of $[0.827, 0.873]$. Similar to deterministic optimization, the shape parameterization technique is FFD with 24×15×2 control lattice box. The uniform distribution is utilized to distribute the control points over the wing geometry. The angle of attack is defined as a design variable within the interval of $[2°, 5°]$ and $C_L$ constraint is included in the objective function for a target mean $C_L$ of 0.65. The size of control lattice box is set to $[-1.0, 1.0]$ in $z$ direction at each iteration. The thickness contraints are located at $[0.0\%, 11.1\%, 22.2\%, 33.3\%, 44.4\%, 55.5\%, 66.7\%, 77.8\%, 88.9\%, 100\%]$ of the span defined with the non-dimensional values of $[0.223, 0.173, 0.131, 0.104, 0.0901, 0.0782, 0.0672, 0.0569, 0.0471, 0.0374]$. The wingspan, spanwise chord distribution, and

sweep angle of the wing are preserved at each optimization iteration. The FFD control points at both upper and lower surfaces at the leading and trailing edges are fixed in order to prevent the change in spanwise twist direction. For robust optimization, the weighted objective function is formulated to minimize the mean and variance of $C_D$ simultaneously, while keeping the mean of target $C_L$ constant:

$$minimize \quad W_1 \left( \frac{\mu_{C_D}}{\mu_{C_{D_{ref}}}} \right) + W_2 \left( \frac{\sigma_{C_D}}{\sigma_{C_{D_{ref}}}} \right)^2 + W_3 \left( \frac{\mu_{C_{L_{\text{Target}}}} - \mu_{C_L}}{\mu_{C_{L_{ref}}}} \right)^2 \tag{7.6}$$

where the weights, $W_1, W_2$ and $W_3$ are within the interval of $[0, 1]$ according to Equation 6.10. $\mu_{C_{D_{ref}}}$ is $1.85 \times 10^{-3}$, $\sigma_{C_{D_{ref}}}$ is $4.08 \times 10^{-3}$, and $\mu_{C_{L_{ref}}}$ is $1.49 \times 10^{-1}$. The weights identify the contribution of each term to the objective function and the reference values are used to bring the magnitude of values in each term to the same level. The impact of each term on the optimal shape and its performance, robustness, and computational cost is investigated by changing the weights in the objective function. The weights used in this study are given in Table 7.2 for each case. The $W_1, W_2$, and $W_3$ are set to 0.36, 0.323 and 0.317 for the mean-biased weighting (MBW), respectively. The $W_1, W_2$, and $W_3$ are set to 0.333, 0.333 and 0.334 for the equal weighting (EW), respectively. Variance-biased weighting (VBW) is performed at the $W_1$ of 0.3, the $W_2$ of 0.4, and the $W_3$ of 0.3. To match the target $C_L$, the optimization algorithm is began with $\alpha = 3.56°$ for the SA model and $\alpha = 3.81°$ for the SST model. In this formulation, the first term is related to the optimization of the mean performance (i.e. the minimization of the mean of the drag coefficient), the second term is used to minimize the variance of the design under the variation of Mach number (i.e. the minimization of the variance of the drag coefficient), and the last term is intended for the implementation of $C_L$ constraint.

**7.3.2. Robust Optimization Results.** The statistical performance metrics of the robust design at a target $C_L$ of 0.65 are given in Table 7.3. Similar to the deterministic optimization, $C_L$ is included in the objective function and the thickness constraints are

satisfied at each iteration in robust optimization. $N_s$ (6 for this study) is the number of samples required to obtain the mean and variance of $C_D$ and $C_L$ with stochastic expansions. The number of CFD evaluations is $N_s$ times the number of iterations required for convergence for robust design. The highest $\mu_{C_D}$ reduction is observed for the MBW case with SST model corresponding to 51 drag counts. Similarly, the highest $\sigma_{C_D}$ reduction is observed for the VBW case with SST model corresponding to 22 drag counts. The MBW and VBW cases provided the lowest $\mu_{C_D}$ and $\sigma_{C_D}$ with both turbulence models when the same quantities are compared for the same turbulence model. Another important observation is that the $\mu_{C_D}$ difference between SA and SST models reduced significantly for all optimization cases. In particular, the difference in $\mu_{C_D}$ between two models decreased from 23 to 2 drag counts for the VBW case. Among all cases, the MBW case with SST model requires the minimum number of iterations to converge. The computational cost stays constant with both turbulence models for the MBW and VBW cases. Unlikely, the number of iterations to converge is 19 and 24 for the EW case with SA and SST models, respectively. It should be noted that the computational time per iteration for each case is approximately the same since the sensitivities are obtained from an adjoint solution.

The original and optimized shapes for the MBW case with SA and SST models can be seen in Figure 7.6. There is a significant difference between the original and optimal CRM wing shapes, however the optimized shapes with different turbulence models are very similar at stations A-F. The difference between the original and optimal shapes increases from the root (station A) to the tip (station H) of the wing. The upper and lower surfaces of

Table 7.2. The robust design cases with different weight contributions to the objective function.

| Optimization Case | $W_1$ | $W_2$ | $W_3$ |
|---|---|---|---|
| Mean-biased weighting (MBW) | 0.360 | 0.323 | 0.317 |
| Equal weighting (EW) | 0.333 | 0.333 | 0.334 |
| Variance-biased weighting (VBW) | 0.3 | 0.4 | 0.3 |

Table 7.3. Robust optimization results for the wing obtained at $\mu_{C_L} = 0.65$ with the SA and SST models.

| Optimization Case | $\mu_{C_D}$ | $\sigma_{C_D} \times 10^3$ | $\Delta\mu_{C_D}$ (cts) | $\Delta\sigma_{C_D}$ (cts) | # of Iterations | $\alpha$ (°) |
|---|---|---|---|---|---|---|
| Original (SA) | 0.0356 | 4.06 | - | - | - | 3.56 |
| Original (SST) | 0.0379 | 3.61 | - | - | - | 3.81 |
| MBW (SA) | 0.0320 | 2.74 | 36 | 14 | 17 | 3.58 |
| MBW (SST) | 0.0328 | 2.26 | 51 | 13 | 16 | 3.82 |
| EW (SA) | 0.0328 | 2.38 | 28 | 17 | 19 | 3.59 |
| EW (SST) | 0.0335 | 1.65 | 44 | 20 | 24 | 3.83 |
| VBW (SA) | 0.0331 | 1.99 | 25 | 21 | 22 | 3.59 |
| VBW (SST) | 0.0333 | 1.38 | 46 | 22 | 22 | 3.83 |

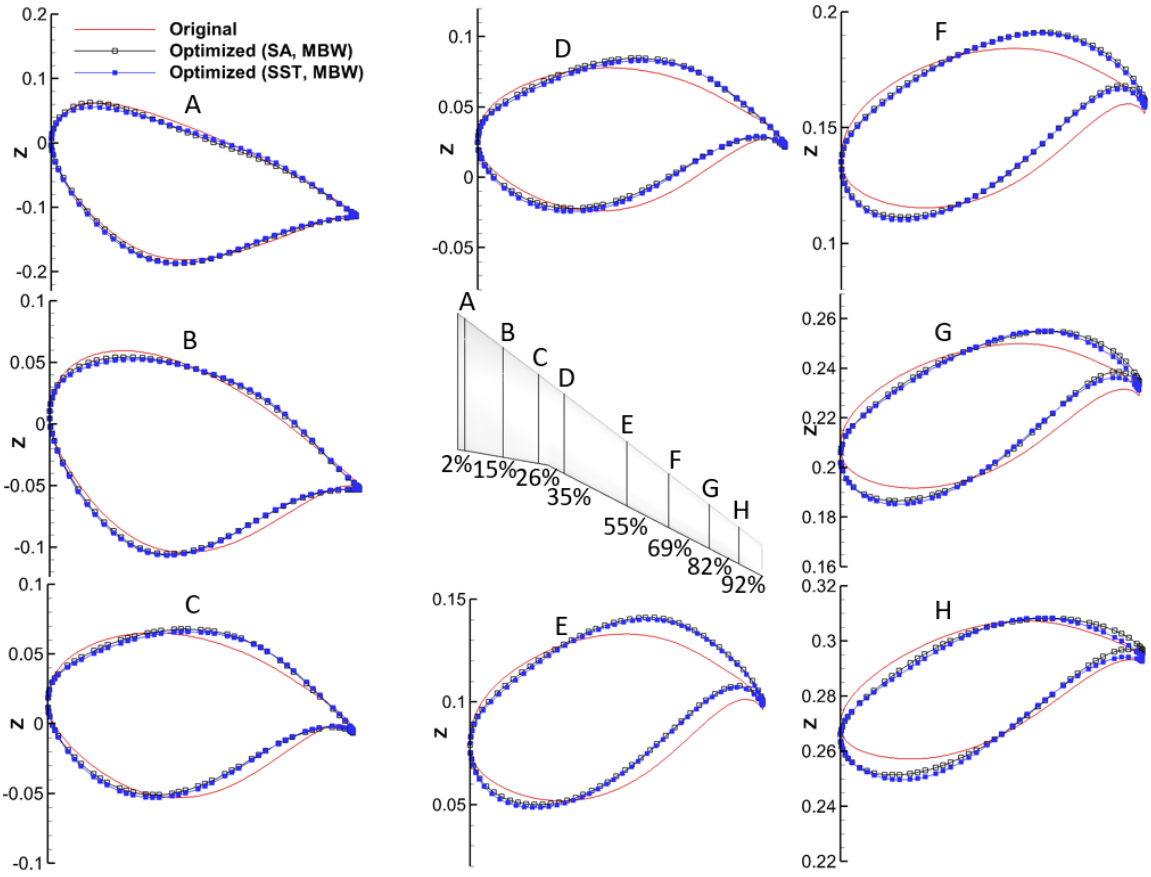


Figure 7.6. The comparison of original and optimal shapes at different spanwise stations for the MBW case with SA and SST models.

the optimal shapes nearby the trailing edge with different turbulence model show slightly different trend at stations G and H. The slight difference in the lower surface of the optimal shapes nearby the leading edge with different turbulence model can also be observed at the same stations.

Figure 7.7 presents the $C_p$ distributions of the original and optimized shapes at selected spanwise stations for the MBW case with SA and SST models at a $C_L$ of the 0.65 at $M_{nominal}$ corresponding to the mean of the Mach number interval considered. The pressure distributions obtained with different turbulence models are close to each other at

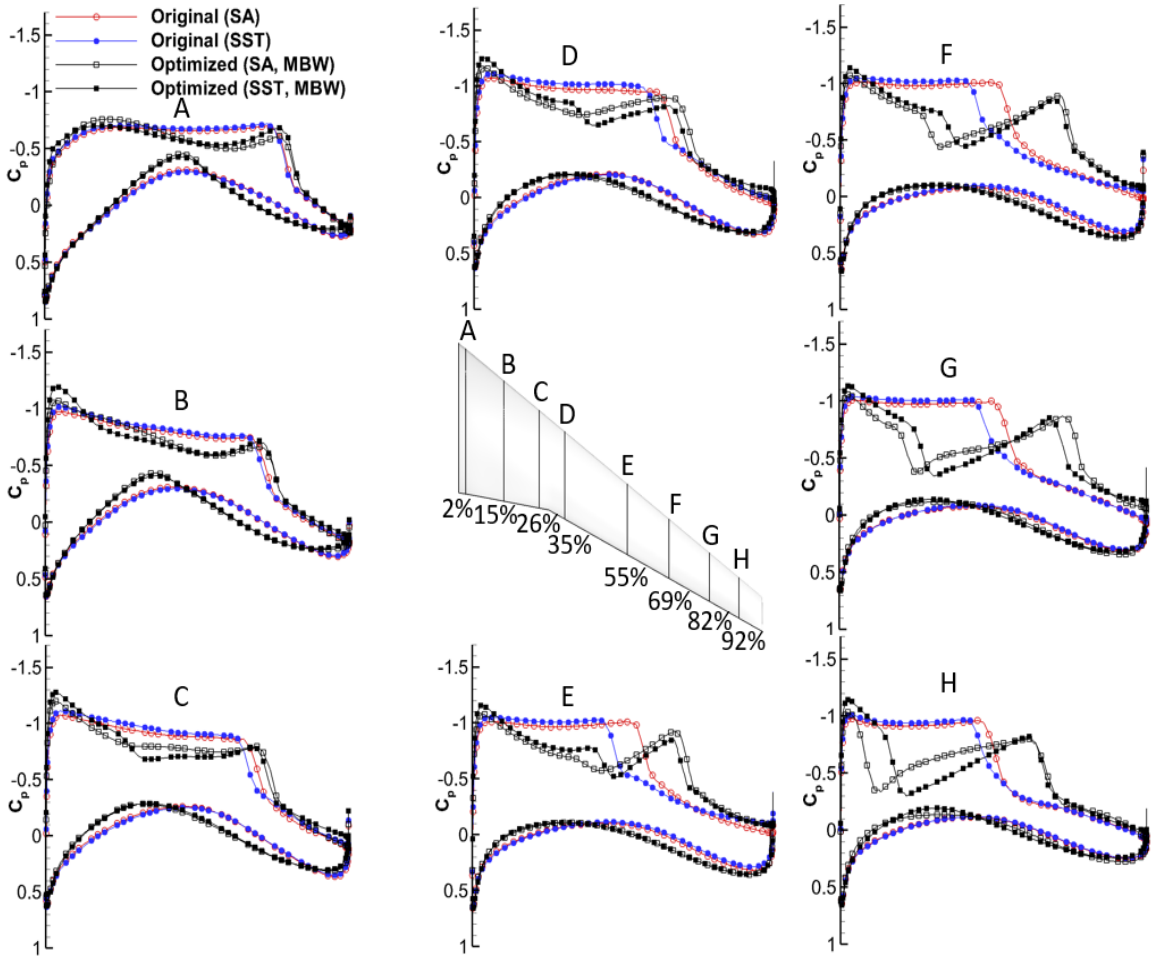


Figure 7.7. The comparison of $C_p$ distributions for the original and optimum shapes at selected spanwise stations for the MBW case with SA and SST models at $C_L$ = 0.65 at $M_{nominal}$.

stations A-F. The difference between the optimum shape pressure distributions can be seen on the upper and lower surfaces at stations G and H where the shapes are different. The difference due to the selection of turbulence model is reduced significantly at stations B-F. Two weaker shock waves are observed at stations F-H. The strength of the shock wave is reduced at stations D and E with SST model.

Figure 7.8 presents the $C_p$ distributions of the original and optimized shapes at selected spanwise stations for the MBW case with SA and SST models at a $C_L$ of the 0.65 at $M_{max}$ corresponding to the maximum of the Mach number interval considered. The

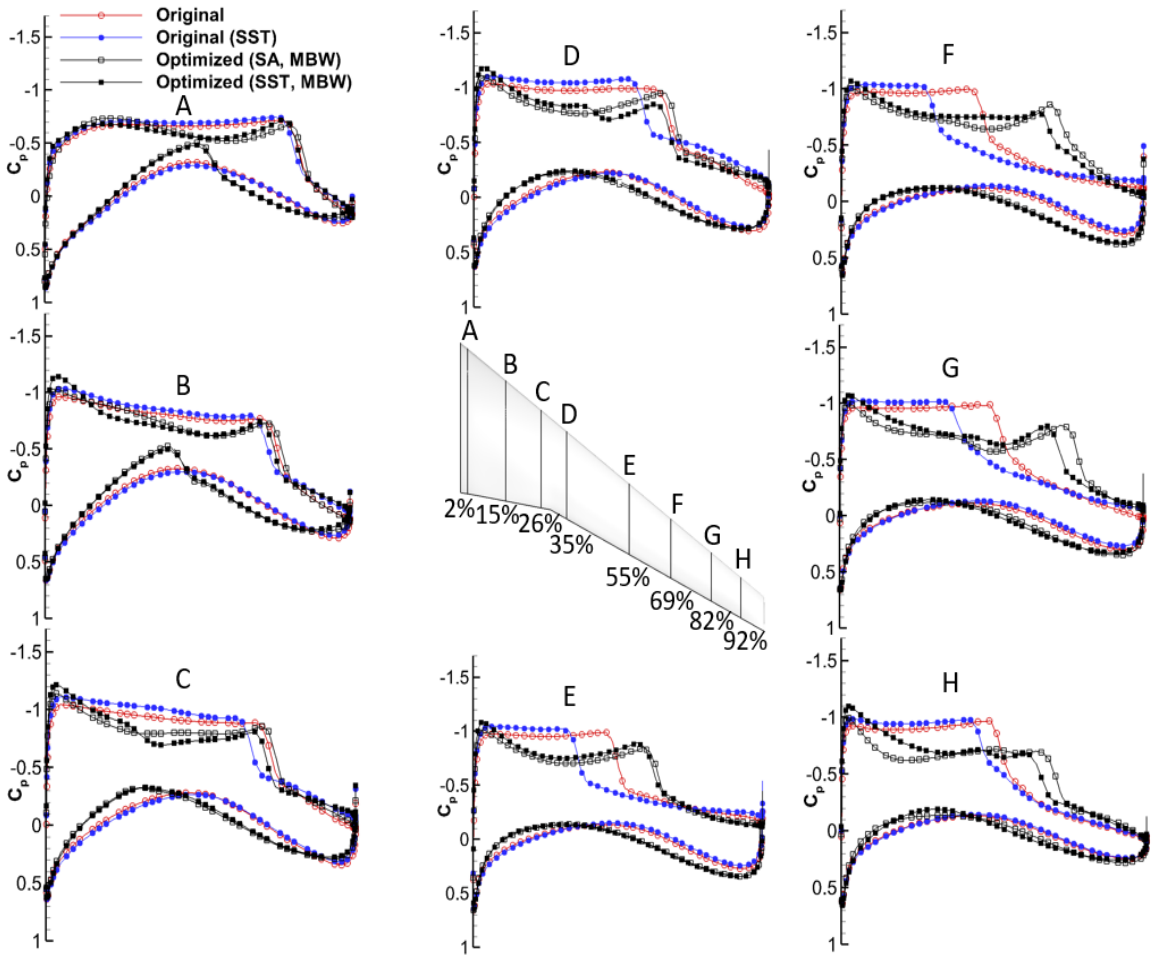


Figure 7.8. The comparison of $C_p$ distributions for the original and optimum shapes at selected spanwise stations for the MBW case with SA and SST models at $C_L$ = 0.65 at $M_{max}$.

pressure distributions obtained with different turbulence models are close to each other at each station. The difference due to the selection of turbulence model is reduced significantly at stations C-G. In particular, the same $C_p$ distribution is observed at station E with SA and SST models. The strength of the shock wave is reduced significantly at stations E, F and H. The reduction in shock wave strength was more at $M_{max}$ compared to the reduction at $M_{nominal}$.

Figure 7.9 presents the original and optimized shapes at selected spanwise stations for the EW case with both turbulence models. As observed for the MBW case, the different turbulence models provide similar optimized shapes at each station except stations G and H.

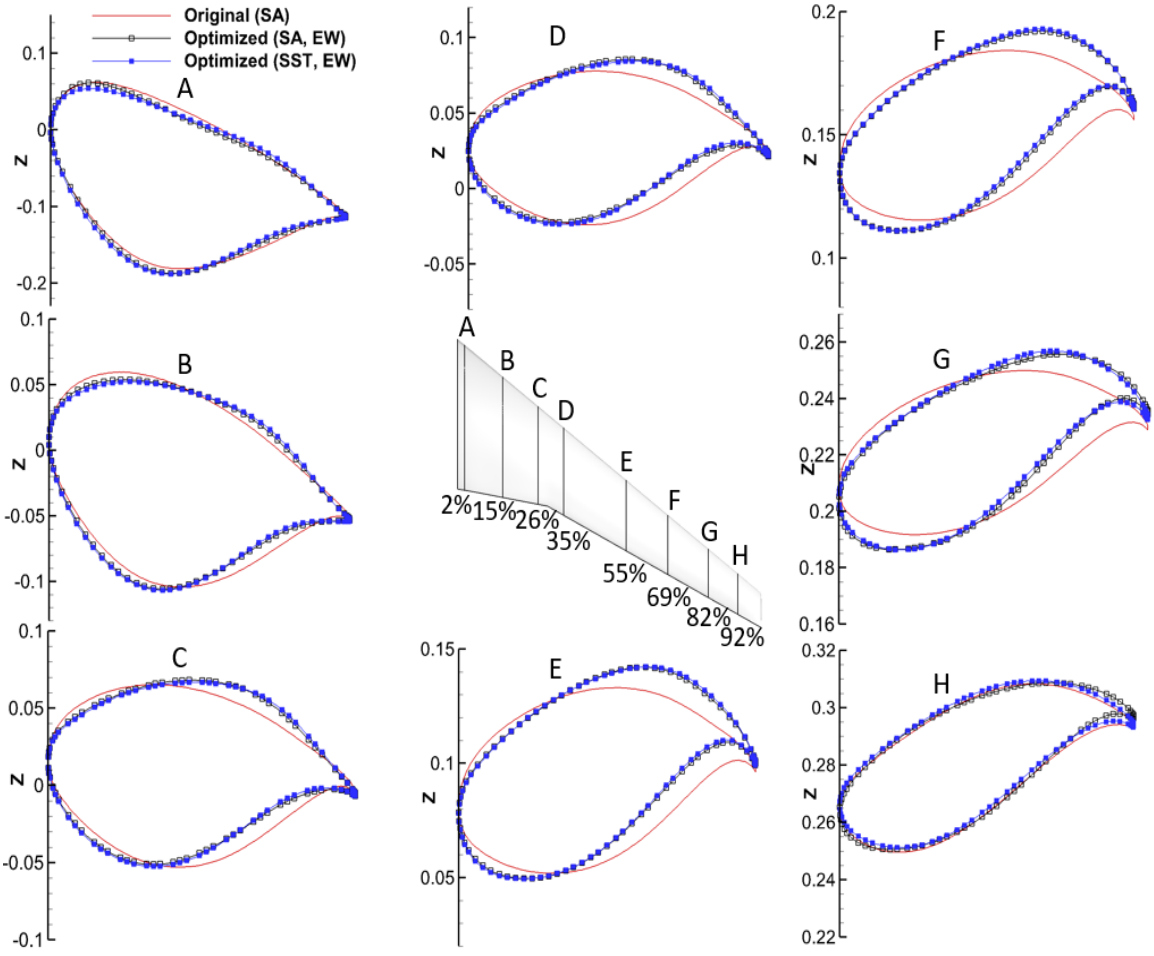


Figure 7.9. The comparison of original and optimal shapes at selected spanwise locations for the EW case with SA and SST models.

There is a significant difference between the original and optimized shapes at each station, and this difference increases from station A to H along the spanwise direction. Similar to the MBW case, the difference between the optimum shapes can be observed at the upper and lower surfaces in the vicinity of leading and trailing edge at stations G and H.

Figure 7.10 shows the $C_p$ distributions of the original and optimized shapes at selected spanwise locations for the EW case with two turbulence model at $M_{nominal}$ at the $C_L$ of 0.65. The difference due to the selection of the turbulence model is reduced significantly at stations B-F. The difference in the pressure distribution between optimum

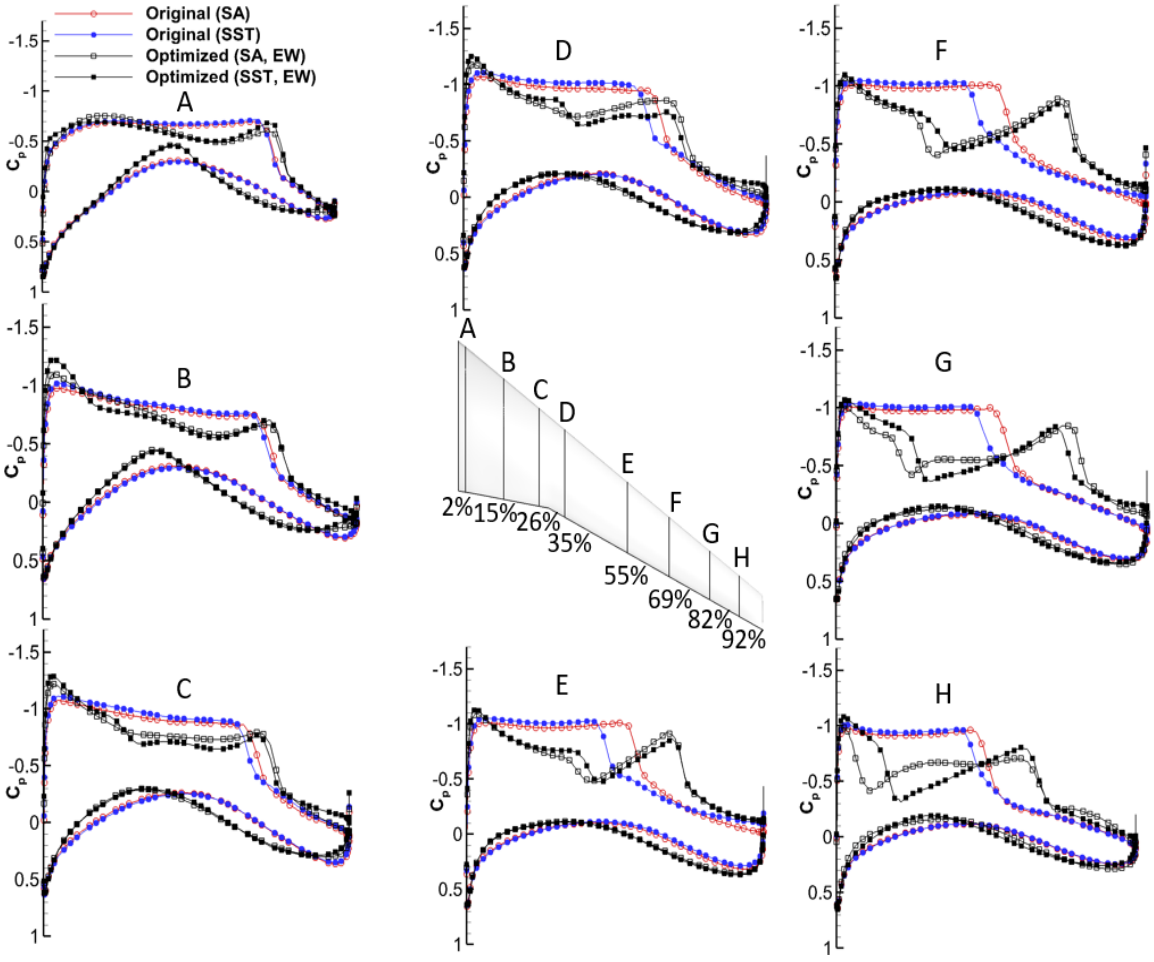


Figure 7.10. The comparison of $C_p$ distributions for the original and optimum shapes at selected spanwise locations for the EW case with SA and SST models at $C_L$ = 0.65 at $M_{nominal}$.

shapes can be observed on the upper and lower surfaces at stations G and H where the difference in the wing profile shapes is observed. Two weaker shock waves are observed at stations F-H. The strength of shock wave is reduced significantly at station D with SST model.

Figure 7.11 presents the $C_p$ distributions of the original and optimized shapes at selected spanwise stations for the EW case with two turbulence model at $M_{max}$ at a $C_L$ of 0.65. The difference in pressure distribution between the optimum shapes is very small at each station. Similar to the MBW case, the $C_p$ distribution with SA and SST models are the same at station E. The shock wave is weakened at stations E, F and H. The difference in $C_p$

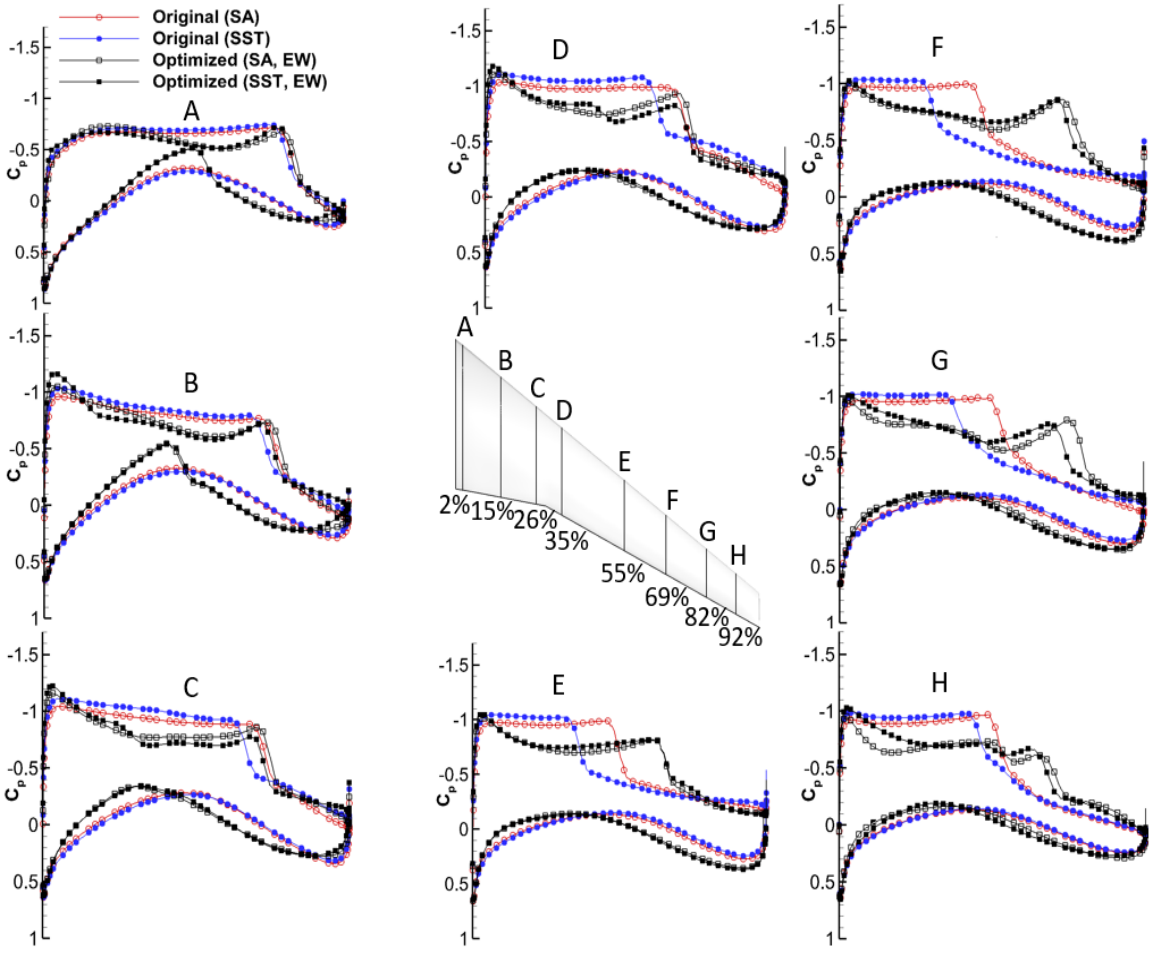


Figure 7.11. The comparison of $C_p$ distributions for the original and optimum shapes at selected spanwise stations for the EW case with SA and SST models at $C_L = 0.65$ at $M_{max}$.

distributions due to the selection of the turbulence model and the strength of shock wave are reduced more at $M_{max}$ compared to the reductions observed at $M_{nominal}$ for the EW case.

The original and optimal shapes at selected spanwise stations for the VBW case with each turbulence model can be seen in Figure 7.12. The significant difference between the original and optimal shapes is shown at each station. Similar to the other cases the optimum shapes are very close to each other at each station except the locations G and H. The difference between the optimum shapes can be seen on both upper and lower surfaces nearby the leading and trailing edges.

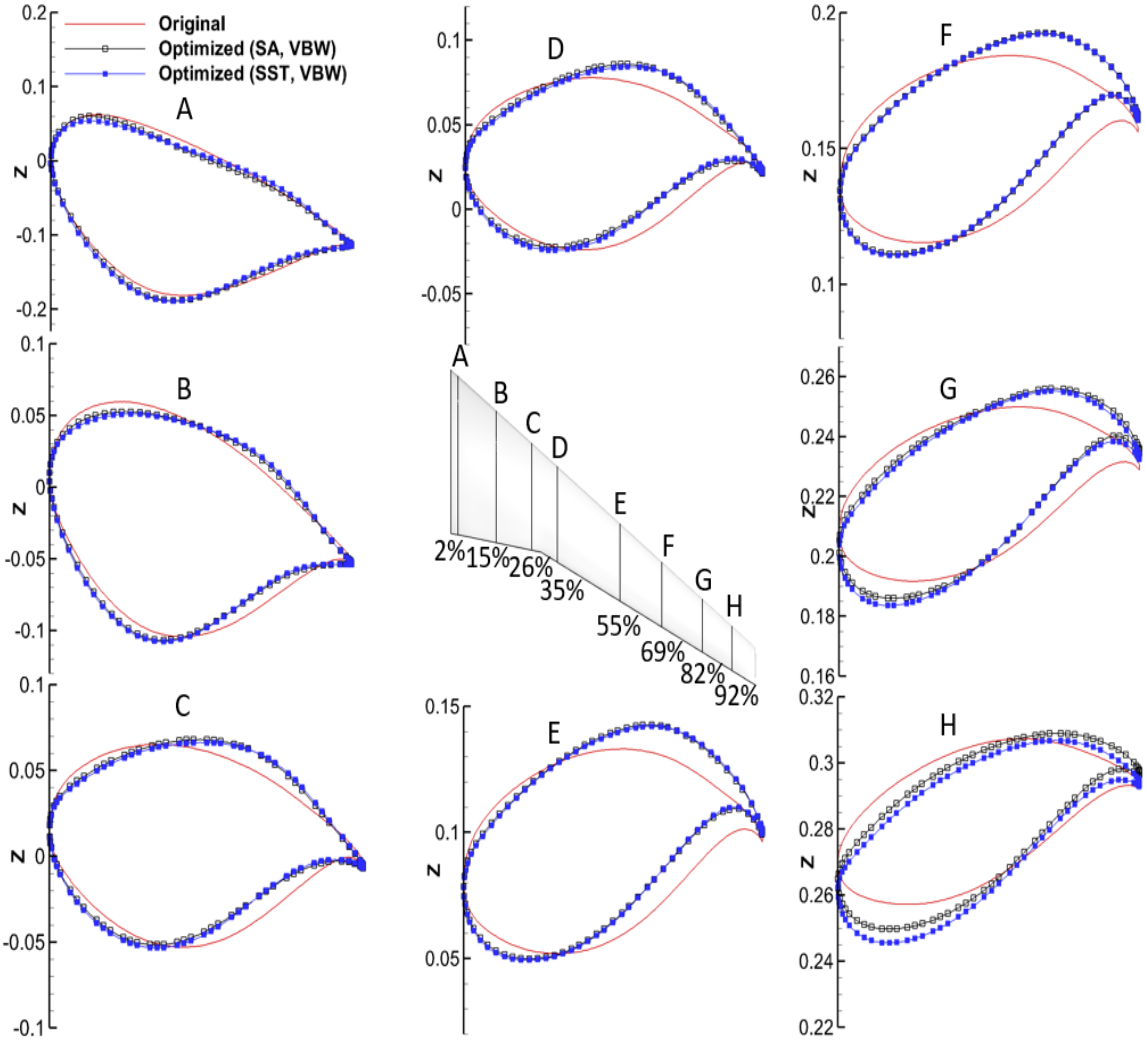


Figure 7.12. The comparison of original and optimal shapes at selected spanwise stations for the VBW case with SA and SST models.

Figure 7.13 represents the pressure distribution of the original and optimal shapes at selected spanwise stations for the VBW case with each turbulence model at a $C_L$ of 0.65 at $M_{nominal}$. The $C_p$ distribution of the optimum shapes are close to each other at each station. In particular, the difference in $C_p$ distributions between the two turbulence models decreased significantly at stations E-G. The reduction in the strength of shock wave can be seen at stations D and H. Similar to the other cases (MBW and EW), two weaker shock waves are observed at stations E-G.

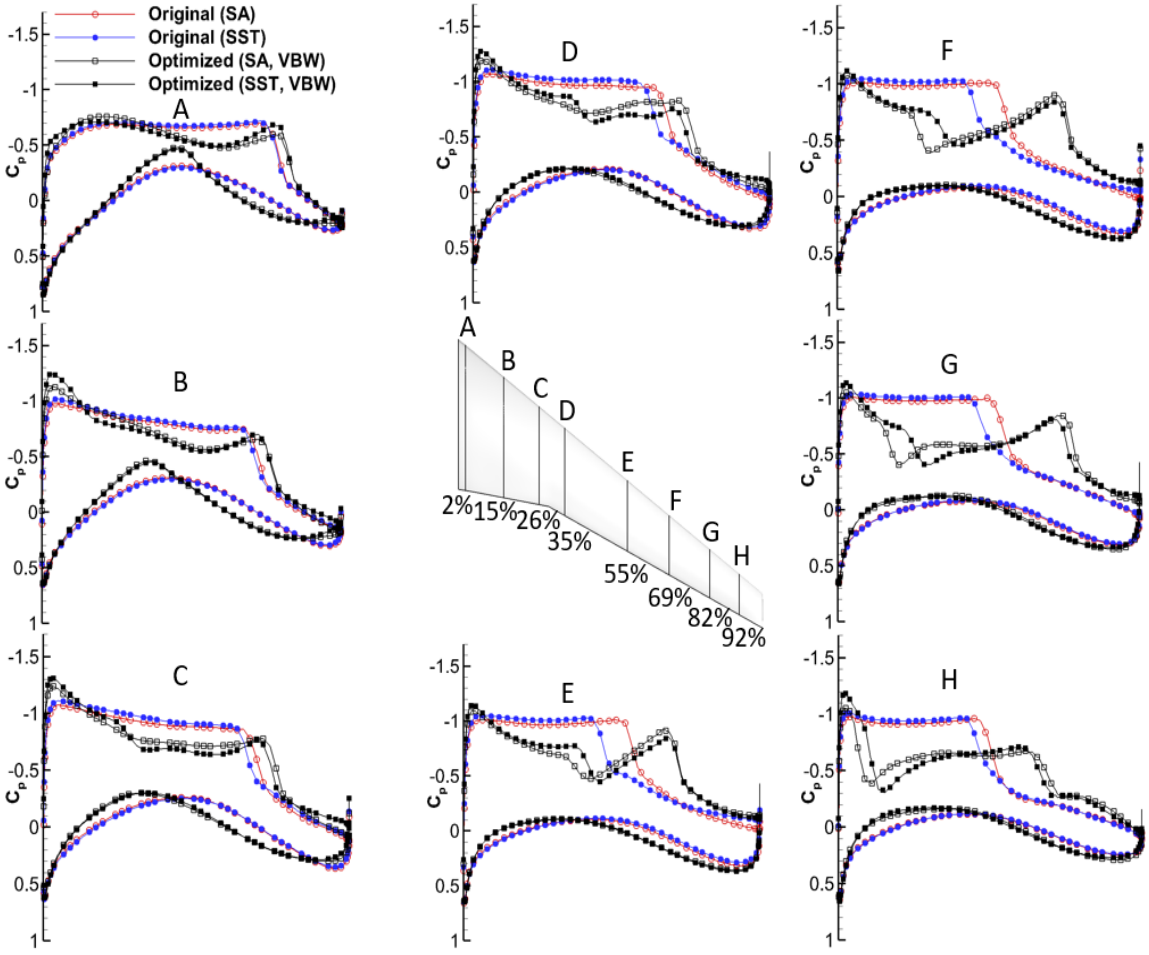


Figure 7.13. The comparison of $C_p$ distributions for the original and optimum shapes at selected spanwise stations for the VBW case with SA and SST models at $C_L$ = 0.65 at $M_{nominal}$.

The pressure distribution of the original and optimal shapes at selected spanwise stations for the VBW case with each turbulence model at a $C_L$ of 0.65 at $M_{max}$ is presented in Figure 7.14. The difference in $C_p$ distributions due to the selection of the turbulence model is reduced remarkably at each station, in particular for locations E-G. The reduction in the shock wave strength is observed at stations E-G. Similarly to the previous cases (MBW and EW), more reduction in the shock strength is observed at $M_{max}$ compared to the reductions observed for $M_{nominal}$.

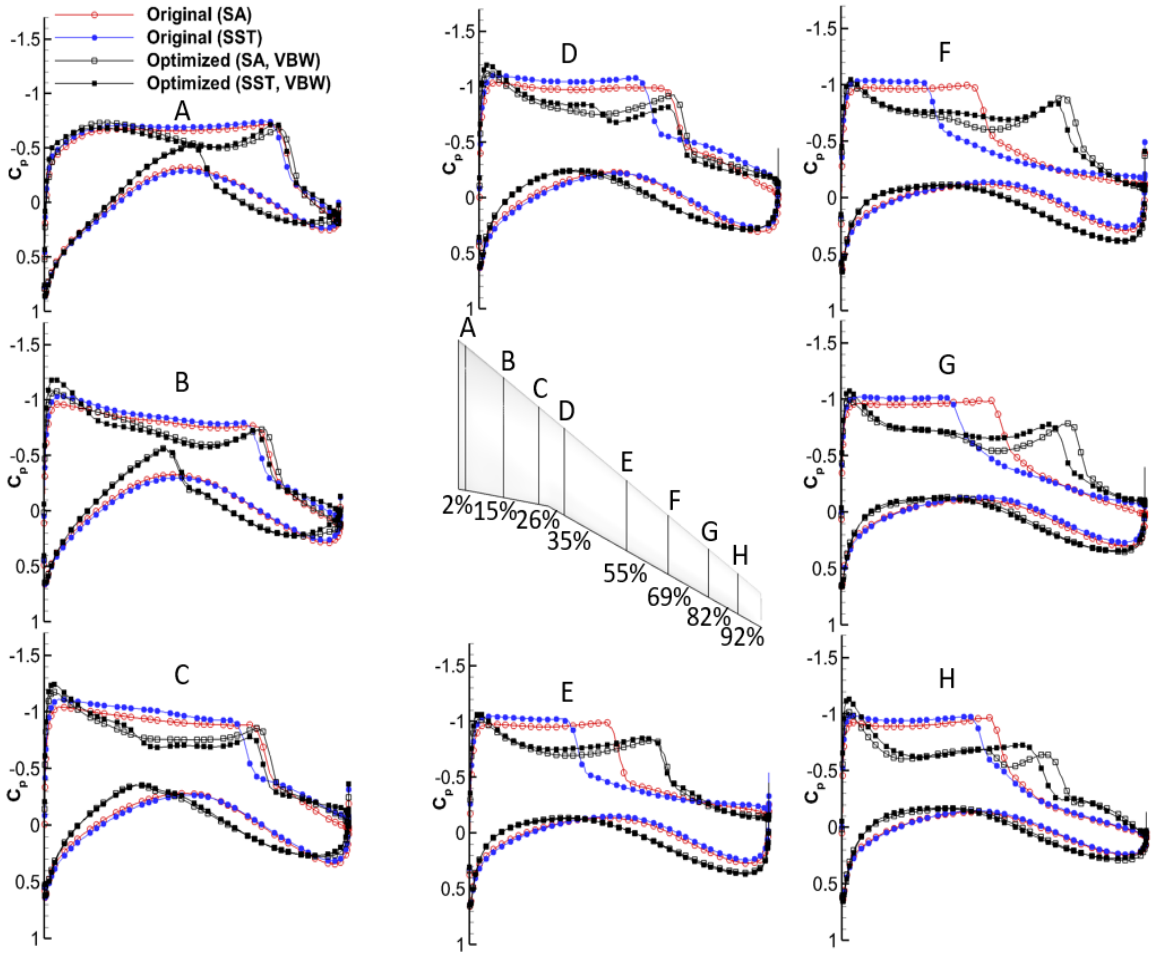


Figure 7.14. The comparison of $C_p$ distributions for the original and optimum shapes at selected spanwise stations for the VBW case with SA and SST models at $C_L$ = 0.65 at $M_{max}$.

The comparison of the original and optimal shapes at selected spanwise stations for the VBW, MBW and EW cases with SA model is presented in Figure 7.15. There is a remarkable difference between the original and optimum shapes at each spanwise. The difference between the original and optimum shapes increases from root to the tip of the CRM wing. The optimum shapes for the MBW case provides slightly different trend on the upper and lower surface nearby the trailing edge compared to the other two optimum shapes at stations E-G. At station H, the optimum shapes for the VBW and EW cases are observed to be similar, however the optimum shape for the MBW case shows a different trend for both upper and lower surfaces.

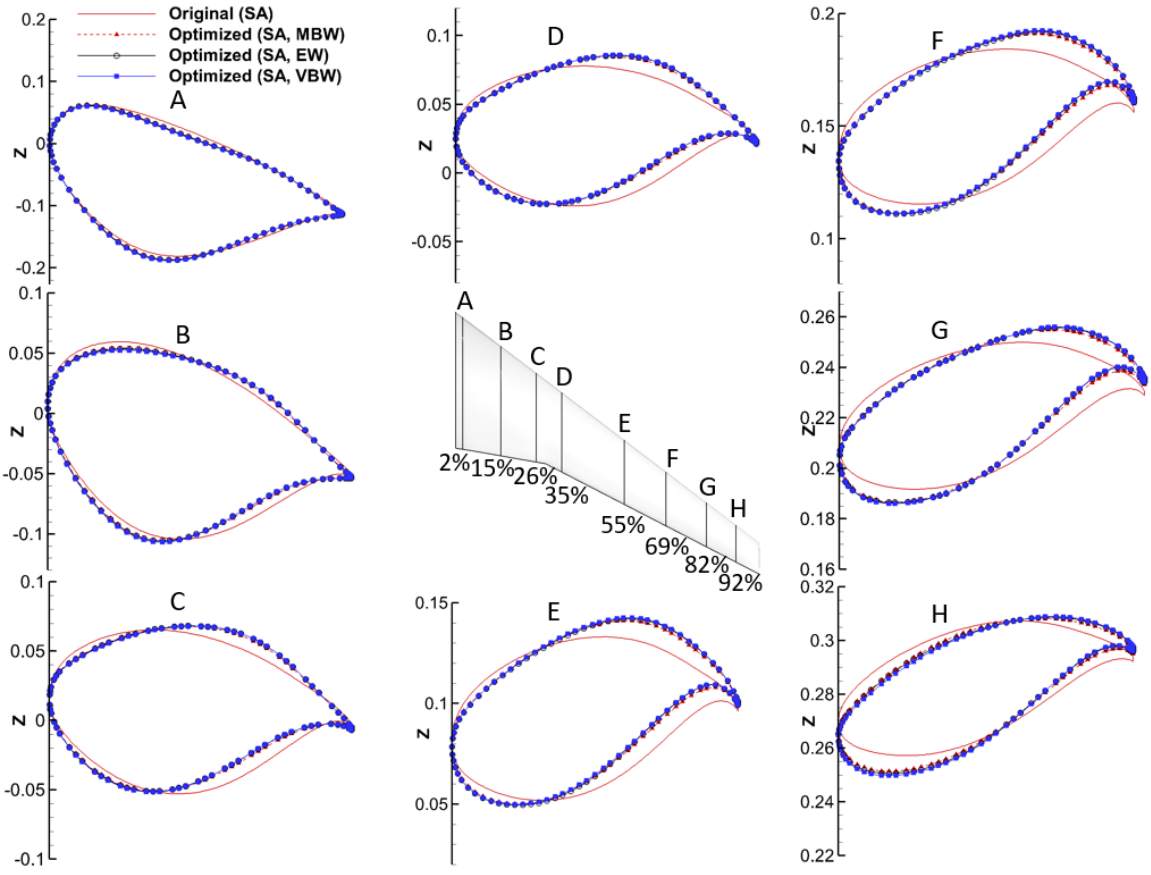


Figure 7.15. The comparison of original and optimal shapes at selected spanwise stations for the MBW, VBW and EW cases with SA model.

Figure 7.16 presents the $C_p$ distribution of original and optimum shapes at selected spanwise stations for the MBW, VBW and EW cases with SA model at a $C_L$ of 0.65 at $M_{nominal}$. The pressure distributions of optimum shapes for all cases are similar at stations A and B. The $C_p$ distribution of the optimum shape for the MBW case is slightly different compared to the $C_p$ distribution for the other cases at stations C-F. The $C_p$ distribution of optimal shapes on upper surface is different for each case at stations G and H. The single strong shock wave observed over the original wing shape is replaced with two weaker shock waves over the optimum shape at stations E-H.

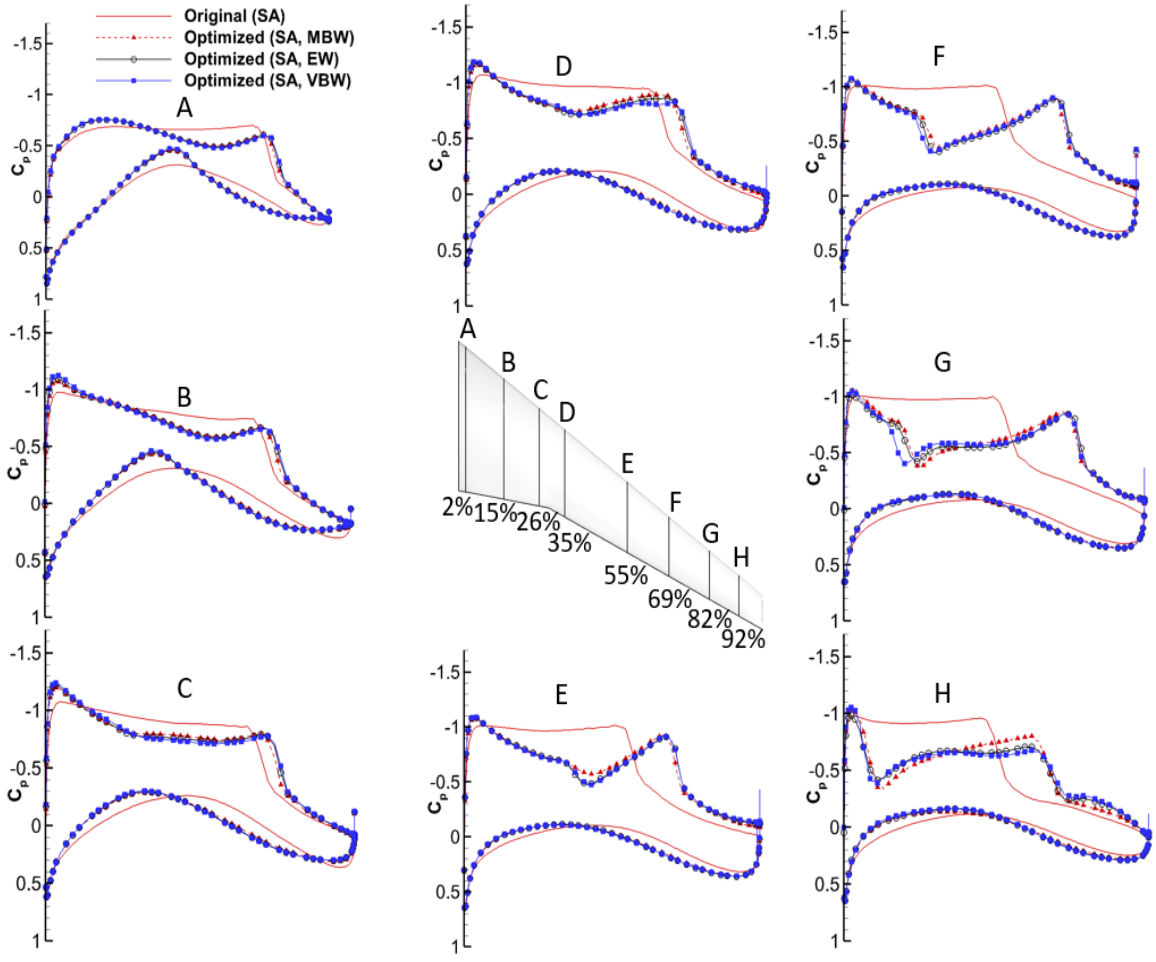


Figure 7.16. The comparison of $C_p$ distributions for the original and optimum shapes at selected spanwise stations for the MBW, VBW and EW cases with SA model at $C_L$ = 0.65 at $M_{nominal}$.

Figure 7.17 presents the $C_p$ distribution of the original and optimum shapes at selected spanwise stations for the MBW, VBW and EW cases with SA model at a $C_L$ of 0.65 at $M_{max}$. The pressure distribution of optimum shapes are similar at stations A and B, however the difference in the $C_p$ distribution of optimum shapes among all cases can be seen at stations G and H where the optimum shapes are different. The $C_p$ distribution of optimum shape for the MBW case shows different trend compared to the other cases at stations C-F. The reduction in shock strength is noticeable at stations E and H for all cases. At $M_{max}$, there is less difference in pressure distributions due to the selection of the turbulence model compared to the difference at $M_{nominal}$. The shock strength is also reduced more at $M_{max}$.

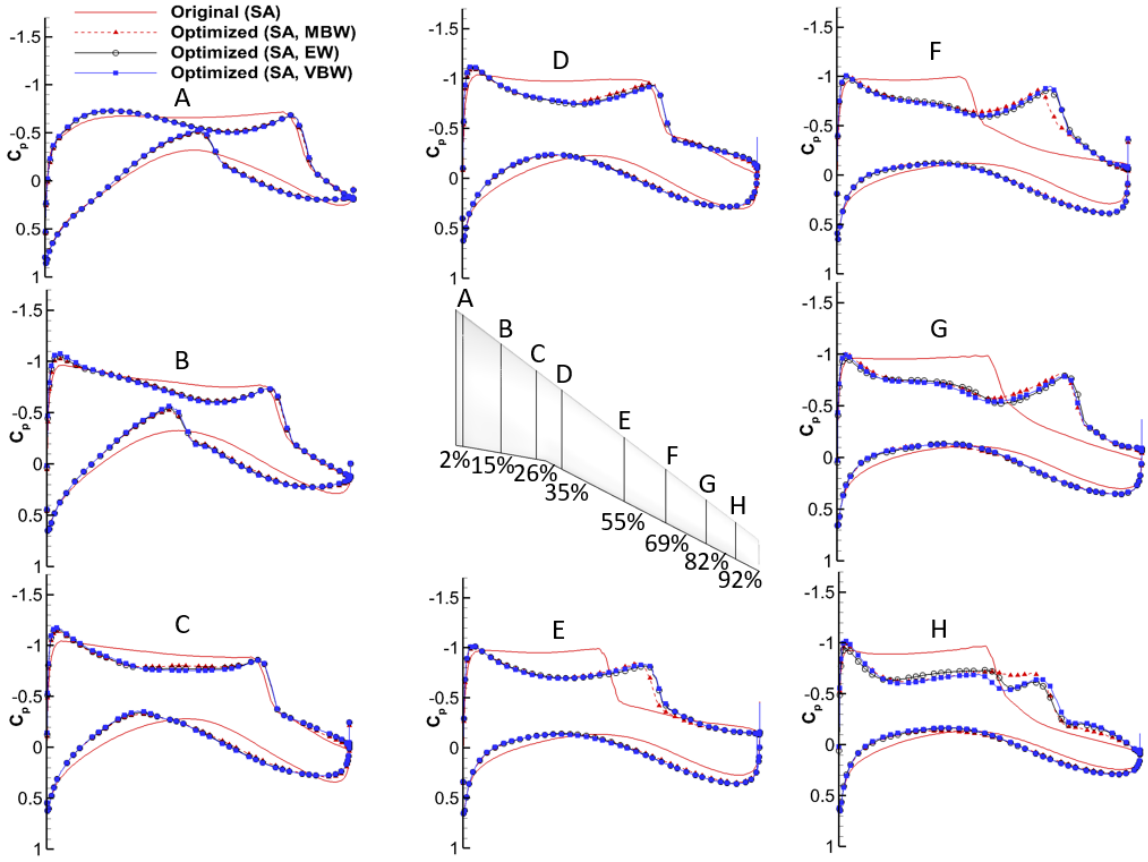


Figure 7.17. The comparison of $C_p$ distributions for the original and optimum shapes at selected spanwise stations for the MBW, VBW and EW cases with SA model at $M_{max}$ at $C_L = 0.65$.

The comparison of original and optimized shapes at selected spanwise stations for the MBW, VBW and EW cases with SST model is presented in Figure 7.18. Similar to SA model, the difference between the original and optimal shapes is remarkable for all cases at each station. The optimal shapes are similar at stations A and B, however the noticeable difference between the optimal shapes can be observed at stations G and H. The optimal shapes for the MBW case exhibits a different trend on the upper and lower surfaces nearby the trailing edge compared to the other optimum shapes. The difference between the original and optimum shapes increase from root to tip of the wing.

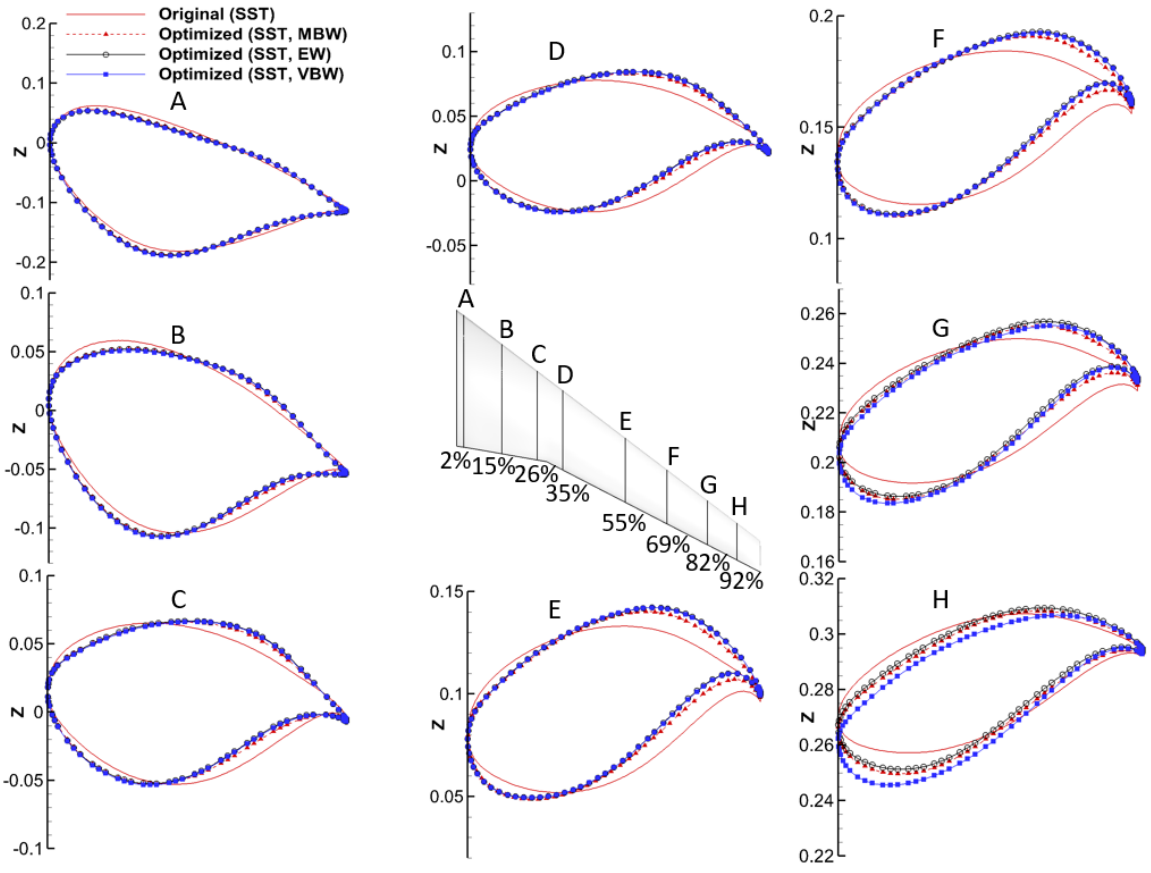


Figure 7.18. The comparison of original and optimal shapes at selected spanwise stations for the MBW, VBW and EW cases with SST model.

Figure 7.19 shows the pressure distribution of the original and optimized shapes at selected spanwise stations for the MBW, VBW and EW cases with SST model at a $C_L$ of 0.65 at $M_{nominal}$. The pressure distributions of optimum shape for VBW and EW cases present similar trend at stations A-F, however the $C_p$ distributions of the optimum shape obtained with MBW case are slightly different at the same stations. At stations G and H, the $C_p$ distributions of the optimum shapes with MBW and EW cases are fairly different compared to the $C_p$ distribution of the optimum shape for the VBW case. The strength of shock wave is reduced significantly at station D, and the single shock of the original geometry is replaced with two weaker shocks over the optimum shape at stations E-H.

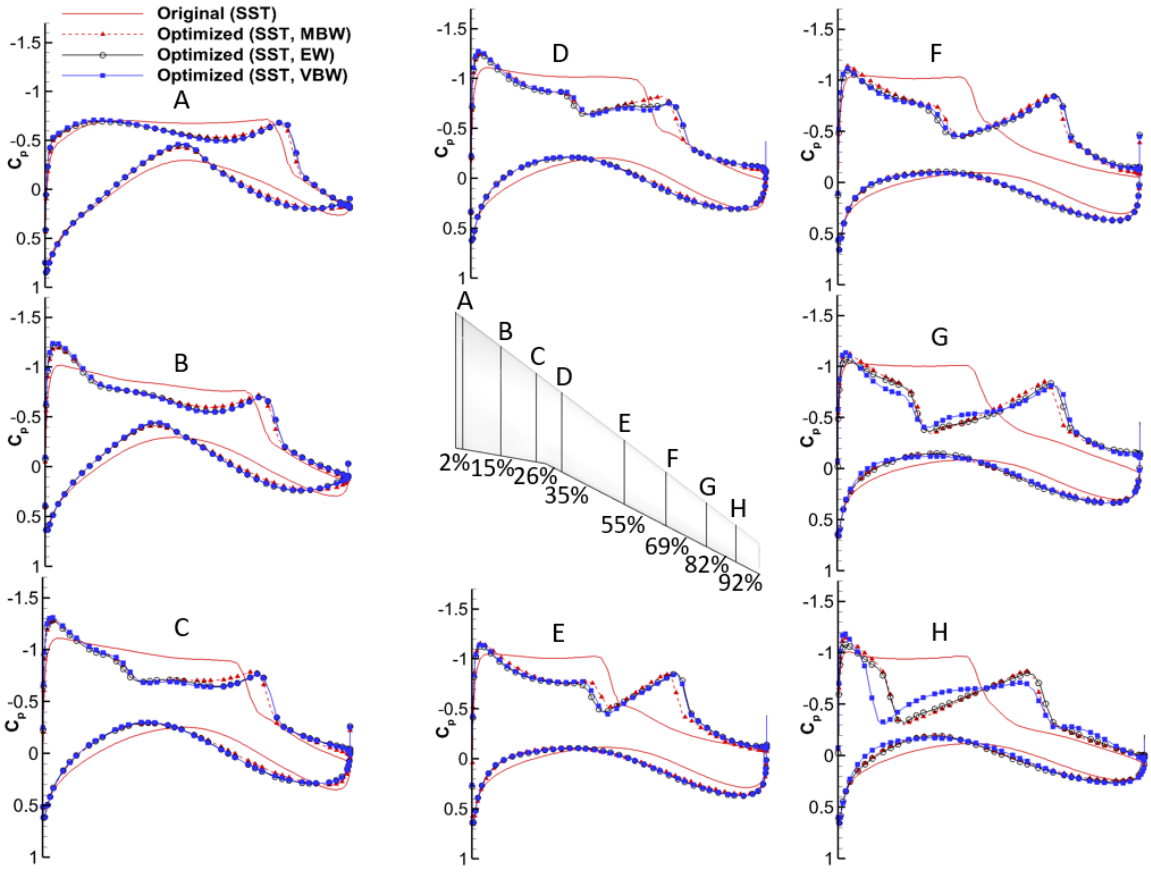


Figure 7.19. The comparison of $C_p$ distributions for the original and optimum shapes at selected spanwise stations for the MBW, VBW and EW cases with SST model at $C_L$ = 0.65 at $M_{nominal}$.

The $C_p$ distributions of the original and optimal shapes at selected spanwise stations for the MBW, VBW and EW cases with SST model at a $C_L$ of 0.65 at $M_{max}$ is presented in Figure 7.20. The $C_p$ distribution of the optimum shapes for VBW and EW cases follow a similar trend compared to the optimum shapes for the MBW case at stations A-F, however the $C_p$ distribution of optimum shape for the EW and MBW cases is similar compared to the optimal shape for the VBW case at stations G and H. The strength of the shock wave is reduced remarkably at stations F-H.

Overall, the detailed shape and pressure distribution analysis performed in this section indicate that the impact of the selection of turbulence models on the aerodynamic characteristics (i.e., the pressure distribution) of the wing is reduced remarkably with

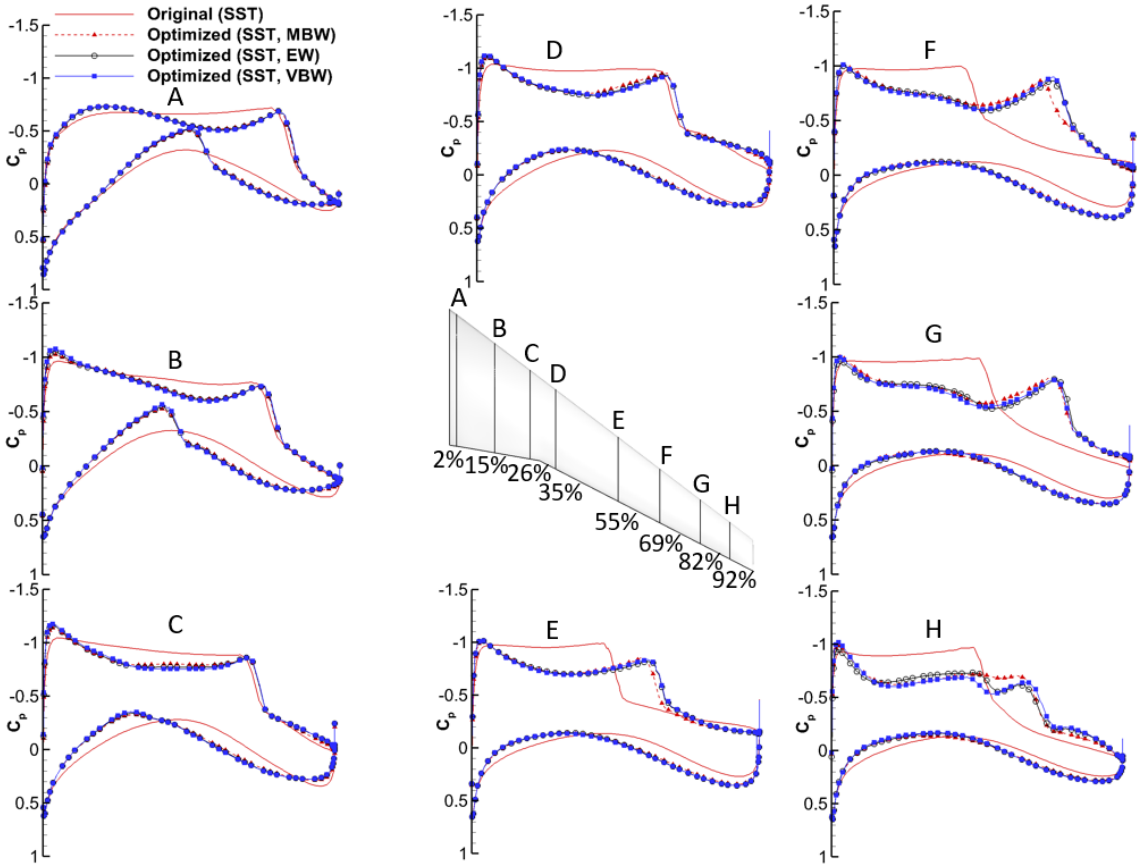


Figure 7.20. The comparison of $C_p$ distributions for the original and optimum shapes at selected spanwise stations for the MBW, VBW and EW cases with SST model at $C_L$ = 0.65 at $M_{max}$.

robust optimization over the Mach number range considered. This is consistent with the observations made for the 2-D robust optimization results. Also, the weights used in the objective function has a larger effect on the optimal shape and the associated aerodynamic characteristics of the optimized wing geometry than the effect of turbulence model in the robust optimization.

## 7.4. COMPARISON BETWEEN ROBUST AND DETERMINISTIC OPTIMIZATION

In deterministic optimization, the wing shape is optimized to minimize the drag coefficient at a target $C_L$ for a certain Mach number with the angle of attack defined as a design variable, However, the performance of optimized shape noticeably degrade if the Mach number changes from its design point in transonic flow. The objective of robust aerodynamic design is to minimize the mean ($\mu_{C_D}$) and variance ($\sigma_{C_D}$) of the drag coefficient at a target mean lift coefficient ($\mu_{C_{L_{\text{Target}}}}$) to achieve robustness in the performance over the specified range. The number of iterations required to converge is greater with the robust design than the deterministic design for VBW case with both turbulence models and for the EW case with SST model (see Table 7.1 and 7.3). Similar to the 2D study, the number of total CFD evaluations is equal to the total number of iterations to converge in deterministic design, whereas the number of total CFD evaluations in $N_s$ times the number of iterations required to converge in robust optimization. The computational cost of robust design per optimization iteration is six times higher than the computational cost of deterministic optimization. In this section, the difference between the performance of the robust and deterministic designs are investigated over the uncertain Mach number range. The effect of the turbulence model is also demonstrated.

The variation of the drag coefficient of the original shape, deterministic design and robust design with the Mach number are presented in Figure 7.21 for each test case for the SST model. The drag coefficient of each shape are evaluated at the target $C_L$ of 0.65. The

$C_D$ of the original CRM wing is the highest over the entire Mach number range except the minimum Mach number. At $M = 0.85$, which is the deterministic design point, the $C_D$ of the deterministic design is approximately 69 drag counts. There is a slight drop in $C_D$ until the deterministic design Mach number and then a significant increase occurs as the Mach number increases. This trend clearly shows that the deterministic optimization performs relatively poorly at the off-design Mach numbers. On the other hand, the wing obtained with the robust optimization approach exhibits a relatively flat $C_D$ curve over the Mach number range with a slight increase starting from $M = 0.865$. The shape obtained with robust optimization achieves 43 drag counts for the MBW case, 46 drag counts for the EW case, and 52 drag counts for the VBW case compared to deterministic design at $M_{max} = 0.872$. The shape obtained with robust optimization for the MBW case performs better than the other two robust designs until the deterministic design Mach number, however its increment in $C_D$ is larger than the other two robust designs after the nominal Mach number. The robust design obtained with VBW case improves the robustness more than the other two robust designs. Overall, robust design performs better than the deterministic design in terms of robustness and the mean performance over the Mach number range considered.

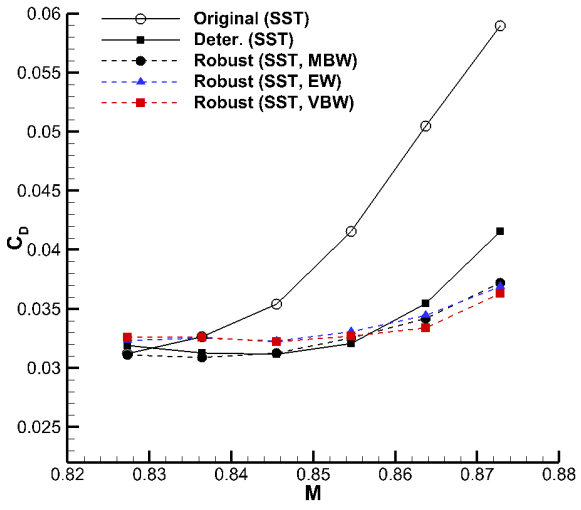


Figure 7.21. $C_D$ comparison of original and optimum shapes (deterministic and robust) with SST under varying Mach number at $C_L = 0.65$ (The MBW, VBW, EW cases).

In Figure 7.22, the variation of the drag coefficient of the original, deterministic design, and robust design with the Mach number are presented for each test case for the SA model. The drag coefficient values of each shape are evaluated at the target $C_L$ value of 0.65. The $C_D$ of deterministic design decreases until $M = 0.85$ and then increases dramatically. The robust design, the VBW case in particular, provides relatively flat $C_D$ curve unlike the deterministic design over the Mach number range. At $M_{max} = 0.872$, the shape obtained with robust optimization achieves 28 drag counts for the EW case, 30 drag counts for the MBW case, and 31 drag counts for the VBW case compared to deterministic design. The robust design with the MBW case provides better mean performance compared to the other two robust designs. Similar to the SST model, robust design has better performance than deterministic design in terms of robustness over the defined Mach number range.

From Figure 7.23, it can be seen that the robust design obtained with VBW case with SST model gives the best result in terms of the mean performance and robustness obtained over the Mach number range that is considered for both turbulence models. It is also observed that the robust design tends to reduce the impact of the turbulence model selection on the optimum shape and performance, because the turbulence model becomes important

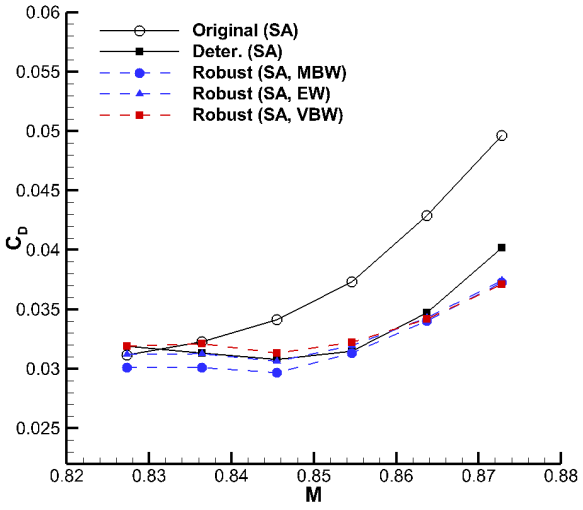


Figure 7.22. $C_D$ comparison of original and optimum shapes (deterministic and robust) with SA under varying Mach number at $C_L = 0.65$ (The MBW, VBW, EW cases).

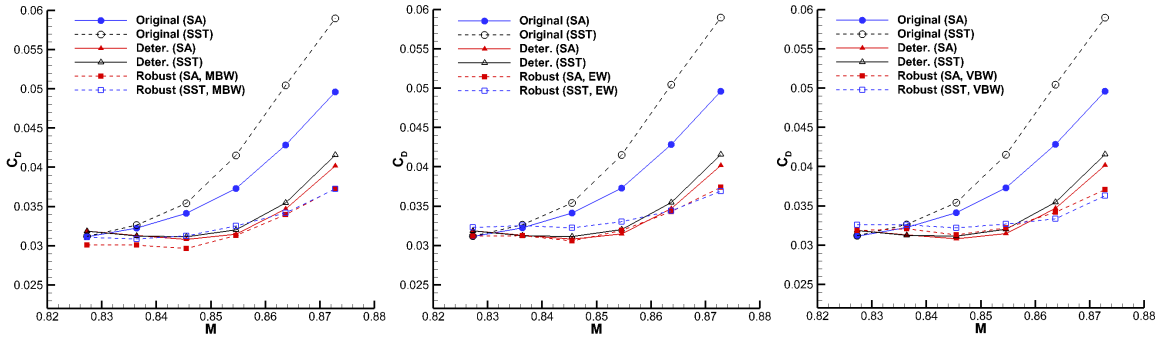


Figure 7.23. $C_D$ comparison of original and optimum shapes (deterministic and robust) under varying Mach number at $C_L$ = 0.65 MBW (left), EW (middle), VBW (right).

for the deterministic design at off-design conditions. The effect of weight contribution on the objective function on robust design is more significant than the effect of turbulence model.

The comparison of original and optimal shapes for both deterministic and robust optimization obtained with the VBW case with SST model, which is identified as the best approach for robust design, is presented in Figure 7.24. Optimized shapes obtained with robust and deterministic optimization are similar at station A. The optimal shapes for both designs are slightly different at stations G-H, which is sufficient enough for the robust design to provide better performance under varying Mach number as shown in Figure 7.21. Thickness constraints are satisfied with both designs.

In Figure 7.25, the comparison of $C_p$ distributions of the original and optimized shapes at $M_{nominal}$ is presented. The pressure distribution of optimal shapes for both designs show similar trend at stations A-C; however, the difference between the pressure distributions of two designs can be observed for the upper surface at stations D-H. The strength of the shock wave is significantly reduced over the deterministic design at stations D-F; however it is replaced with two weaker shocks over the robust design especially at stations E-H.

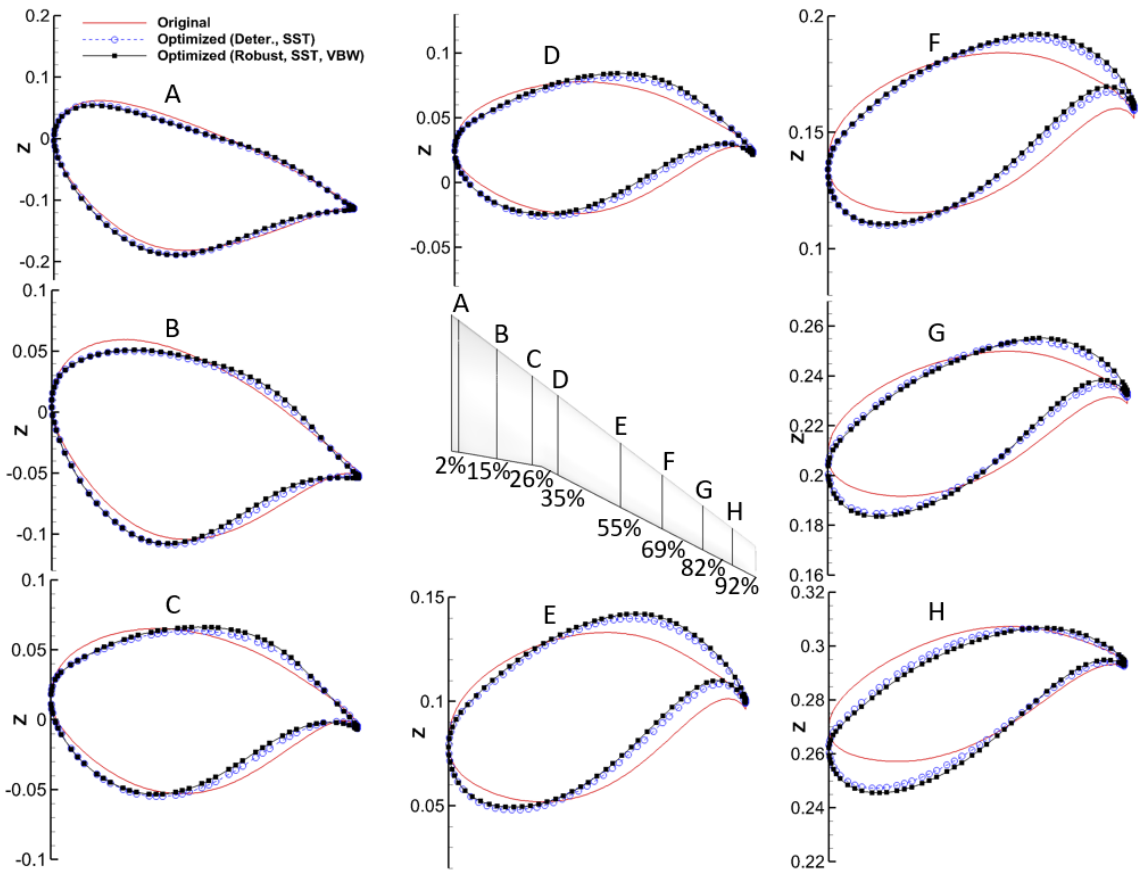


Figure 7.24. The comparison of original and optimized (robust and deterministic) shapes at selected spanwise stations.

In Figure 7.26, the comparison of $C_p$ distributions of the original and optimized shapes at $M_{max}$ is shown. Similar to the findings at $M_{nominal}$, the pressure distribution of optimal shapes for both designs show similar trend at stations A-C; however, the difference between the pressure distribution of two designs on upper surface increases at stations D-H. The strength of shock wave is reduced noticeably at stations E and H of the robust design. Overall, the strength of shock wave is weaker over the robust design compared to the deterministic at $M_{max}$.

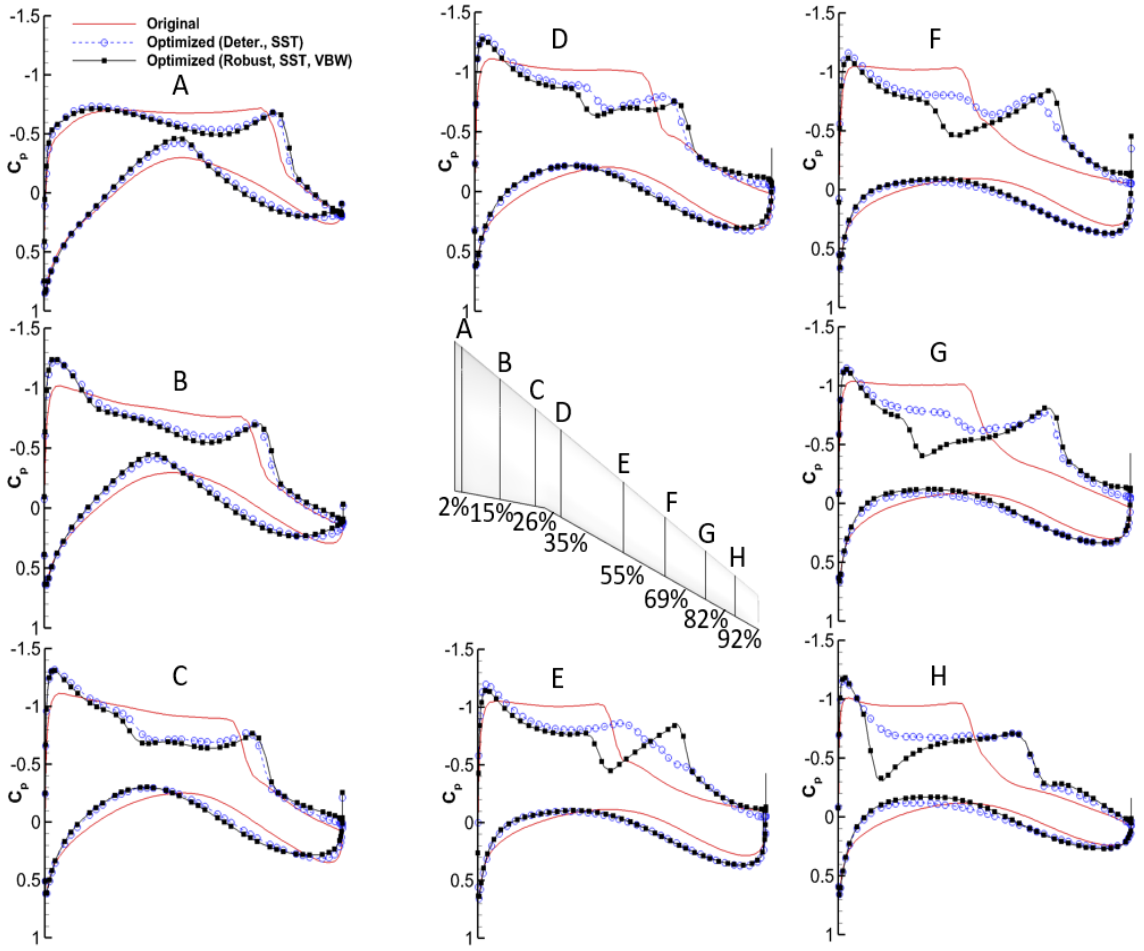


Figure 7.25. The comparison of $C_p$ over original and optimized shapes at $C_L = 0.65$ at $M_{nominal}$ for the best robust design (The VBW case with SST model).

Figure 7.27 shows the pressure coefficient contours over the optimized (deterministic and robust) and original shapes of the CRM wing at $M_{nominal}$ and at $M_{max}$ at $C_L = 0.65$ for the best robust design case which was obtained with VBW case and SST model. The strength of the shock wave is decreased with both deterministic and robust designs. The shock wave is weaker over the robust design compared to the deterministic design.

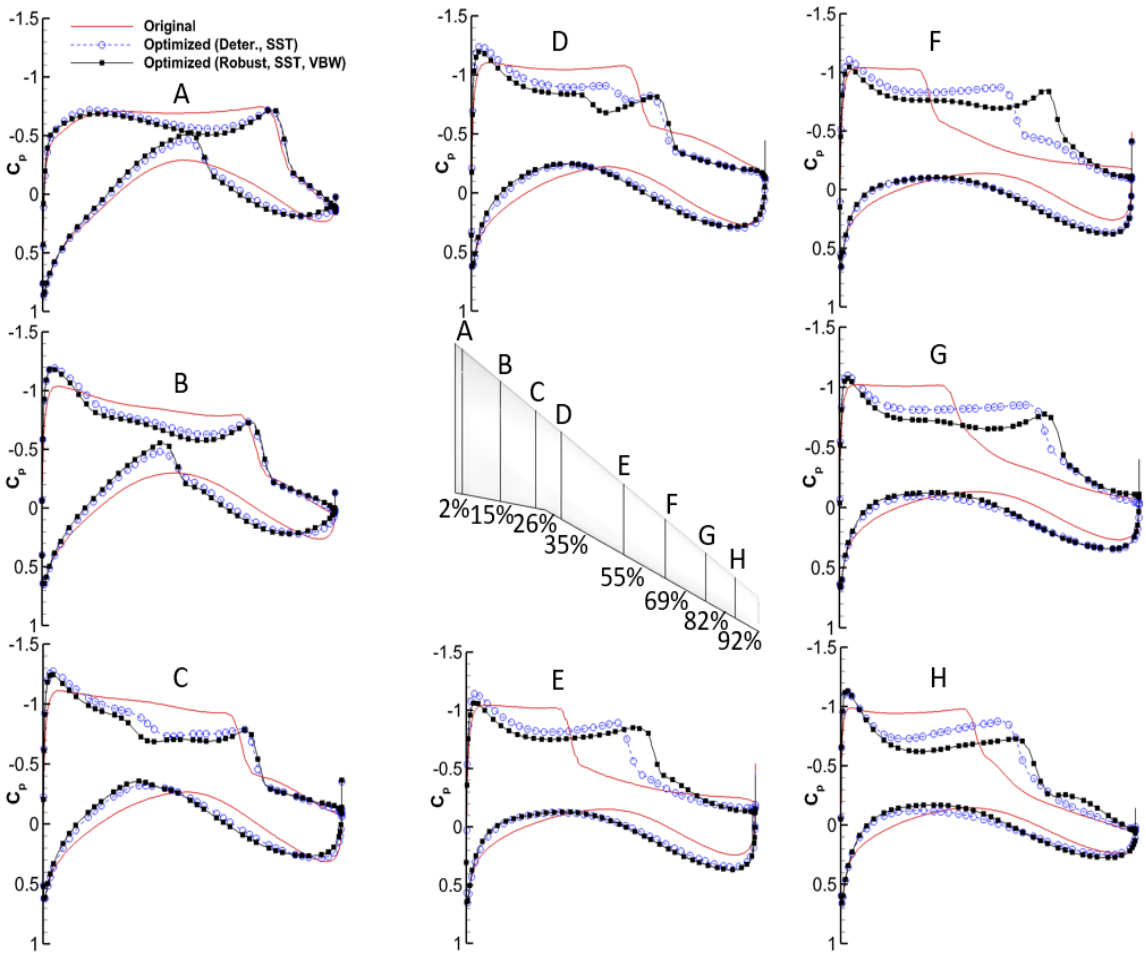


Figure 7.26. The comparison of $C_p$ over original and optimized shapes at $C_L = 0.65$ at $M_{max}$ for the best robust design (The VBW case with SST model).

Overall, the relatively flat profile of the $C_D$ under varying Mach number obtained with two turbulence models and three different weight cases indicates that the robustness of the wing improved significantly with stochastic optimization compared to the deterministic design. On the other hand, the robustness, especially with the VBW case, comes at the expense of an increase in $\mu_{C_D}$ compared to the $C_D$ values of the deterministic design.

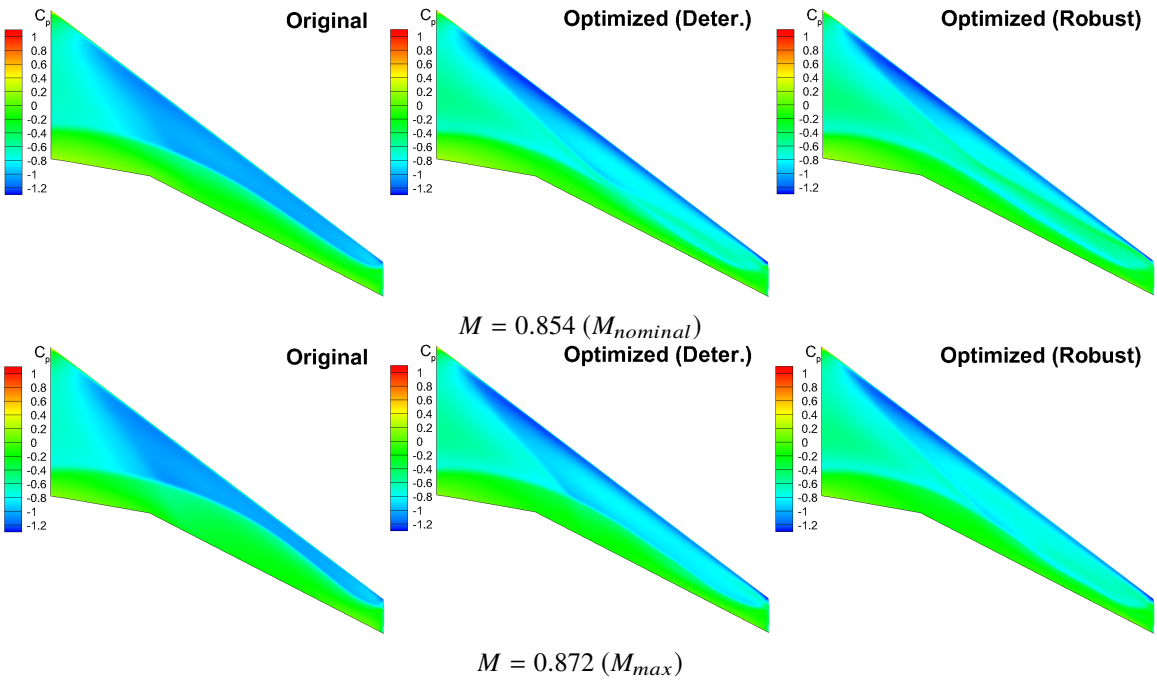


Figure 7.27. The $C_p$ contours at $C_L = 0.65$ over optimized and original shapes for the best robust design case (The VBW case, SST model).

# 8. CONCLUSIONS AND FUTURE WORK

The main objective of this study is to investigate the impact of the two commonly used turbulence models (SA and SST) in Reynolds-Averaged Navier-Stokes simulations on two-dimensional and three-dimensional optimum design obtained with gradient-based deterministic and robust aerodynamic shape optimization in transonic, viscous, turbulent flow. The impact of shape parameterization technique is also investigated for two-dimensional optimization problem. The impact of each turbulence model and shape parameterization technique is evaluated in terms of computational cost and difference in the shape and performance of the final design. The inherent variation of Mach number in transonic flow is modeled as the uncertain operating condition for the robust design study. The same shape parameterization techniques and turbulence models are first applied to the deterministic optimization of the same airfoil and wing geometry at the mean Mach number to make comparison between the deterministic and robust optimization findings. In the robust optimization methodology, stochastic expansions obtained with point-collocation non-intrusive polynomial chaos (NIPC) technique are utilized for uncertainty quantification due to their computational accuracy and efficiency in stochastic aerodynamics problems.

The objective of deterministic optimization of RAE2822 airfoil is to minimize the drag coefficient at a target lift coefficient of 0.824 (implemented in the objective function) subject to area constraint at $M = 0.734$. The deterministic optimization of RAE2822 airfoil is performed for B-spline curves with 20 control points, Hicks-Henne bump functions with 256 bump functions and $t_2 = 10$ (the width of the function), and FFD with $2 \times 40$ control lattice with the size of $[-0.1, 0.1]$ in the $z$ direction. The uniform distribution is implemented for the spacing of design variables over the geometry for each parameterization technique. The objective of robust optimization of RAE2822 airfoil is to minimize the mean and variance of drag coefficient at a mean of target $C_L$ of 0.824 (implemented in the

objective function) subject to area constraint. Mach number is considered as a uniformly distributed uncertain variable within the interval of $[0.725, 0.743]$. The robust optimization of RAE2822 airfoil is performed for B-spline curves with 20 control points, Hicks-Henne bump functions with 256 bump functions and $t_2 = 10$ (the width of the function), and FFD with $2 \times 20$ control lattice with the size of $[-0.1, 0.1]$ in the $z$ direction. A cosine distribution is used for the spacing of design variables over the geometry for B-spline curves and Hicks-Henne bump functions. Uniform distribution is used for the FFD technique. The optimization algorithm is started with $\alpha = 2.92°$ for the SA model and $\alpha = 3.06°$ for the SST model as an initial value both for deterministic and robust optimization. The angle of attack is defined as design variable for the deterministic and robust optimzation of the RAE2822 airfoil. The objective of deterministic optimization of CRM wing is to minimize the drag coefficient at a target lift coefficient of 0.65 (implemented in the objective function) subject to thickness constraint at $M = 0.85$. The deterministic optimization of CRM wing is performed for $24 \times 15 \times 2$ control lattice box (uniformly distributed over the geometry) with the size of $[-1.0, 1.0]$ in $z$ direction with FFD technique. The objective of robust optimization of CRM wing is to minimize the mean and variance of drag coefficient at a mean of target lift coefficient of 0.65 (implemented in the objective function) subject to thickness constraint. Mach number is considered as a uniformly distributed uncertain variable within the interval of $[0.827, 0.873]$. The control lattice box used for deterministic optimization is used for robust optimization of the CRM wing with the same FFD box size. The optimization algorithm is started with $\alpha = 3.56°$ for the SA model and $\alpha = 3.81°$ for the SST model as an initial value both for deterministic and robust optimization. The angle of attack is defined as design variable for the deterministic and robust optimzation of the CRM wing.

The results of the 2-D study show that the shape parameterization technique has larger effect on the computational cost than the turbulence model both for deterministic and robust optimization. In general, robust design tends to reduce the impact of the turbulence

model selection on the optimum shape and performance, whereas the turbulence model becomes important for the deterministic design at off-design conditions. The effect of the shape parameterization technique on robust design is more significant than the effect of the turbulence model. The robust design of streamlined aerodynamic shapes such as airfoils and wings lead to simplified flow fields over these geometries (e.g., with weak or no shock waves and no flow separation), which reduces the impact of the selection of the turbulence models as these models provide similar solutions over the same geometries at a range of operating conditions. The same observation can be made for the deterministic design but only at the design point. However, for aerodynamic designs obtained with deterministic or robust optimization that still include complex flow physics over the final configuration, and the turbulence model may still play an important role on the optimum shape and the performance prediction.

In 2-D study, the robust design obtained with the Hicks-Henne shape parameterization gives the best result in terms of the mean performance and the robustness over the Mach number range considered for both turbulence models. In this study, the improvement of the robustness of the final design obtained with stochastic optimization approach is also demonstrated over the Mach number range considered as the uncertain operating condition.

The results of the 3-D study show that the computational cost of optimization remains approximately constant for each turbulence model. It is observed that the drag reduction is larger with SST model than the SA model; however, the drag value of original shape is also significantly larger with the SST model. Similar to 2-D results, at the target $C_L$ and Mach number, the difference between the drag and pressure distributions for the optimal shapes obtained with each turbulence model is reduced, which indicates that the optimization tends to minimize the impact of selection of the turbulence model on the aerodynamic analysis. The difference in $C_D$ between two turbulence models at higher off-design Mach numbers is also reduced significantly. The impact of selection of turbulence model on the optimum shape and performance is reduced significantly over the uncertain

Mach number range considered with robust optimization. The effect of weight distribution in the objective function is larger than the effect of turbulence model on the optimal design obtained with robust optimization below the design Mach number value. Optimized wing geometries exhibit better performance under varying Mach number than the original wing for both turbulence models.

The future work may focus on the multidisciplinary optimization of the CRM wing. The deterministic and robust optimization approaches introduced in this work can be applied to the optimization of the aeroelastic response of the CRM wing. The effect of initial design on the computational cost, the shape and performance of the final design may be investigated by utilizing the deterministic optimium design as an initial geometry. In addition, the multimodality of robust aerodynamic shape optimization of CRM wing may be investigated in the future.

# APPENDIX A.

# GRID CONVERGENCE STUDY OF THE RAE2822

Three additional grids are generated based on the medium grid by conserving the original grid topology. These grids include a coarse grid and two finer grids, L1 and L2. The results presented in this study obtained from the deterministic and robust shape optimization studies utilized the medium grid as the baseline (RAE2822) mesh. It should be noted that, in some previous studies, the same medium grid used in the current work was also utilized for the validation of turbulence models [77, 78]. The coarse grid is generated by coarsening the medium grid by a factor of approximately 2 in both airfoil surface and normal directions. This ratio of 2 was strictly enforced in the structured part of the grid (i.e., region with quadrilaterals) close to the surface. L1 grid is created by refining the medium grid by a factor of approximately 2 in both directions while this ratio of 2 was again strictly enforced in the structured part of the grid close to the surface. In a similar way, L2 grid is generated by refining the L1 grid by a factor of approximately 2 in both directions.

Tables A1 and A2 give a summary of the lift ($C_L$) and drag ($C_D$) coefficients obtained for the RAE2822 airfoil with the four grid levels outlined above. The simulations for all grid levels are performed at a Mach number of 0.734, Re number of $6.5 \times 10^6$, $\alpha = 2.92^\circ$ for SA and $\alpha = 3.06^\circ$ for SST model. The $C_D$ of L1 and L2 grids with SA model are 4 and 3 drag counts higher than medium grid, respectively. The $C_D$ of L1 and L2 grids with SST model are 1 drag count higher than medium grid. The comparison of $C_p$ distributions obtained with the four grid levels and SA and SST models are presented in Figure A1. The $C_p$ distributions of all grid levels except the coarse grid are close to each other for each turbulence model and they are in good agreement with the experimental data [79]. Overall, the grid convergence results reported here indicate that the medium grid level utilized in this study has sufficient accuracy in resolving the quantities of interest used in aerodynamic shape optimization of RAE2822 transonic airfoil.

Table A1. Summary of the grid convergence study with SA model.

| Grid | Total Cells | $C_L$ | $C_D$ | $z^+$ |
|---|---|---|---|---|
| L2 | 365,208 | 0.845 | 0.0212 | 0.6 |
| L1 | 90,410 | 0.842 | 0.0213 | 0.95 |
| Medium | 22,842 | 0.824 | 0.0209 | 1.0 |
| Coarse | 7,382 | 0.764 | 0.0197 | 5.2 |

Table A2. Summary of the grid convergence study with SST model.

| Grid | Total Cells | $C_L$ | $C_D$ | $z^+$ |
|---|---|---|---|---|
| L2 | 365,208 | 0.833 | 0.0218 | 0.6 |
| L1 | 90,410 | 0.832 | 0.0218 | 0.95 |
| Medium | 22,842 | 0.824 | 0.0217 | 1.0 |
| Coarse | 7,382 | 0.786 | 0.0228 | 5.2 |

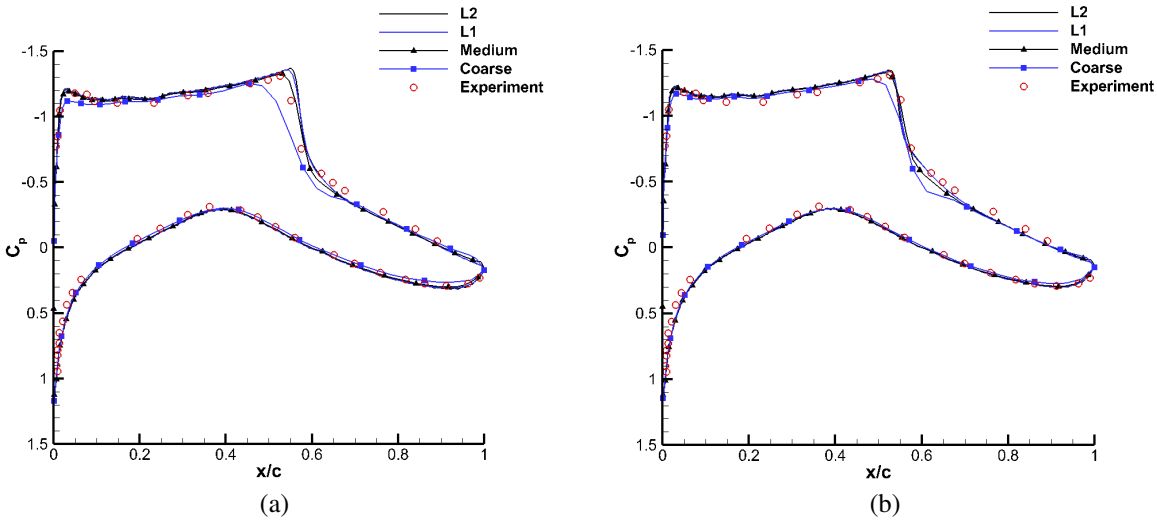


Figure A1. The comparison of $C_p$ over RAE2822 airfoil at different grid levels with SA and SST models. a) $C_p$ with SA model. b) $C_p$ with SST model.

# APPENDIX B.

# GRID CONVERGENCE STUDY OF THE CRM

Three additional grids are created based on the medium grid by conserving the original grid topology. The additional grids include one fine and two coarser grids, C1 and C2. The results presented in the study obtained from deterministic and robust shape optimization studies used the medium grid as the baseline (CRM) mesh. The fine grid is generated by refining the medium grid by a factor of 2 in each computational direction. The C1 is created by coarsening the medium grid by the factor of 2 in the streamwise direction. The C2 is generated by coarsening the medium grid by the factor of 2 in each computational direction.

Tables B1 and B2 give a summary of the lift ($C_L$) and drag ($C_D$) coefficients obtained for the CRM wing with the four grid levels outlined above. The simulations for all grid levels are performed at a Mach number of 0.85, Re number of $5.0 \times 10^6$, $\alpha = 3.56^\circ$ for SA and $\alpha = 3.81^\circ$ for SST model. The $C_D$ of the fine grid with SA and SST models are 3 and 5 drag counts higher than the medium grid, respectively. The $C_D$ of the C1 and C2 with SA model are 12 and 9 drag counts higher than the medium grid, respectively. The $C_D$ of the C1 and C2 with SST model are 6 and 32 drag counts higher than the medium grid, respectively. The comparison of $C_p$ distributions obtained with four grid levels with SA and SST models are presented in Figure B1 and B2, respectively. The $C_p$ distributions of the fine and medium grid are close to each other at each station for each turbulence model. The $C_p$ distribution of C1 and C2 are significantly different than both fine and medium grids at all stations except station A for each turbulence model. Overall, the grid convergence results reported here indicate that the medium grid level utilized in this study has sufficient accuracy in resolving the quantities of interest used in aerodynamic shape optimization of the CRM wing.

Table B1. Summary of the grid convergence study with SA model.

| Grid | Total Cells | $C_L$ | $C_D$ | $z^+$ |
|---|---|---|---|---|
| Fine | 3,604,480 | 0.669 | 0.0359 | 0.69 |
| Medium | 450,560 | 0.65 | 0.0356 | 1.58 |
| C1 | 265,440 | 0.607 | 0.0344 | 1.81 |
| C2 | 56,320 | 0.591 | 0.0365 | 4.44 |

Table B2. Summary of the grid convergence study with SST model.

| Grid | Total Cells | $C_L$ | $C_D$ | $z^+$ |
|---|---|---|---|---|
| Fine | 3,604,480 | 0.649 | 0.0371 | 0.68 |
| Medium | 450,560 | 0.65 | 0.0376 | 1.56 |
| C1 | 265,440 | 0.611 | 0.0370 | 1.73 |
| C2 | 56,320 | 0.624 | 0.0408 | 4.38 |

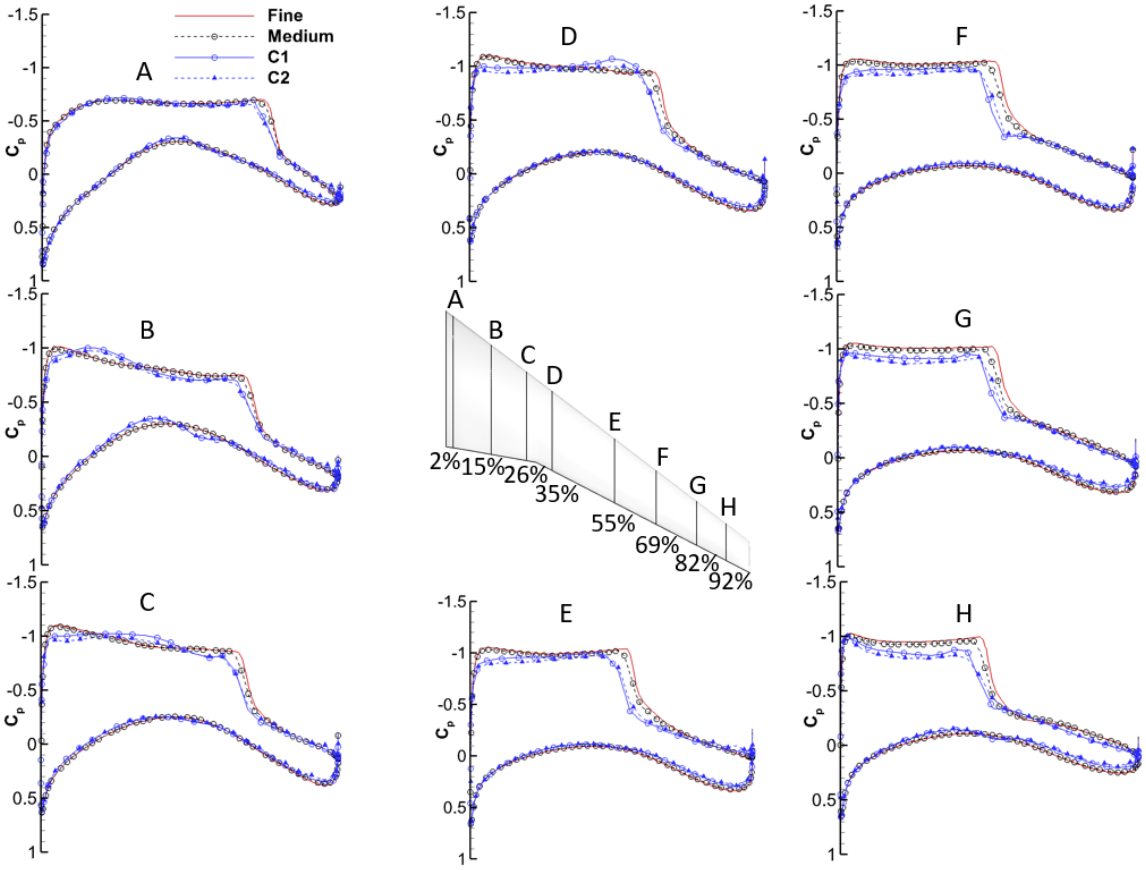


Figure B1. The comparison of $C_p$ over CRM wing at various spanwise locations at different grid levels with SA model.

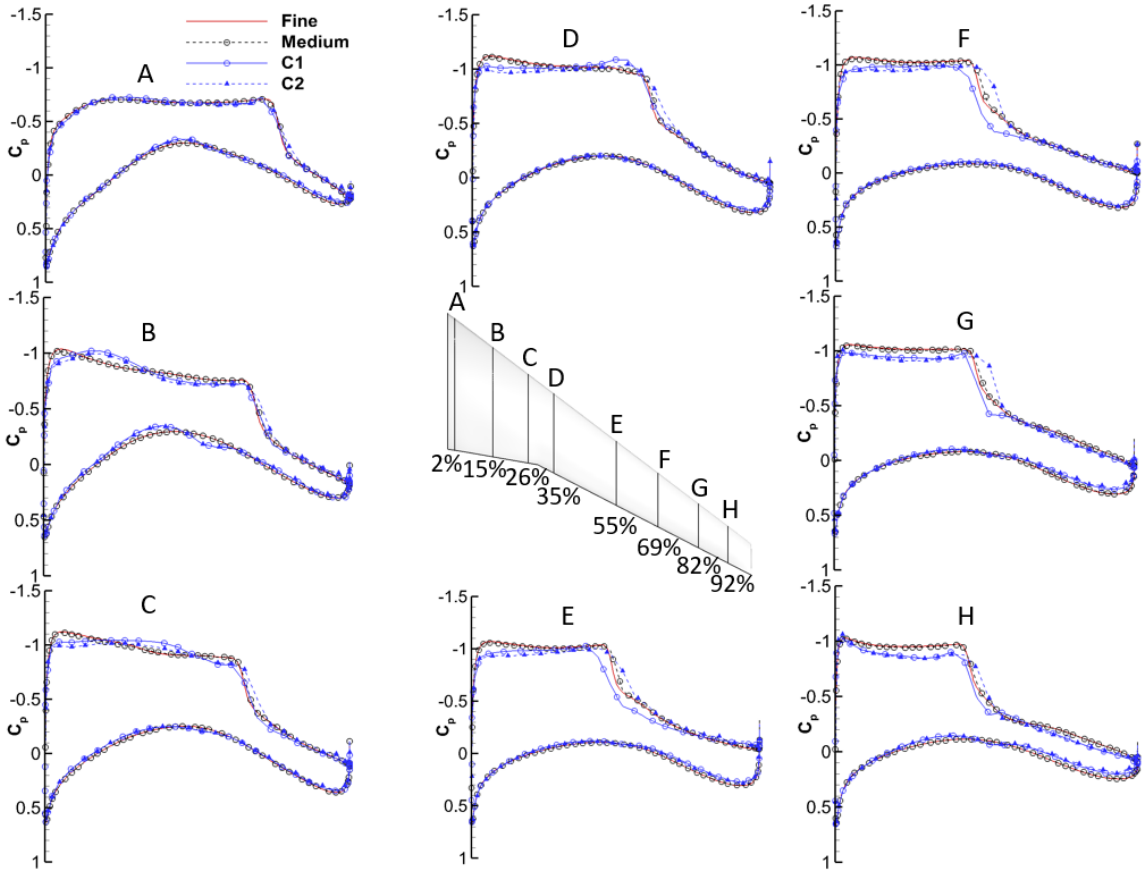


Figure B2. The comparison of $C_p$ over CRM wing at various spanwise locations at different grid levels with SST model.

# APPENDIX C.

# IDENTIFICATION OF OPTIMUM FACTORS FOR THE 2-D SHAPE PARAMETERIZATION TECHNIQUES

The objective of the study presented in this section is to investigate and identify the optimum number of design variables and their distribution(cosine or uniform) over the geometry for each shape parameterization technique (Hicks-Henne, Bspline and Free Form Deformation) for robust aerodynamic shape optimization of RAE2822 airfoil described in Section 6. The parametric study for each shape parameterization technique is evaluated in terms of the computational cost, the shape of final design, and its performance in deterministic and robust aerodynamic shape optimization.

## 1. PARAMETRIC STUDY FOR DETERMINISTIC OPTIMIZATION

### 1.1. PROBLEM STATEMENT

The objective of deterministic optimization is to reduce the drag coefficient $C_D$ of the airfoil at a specified Mach number subject to a specified minimum lift coefficient $C_L$, and area constraint. The optimization of RAE2822 airfoil is performed for viscous turbulent flow at a Mach number of $M = 0.734$ and a $Re$ number of $6.5 \times 10^6$. The shape parameterization techniques studies included B-spline curves with 12, 16, 20, 40 and 60 control points, Hicks-Henne bump function with $t_2 = 10$, 20 and 30 (the width of the function) and with 20, 38, 40, 60, 80, 96, 128, 192 and 256 bump functions, FFD with $2\times10$, $2\times20$, $2\times30$, $2\times40$, $2\times48$, $2\times64$, $2\times96$, and $2\times128$ control lattice with the size of control lattice of $[-0.1, 0.1]$, $[-0.09, 0.09]$, $[-0.08, 0.08]$, and $[-0.07, 0.07]$. In FFD, the boundary of each control point is set $[0.5z_i, 1.5z_i]$ and $[0.25z_i, 1.75z_i]$ where $z_i$ is the $z$ coordinate of $i^{th}$ control point at each iteration. In addition, the uniform (UD) distribution is demonstrated for the spacing of design variables along the airfoil chord for each parameterization technique. The cosine (CoD) distribution is demonstrated for the spacing of design variables along the airfoil chord for B-spline and Hicks-Henne techniques. The x-location of design points based on cosine distribution is obtained with Equation (6.12). The angle of attack is defined as a design variable for all cases and $C_L$ constraint is included in the objective function,

setting the target $C_L$ as 0.824. For B-spline curves, the angle of attack is constraint within the interval $[-10.0°, 10.0°]$ and the non-dimensionalized vertical position of each control point is limited with the interval $[-0.1, 0.1]$. For Hicks-Henne bump function, the angle of attack is constraint within the interval $[2.0°, 4.0°]$. The effect of function amplitude limit set for each iteration is studied for intervals $[-0.1, 0.1]$ and $[-0.01, 0.01]$. For FFD technique, the angle of attack is constrained within the $[2.0°, 4.0°]$. The optimization algorithm is started with the original airfoil shape and $\alpha = 2.92°$ as an initial value. A weighted objective function is defined to include the $C_L$ constraint besides the main objective of the minimization of the $C_D$:

$$minimize \quad W_1 C_D^2 + W_2 \left( C_{L_{Target}} - C_L \right)^2 \tag{1}$$

where the weights $W_1$ is $10^4$ and $W_2$ is $10^1$. The contribution of each term in terms of their percentage is investigated on test cases and the optimum combination is selected according to test case outputs.

## 1.2. DETERMINISTIC OPTIMIZATION RESULTS

Figure 1 shows deterministic optimal shapes and original shape of RAE2822 using Hicks-Henne method as the parameterization technique in the optimization. These cases were obtained with $t_2 = 10$ and the interval $[-0.01, 0.01]$ for the function amplitude limit.

The $C_L$ of the original shape is 0.824 and the $C_D$ is 0.0209 at $\alpha = 2.92°$. The area of the airfoil is non-dimensionalized by $c^2$, which is 0.0778 for the original geometry and the objective function value at the first iteration is 4.3882. The numerical results of the optimized shapes in Figure 1 is given in Table 1. According to data in Table 1, the drag is reduced 77 drag counts at 128bf and 192bf uniformly distributed cases, 76 drag counts at 256bf (UD) and 78 drag counts at 256bf (CoD). 256bf with UD and CoD converged in 21 and 27 iterations, respectively. However, 128bf and 192bf with UD converged 45 and 29

iterations, respectively. According to this data, one of the finding is the number of bump function has a significant impact on computational cost. As it can be seen in Figure 1, optimized shapes with UD are very similar and their lift and drag coefficients are close as well. There is a slight difference with CoD case which can be due to the $x$-location of the bump functions. This also affects the aerodynamic coefficients of the optimized shapes. 256bf (UD) at $t_2 = 10$ with the interval $[-0.01, 0.01]$ is selected as the best case.

The pressure distributions of original and optimized shapes are presented in Figure 2. The shock wave over the original shape is weakened for the optimized shapes and UD shapes exhibit the same surface pressure distribution. For the CoD case, the distance

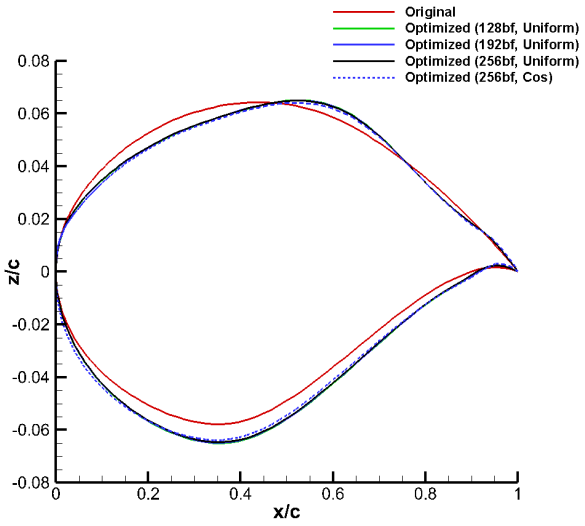


Figure 1. The comparison of the optimal (deterministic) and original shapes for the RAE2822 airfoil (Hicks-Henne Shape Parameterization).

Table 1. Numerical Results for the original and optimized shapes (Hicks-Henne Shape Parameterization).

| # of Bump Functions | $C_L$ | $C_D$ | Objective Func. | Area | # of Iterations |
|---|---|---|---|---|---|
| Original | 0.824 | 0.0209 | 4.3882 | 0.0778 | - |
| 128bf (UD) | 0.829 | 0.0132 | 1.7519 | 0.0815 | 45 |
| 192bf (UD) | 0.828 | 0.0132 | 1.7360 | 0.0814 | 29 |
| 256bf (UD) | 0.829 | 0.0133 | 1.7565 | 0.0813 | 21 |
| 256bf (CoD) | 0.840 | 0.0131 | 1.7223 | 0.0806 | 27 |

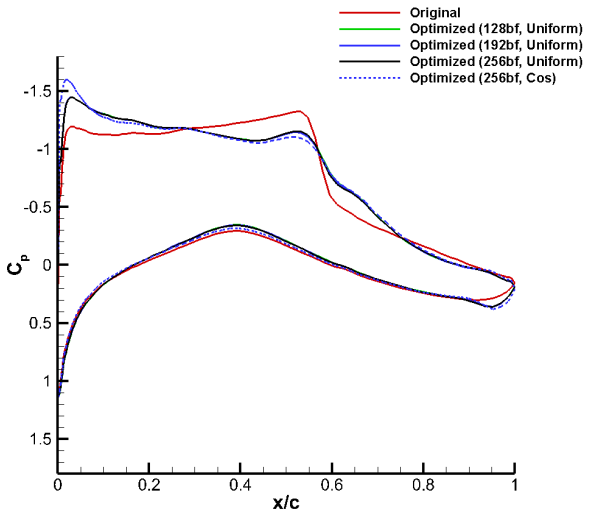


Figure 2. The comparison of $C_p$ distribution of the optimal (deterministic) and original shape for the RAE2822 case (Hicks-Henne Shape Parameterization).

between $x$-locations of bump functions is small in the vicinity of the leading and trailing edges. The effect of this feature can be seen on the pressure distribution of optimized shape especially in peak suction pressure close to the leading edge.

Figure 3 shows the Mach contours of optimized and original shape of RAE2822. The shock wave over the original shape, which causes drag and reduces airfoil performance, is significantly weakened on the optimized shape. The Mach contours of optimized shapes (256bf) with respect to different distributions is indistinguishable.

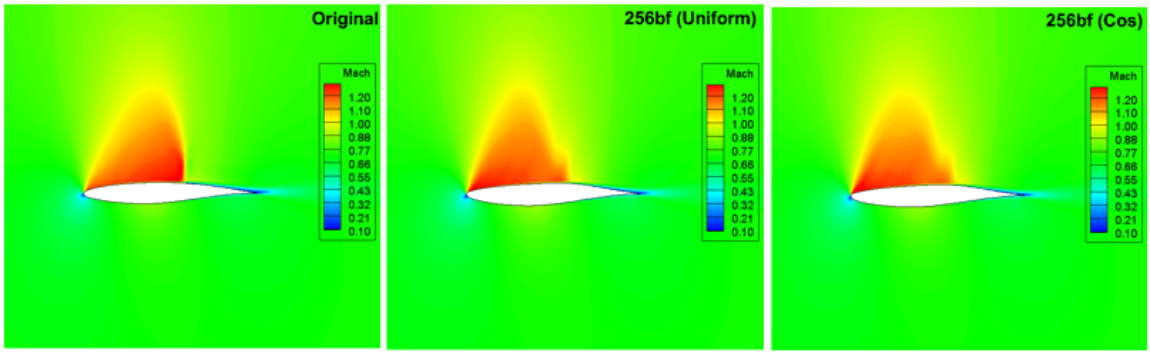


Figure 3. The contours showing Mach number over optimized (deterministic) and original shape of RAE2822 (Hicks-Henne Shape Parameterization).

In Figure 4, $C_D$, $C_L$ and the number of iterations to converge are presented for two distributions (UD and CoD) and three function amplitude ($t_2$) values as a function of the number of bump functions (design variables) with the function amplitude boundary $[-0.1, 0.1]$. Drag coefficients are lower with less number of bump functions, however there is a significant increment after 96bf. Lift coefficient trends and the number of iterations to converge are consistent with the $C_D$ trends. $C_L$ values at UD cases are closer to the target $C_L$ (0.824) compared to the cosine distribution cases. $C_L$ for UD, 20bf case is lower than target $C_L$, which is likely due to the fact that $C_L$ constraint is integrated into the objective function instead of defining as a constraint separately. The number of iterations for convergence decreases consistently as a function of the number of bump functions. Since the computational time for each iteration is approximately the same for all cases, it can be said that the computational time for each case decreases significantly with the increase of the number of bump functions (design variables). According to Figure 4, 40bf with UD at $t_2 = 10$ within the interval $[-0.1, 0.1]$ is the optimal case in terms of drag value and computational cost.

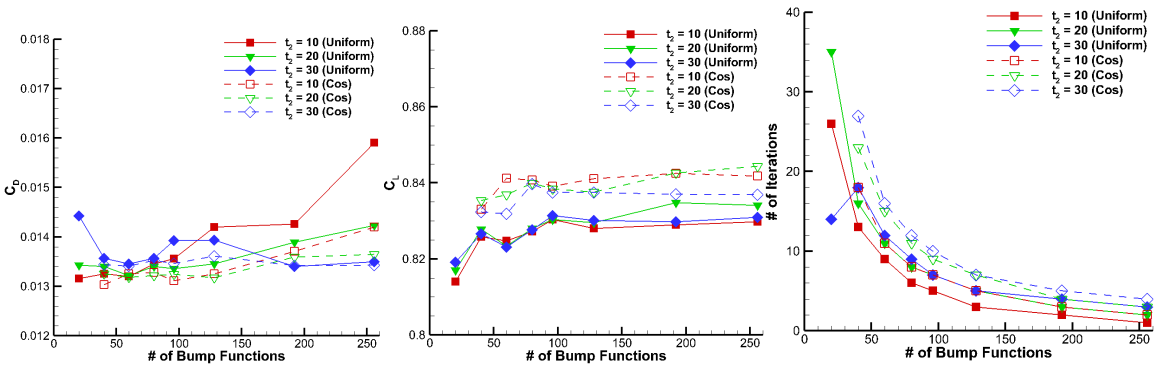


(a) (b) (c)

Figure 4. (a) $C_D$ vs. number of bump functions for UD, CoD, and $t_2$ values. (b) $C_L$ vs. number of bump functions for UD, CoD, and $t_2$ values. (c) The number of iterations to converge vs. number of bump functions for UD, CoD, and $t_2$ values. (For all plots, the function amplitude boundary is $[-0.1, 0.1]$).

In Figure 5, $C_D$, $C_L$ and the number of iterations to converge are presented for two distributions (UD and CoD) and three function amplitude ($t_2$) values as a function of the number of bump functions (design variables) with the function amplitude boundary set to $[-0.01, 0.01]$. Drag coefficient decreases with the number of bump functions for both distributions and all $t_2$ values. In terms of $C_D$, UD and CoD cases with $t_2 = 10$ for all number of bump functions perform better, converging to a $C_D$ value of approximately 77 drag counts beyond 50bf (design variables). $C_L$ constraint is satisfied for all cases which shows the effect of boundary set for bump function amplitudes on this quantity. Reducing the number of design variables increases the number of iterations to converge which directly affects the computational cost compared to the boundary with the interval $[-0.1, 0.1]$. Among all cases, 256 bf (UD) with $t_2 = 10$ within the interval $[-0.01, 0.01]$ is observed as the best case in terms of the computational cost, reduction in drag coefficient and $C_L$ constraint satisfaction.

Hicks-Henne bump function results show consistency when the function amplitude is limited within the interval $[-0.01, 0.01]$ at each iteration. The deformation of geometry at each iteration is slight, therefore the number of iterations to converge is higher compared to the case set with the interval $[-0.1, 0.1]$. The latter has better performance in terms of

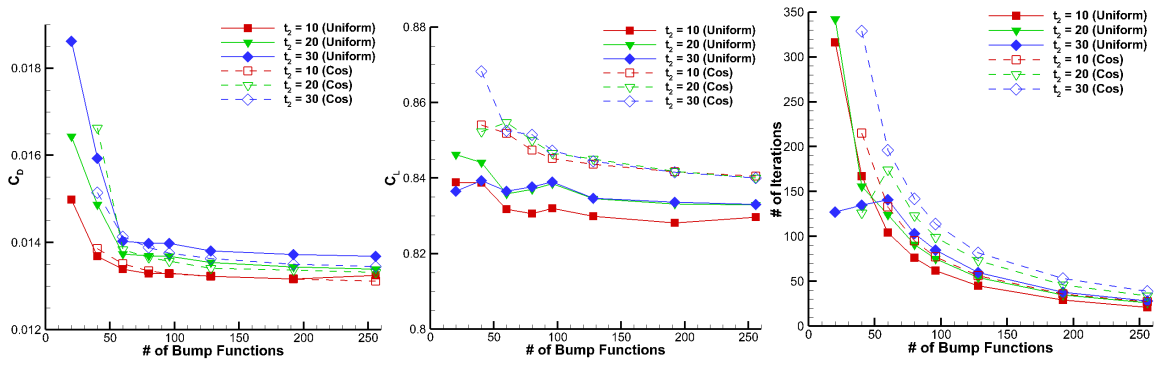


(a) (b) (c)

Figure 5. (a) $C_D$ vs. number of bump functions for UD, CoD, and $t_2$ values. (b) $C_L$ vs. number of bump functions for UD, CoD, and $t_2$ values. (c) The number of iterations to converge vs. number of bump functions for UD, CoD, and $t_2$ values. (For all plots, the function amplitude boundary is $[-0.01, 0.01]$).

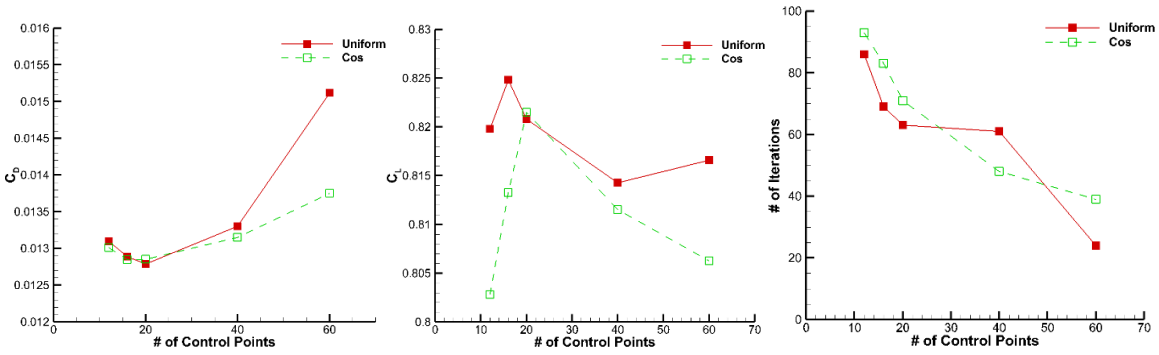


(a) (b) (c)

Figure 6. (a) $C_D$ vs. number of control points for UD and CoD. (b) $C_L$ vs. number of control points for UD and CoD. (c) The number of iterations to converge vs. number of control points for UD and CoD.

computational cost, however consistency problem is observed with respect to the number of bump functions, function amplitudes and distribution type due to high geometry deformation at each iteration.

Figure 6 presents $C_D$, $C_L$ and the number of iterations to converge as a function of the number of control points (cp) or design variables for two distributions (UD and CoD). The drag coefficient decreases and the lift coefficient satisfies the constraint up to 20cp. Beyond this value, the former increases and the latter violates the constraint for both distributions. The number of iterations to converge decreases with the increase of the number of control points for each distribution. Among all cases utilizing B-spline curves, 20cp is observed as the best case in terms of the drag reduction corresponding to a 81 drag count change, which is 5 drag counts more compared the Hicks-Henne bump function best case. The Table 2 includes an outline of the results obtained with the B-spline cases. As can be seen from this table, the drag coefficient reduction is 81 drag counts for UD case and 80 drag counts for the CoD case. The former converged in 63 iterations and the latter converged in 71 iterations. Lift coefficients are 0.820 and 0.821 respectively. The area of airfoil shape increases in both cases from 0.0778 to 0.0795 (the former) and 0.0799 (the latter). The objective function reduces from 4.3882 to 1.6351 (UD case) and 1.6501 (CoD case).

Table 2. Numerical Results for the original and optimized shapes (B-spline Shape Parameterization).

| # of Bump Functions | $C_L$ | $C_D$ | Objective Func. | Area | # of Iterations |
|---|---|---|---|---|---|
| Original | 0.824 | 0.0209 | 4.3882 | 0.0778 | - |
| 16cp (UD) | 0.824 | 0.0129 | 1.6609 | 0.0795 | 69 |
| 16cp (CoD) | 0.813 | 0.0129 | 1.6514 | 0.0799 | 83 |
| 20cp (UD) | 0.820 | 0.0128 | 1.6351 | 0.0795 | 63 |
| 20cp (CoD) | 0.821 | 0.0129 | 1.6501 | 0.0799 | 71 |

Figure 7 shows the comparison of the shapes and the pressure distribution between the original and optimized airfoils obtained with B-spline curve parameterization with 20cp both for UD and CoD cases. Since the aerodynamic coefficients are similar, the shapes of the optimized airfoils and their surface pressure distributions are close to each other as expected. The optimized shapes and $C_p$ distributions in the vicinity of the leading edge (suction region) slightly different due to the difference in $x$-location of control points for each distribution. As it can be seen from Figure 7, shock wave becomes weaker on the optimized shapes which improves the drag coefficient and the performance of the airfoil.

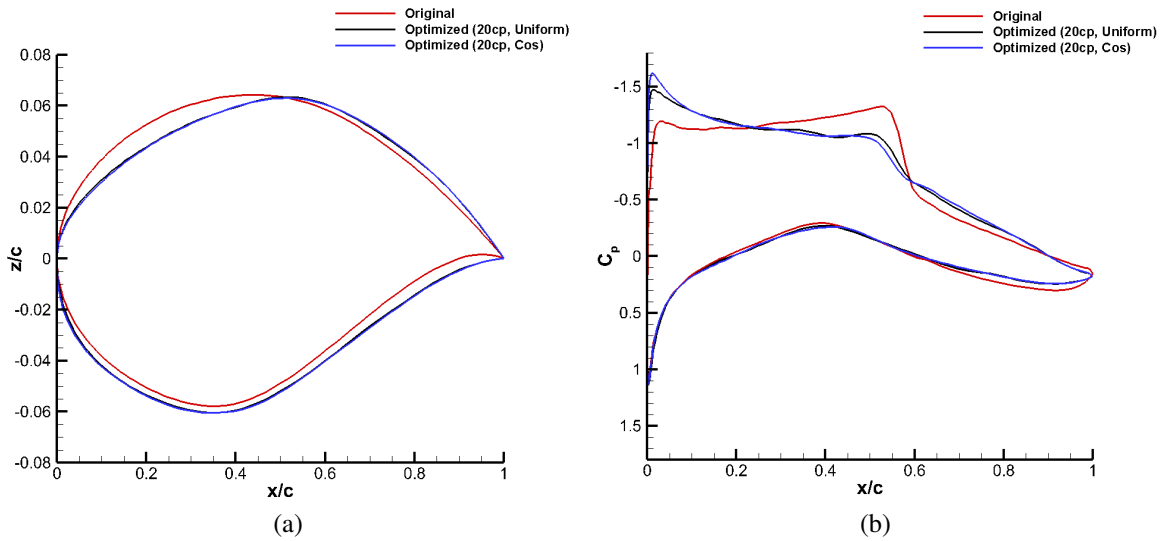


Figure 7. (a) The comparison of original and optimized shapes (20cp with UD and CoD). (b) The $C_p$ comparison of original and optimized shapes (20cp with UD and CoD).

In Figure 8, the shapes and pressure distributions of original and optimized airfoils with 16cp, 20cp and 60cp (UD case) are compared. The optimized shapes with 16cp and 20cp are similar and the shock wave is weakened as can be seen from Figure 10(b). On the other hand, there is no significant shape deformation for the 60cp case compared to the other two cases with lower number of control points. For the 60cp case, the shock wave slightly moves upstream with a minor reduction in strength.

The original and optimized shapes obtained with each shape parameterization technique for the best cases are compared in Figure 9. The best cases for B-spline and Hicks-Henne parameterization techniques are 20cp and 256bf with UD, respectively. The methodology of shape modification is different with each technique, therefore the optimized shapes and their aerodynamic coefficient values are different. The former converges in 63 iterations and the latter converges in 27 iterations. Their common feature is to weaken the shock wave. Based on Figure 9, B-spline curves handle the shock wave better, however it has a disadvantage on the computational cost. Hence, Hicks-Henne bump function technique with 256bf

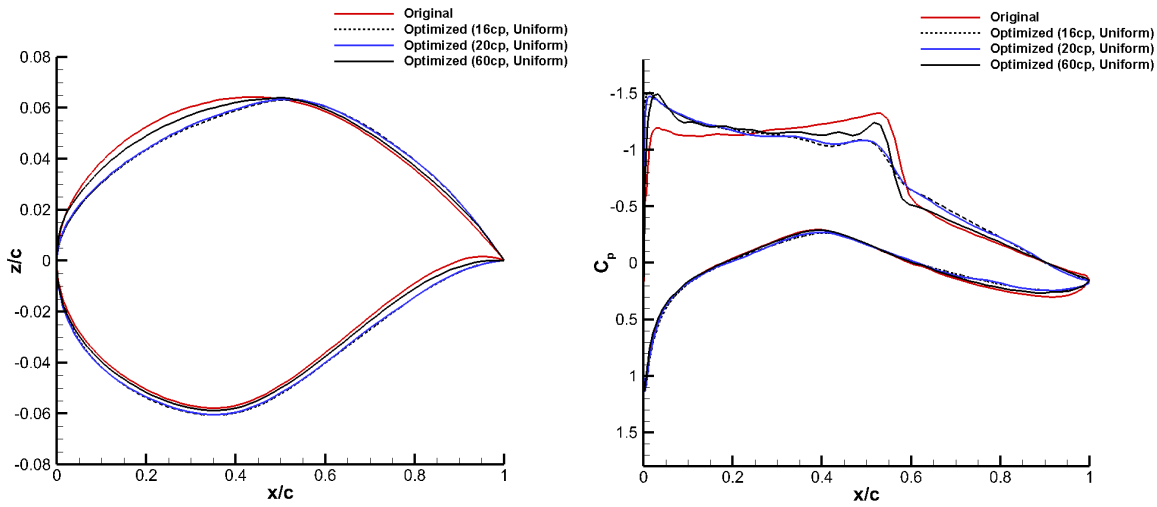


(a) (b)

Figure 8. (a) The comparison of original and optimized shapes (16cp, 20cp and 60cp with UD). (b) The $C_p$ comparison of original and optimized shapes (16cp, 20cp and 60cp with UD).

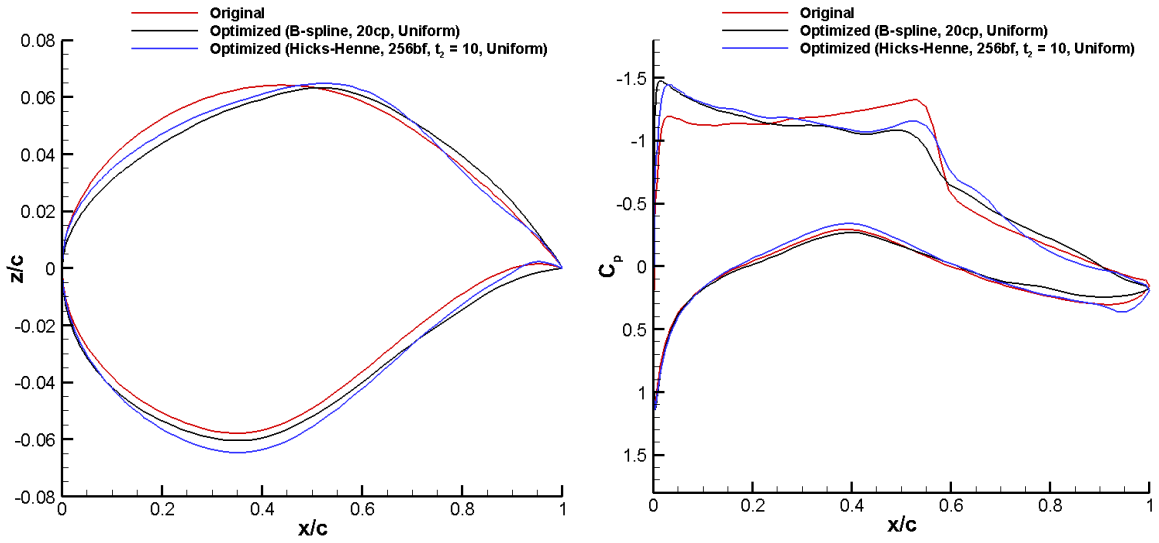


Figure 9. (a) The comparison of original and optimized shapes of best cases obtained with Hicks-Henne bump function and B-spline curve parameterization. (b) The $C_p$ comparison of original and optimized shapes of best cases obtained with Hicks-Henne bump function and B-spline curve parameterization.

(UD) with $t_2 = 10$ within the interval $[-0.01, 0.01]$ seems to be an appropriate combination for the deterministic optimization of RAE2822 in terms of aerodynamic coefficients and computational cost.

In Figure 10, the $C_D$, $C_L$ and the number of iterations to converge is presented for the uniform distribution and the four control lattice size with the boundary of each control point of $[0.5z_i, 1.5z_i]$. The drag coefficient reduces up to 96 design variables, however the $C_L$ constraint is satisfied with 20 and 40 design variables. The former increases after starting from 128 design variables and the latter violates the constraint starting from 60 design variables. The number of iterations to converge decreases with the increase of the control points for each distribution. Among all cases, the lattice box of $2 \times 40$ is selected as best case according to the the number of iterations to converge and the reduction in $C_D$.

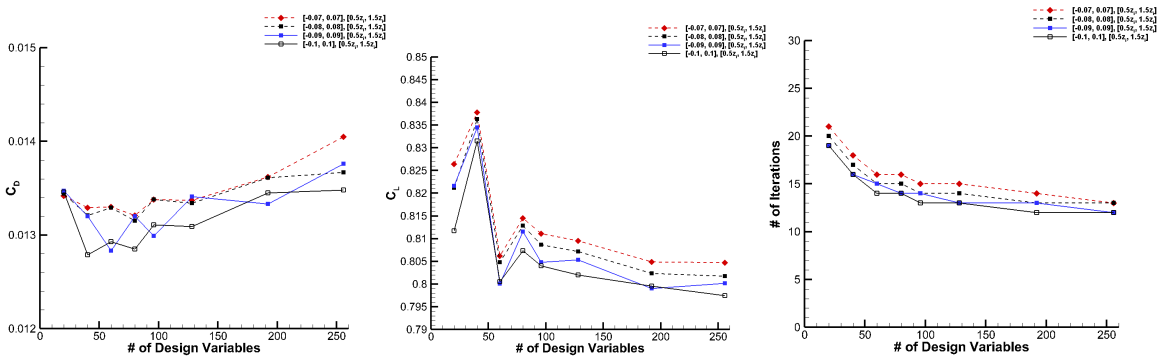


(a) (b) (c)

Figure 10. (a) $C_D$ vs. number of columns. (b) $C_L$ vs. number of columns. (c) The number of iterations to converge vs. number of columns with the boundary interval of $[0.5z_i, 1.5z_i]$.

The numerical results for the original and optimized shapes with FFD technique is given in Table 3. The $C_D$ is reduced 80 drag counts with the lattice box of $2 \times 30$, 81 drag counts with the lattice box of $2 \times 40$, and 79 drag counts with the lattice box of $2 \times 64$. The number of iterations to converge is almost the same for the FFD cases given in the table.

Figure 11 shows the shapes and pressure distributions of the original and optimized airfoils with the lattice box of $2 \times 40$. There is a significant difference between the original and optimal shapes on both upper and lower surfaces. The strength of shock wave is noticeably weakened with FFD technique.

Table 3. Numerical Results for the original and optimized shapes (FFD Shape Parameterization).

| Lattice Box | $C_L$ | $C_D$ | Objective Func. | Area | # of Iterations |
|---|---|---|---|---|---|
| Original | 0.824 | 0.0209 | 4.3882 | 0.0778 | - |
| $2 \times 30$ | 0.800 | 0.0129 | 1.6501 | 0.0798 | 14 |
| $2 \times 40$ | 0.807 | 0.0128 | 1.6519 | 0.0795 | 13 |
| $2 \times 64$ | 0.802 | 0.0131 | 1.6508 | 0.0799 | 12 |

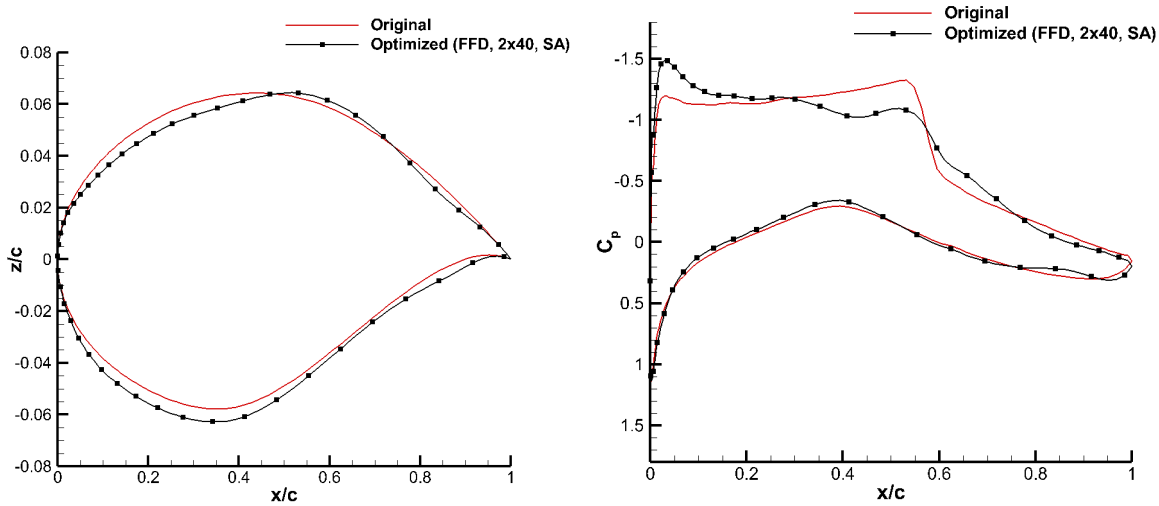


(a) (b)

Figure 11. (a) The comparison of original and optimized shapes. (b) The $C_p$ comparison of original and optimized shapes. (The lattice box of $2 \times 40$)

## 2. PARAMETRIC STUDY FOR ROBUST OPTIMIZATION

### 2.1. PROBLEM STATEMENT

The robust design is applied to the same RAE2822 case considered for deterministic optimization, however the Mach number is considered as a uniformly distributed uncertain variable within the interval $[0.7253, 0.7427]$. The nominal (mean) Mach number is 0.734 at which the deterministic optimization is performed. For robust optimization, the weighted objective function is formulated to minimize the mean and the variance of $C_D$ simultaneously while keeping the mean of target $C_L$ constant:

$$minimize \quad W_1 \mu_{C_D} + W_2 \sigma^2_{C_D} + W_3 \left( \mu_{C_{L_{Target}}} - \mu_{C_L} \right)^2 \tag{2}$$

where the weights $W_1$, $W_2$ and $W_3$ are selected as $1.0 \times 10^2$, $2.5 \times 10^5$ and $1.5 \times 10^1$ respectively based on a parametric study. The mean of target $C_L$ is defined as 0.824 and the optimization algorithm is started with $\alpha = 2.92°$ as an initial value. In this formulation the

first term is related to optimization of the mean performance (i.e., minimization of the mean of drag coefficient) and the second term is to achieve the robustness of the design under the variation of the Mach number (i.e., the minimization of the variance of the drag coefficient) and the third term is for the implementation of $C_L$ constraint. In robust optimization, Hicks-Henne shape parameterization technique is performed using the same number and distributions of bump functions considered in deterministic optimization with $t_2$ = 10, 20 and 30. The boundary of function amplitude and the angle of attack are defined with the interval $[-0.1, 0.1]$ and $[2.0°, 4.0°]$, respectively. B-spline curves approach is also evaluated with the same number and distribution of design variables as deterministic optimization when the boundary of control points is described with the interval $[-0.1, 0.1]$ and the angle of attack is bounded with the interval $[-10.0°, 10.0°]$.

## 2.2. ROBUST OPTIMIZATION RESULTS

Figure 12 presents the mean and standard deviation of drag coefficient, the number of iterations to converge and the mean of lift coefficient under varying number of bump functions, distributions and function widths. Mostly all the cases between 64 and 128 bump functions have significant success about the reduction in $\mu_{C_D}$ and $\sigma_{C_D}$ at both distributions and three function widths. In this range, bump functions with CoD performs better results in terms of $\mu_{C_D}$ and $\sigma_{C_D}$. However, when the combination of mean and standard deviation of drag coefficient (the objective function of optimized shape) is considered, UD with $t_2$ = 10 is advantageous among all cases in this range. The mean of lift coefficient constraint is implemented into the objective function instead of setting as a contraint, therefore it is usually slightly lower than $\mu_{C_{L_{Target}}}$. According to Figure 12(b), the $\mu_{C_L}$ of uniformly distributed cases after 64 bump functions at $t_2$ = 30 are approximately 0.8. Uniformly distributed bump functions are advantageous in terms of computational cost, especially for uniformly distributed with $t_2$ = 10. The number of CFD solver run for optimized shape is the parameter to measure the vast cost of robust design. In this study, each iteration consists

of 6 samples and direct and adjoint (for drag and lift coefficients) solvers are called for each sample, therefore 12 CFD runs occur at each iteration (6 flow solutions and 6 for the adjoint solver runs). As an example, 20bf (UD) with $t_2 = 10$ case converges in 39 iterations which requires 468 CFD runs. Consequently, uniformly distributed bump function cases with $t_2 = 10$ are definitely advantageous in terms of computational cost.

Based on Figure 12, 60bf (CoD) with $t_2 = 10$ is selected as the best case with a $\sigma_{C_D}$ of 0.0038 and 73 drag count reduction in $\mu_{C_D}$. The convergence criterion is satisfied in 15 iterations and $\mu_{C_L}$ of optimized shape is 0.803 at $\alpha = 2.9316°$. The area is increased from 0.0778 to 0.0805. The objective function decreases from 3.4463 to 1.4023.

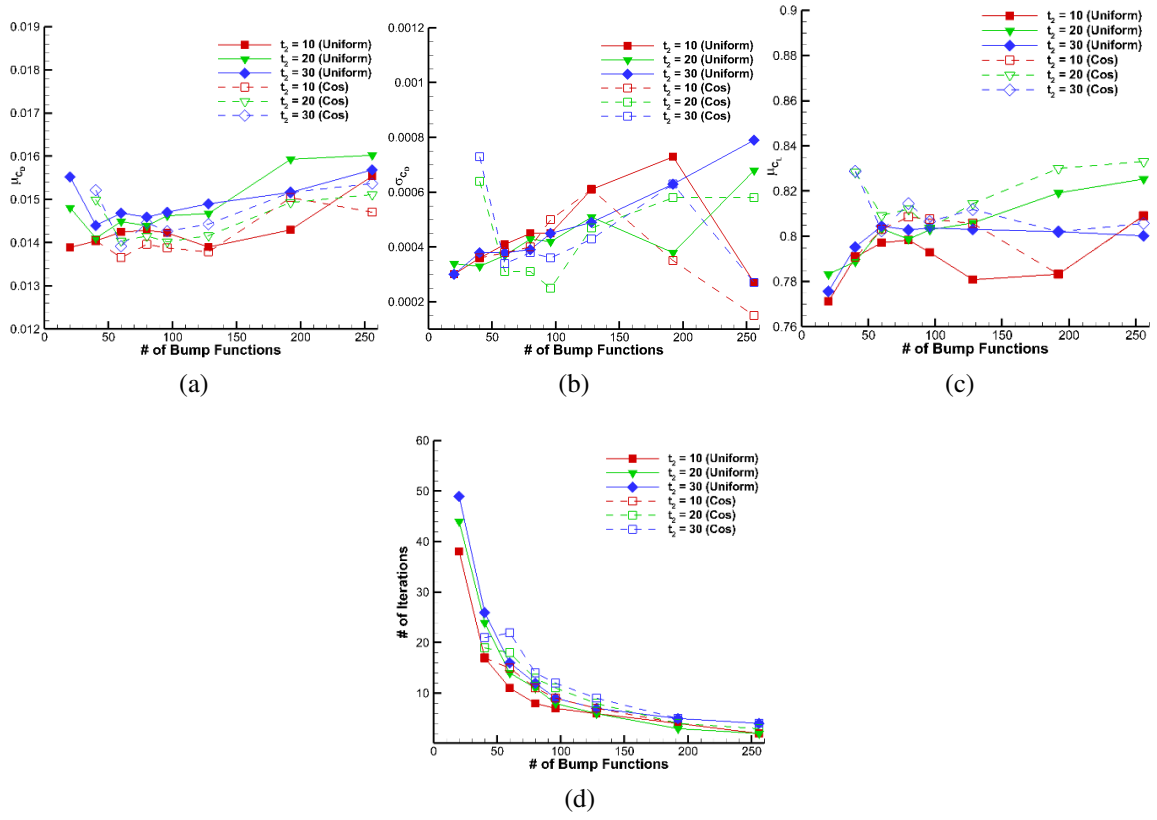


Figure 12. (a) $\mu_{C_D}$ vs. number of bump functions for UD and CoD (b) $\sigma_{C_D}$ vs. number of bump functions for UD and CoD (c) $\mu_{C_L}$ vs. number of bump functions for UD and CoD (d)The number of iterations to converge vs. number of bump functions for UD and CoD (For all plots, the function amplitude boundary is $[-0.1, 0.1]$).

Figure 13 presents the comparison of original and optimized (38bf and 40bf with UD) shapes. Both cases converged in 17 iterations. For the 38bf case, the mean and standard deviation of drag coefficient are 0.0139 and 0.00035 at $\alpha = 2.9378°$. The area of optimized shape is 0.0827 and the objective function is reduced from 3.4463 to 1.4210. For the 40bf case, the reduction in $\mu_{C_D}$ is 69 drag counts and $\sigma_{C_D}$ is 0.00036 at the same angle of attack. The area and the objective function of the optimized airfoil is 0.0819 and 1.4366 respectively. Based on these numerical results, since the mean and standard deviation of aerodynamic coefficients are approximately at the same level, the optimized shape airfoils are expected to be similar which is proven in Figure 13.

Surface pressure coefficient distribution of optimized shapes is very similar as presented in Figure 14. Instead of having a single weaker shock wave as observed for the deterministic optimum designs, the robust optimization procedure creates two weak shock waves, which is expected to decrease the drag coefficient under the variation of Mach number within the specified interval $[0.7253, 0.7427]$.

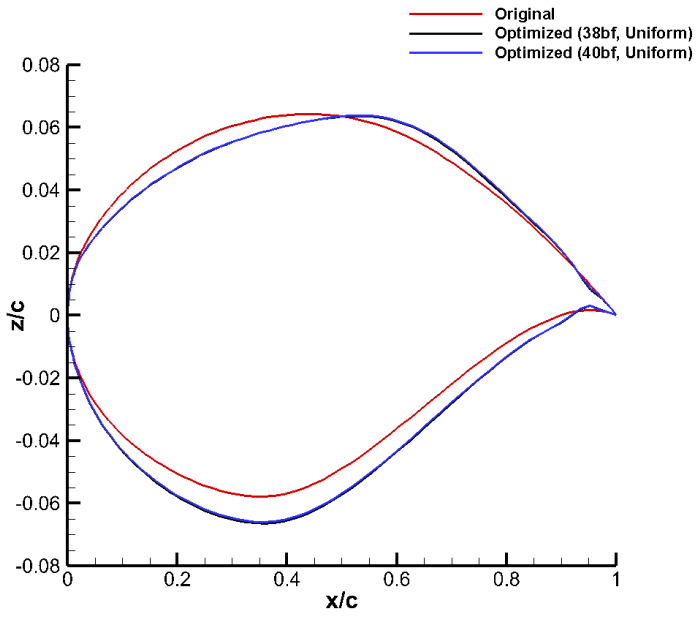


Figure 13. The comparison of original and optimized shapes (38bf and 48bf with UD).

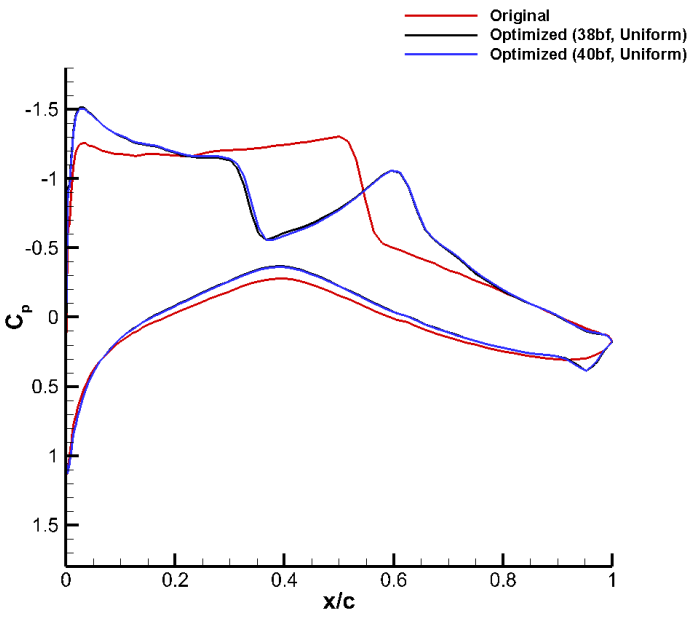


Figure 14. The $C_p$ comparison of original and optimized shapes (38bf and 48bf with UD).

Figure 15 presents the Mach number contours for the original and optimized shapes (38bf and 40bf) at $M = 0.7253$. As discussed for Figure 15, two weak shock waves can be seen where at $x/c = 0.3$ and 0.6. In deterministic optimization, the shock wave is weakened based on a single point (Mach number) optimization procedure. Differently, in robust design, the power of shock wave is separated into two due to the continuous multi-point nature of the optimization procedure.

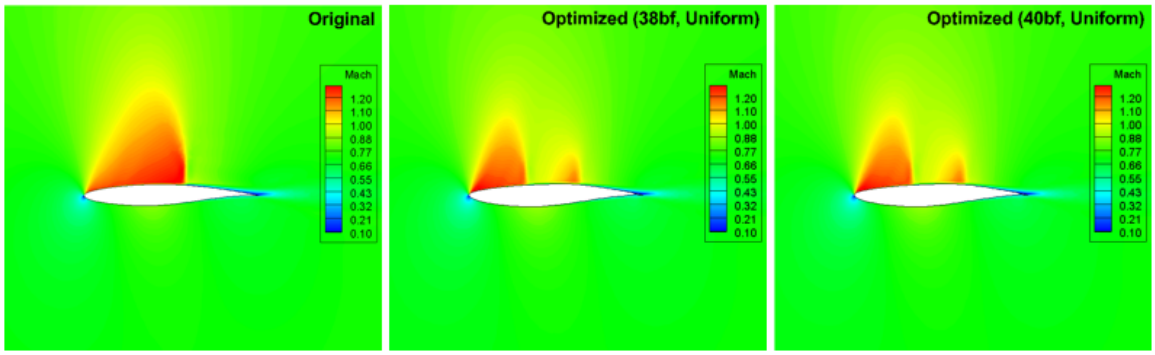


Figure 15. The contours showing Mach number over optimized (robust, 38bf and 40bf with UD) and original shape of RAE2822.

In Figure 16, the mean and standard deviation of drag coefficient, the number of iterations to converge and the mean of lift coefficient as a function of number of control points are presented for two distributions. With B-spline curve parameterization, the performance of optimization in terms of the mean and standard deviation of drag coefficient and the mean of lift coefficient decrease with the increase of control points. UD and CoD cases show similar trends in terms of robustness and mean measures. Similar to deterministic and robust (Hicks-Henne) design, the number of control points has high impact on computational cost.

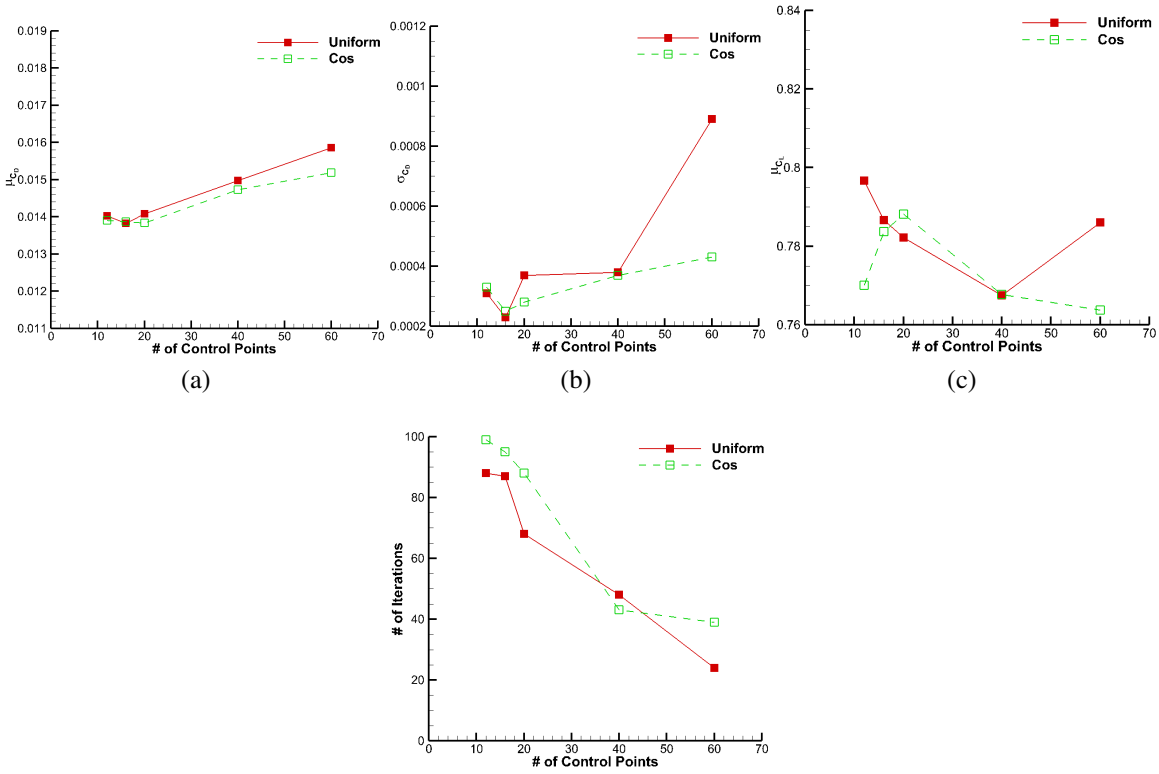


Figure 16. (a) $\mu_{C_D}$ vs. number of control points for UD and CoD. (b) $\sigma_{C_D}$ vs. number of control points for UD and CoD. (c) $\mu_{C_L}$ vs. number of control points for UD and CoD. (d) The number of iterations to converge vs. number of control points for UD and CoD.

Among B-spline parameterization robust design cases, cosine distributed 20cp is selected as the best case which reduced $\mu_{C_D}$ from 0.0209 to 0.0142, $\sigma_{C_D}$ from 0.0023 to 0.0003. $\mu_{C_L}$ constraint is integrated in objective function, therefore $\mu_{C_L}$ of optimized shape is 0.8058. The area of airfoil increases from 0.0778 to 0.0783 and the angle of attack for optimized shape is 3.3627°. This case converged in 69 iterations.

Figure 17 shows the comparison of original shape and optimized shapes for both parameterization techniques. The optimized shapes show significant difference based on the shape parameterization technique used. For the Hicks-Henne bump function case, optimized shape is thicker, however there is a deflection region similar to a flap close to the trailing edge. This may be due to the fact that the Hicks-Henne bump function can modify the surface where $x$ is in between 0.0001 and 0.9999.

The pressure distribution comparison of original and optimized shapes from both shape parameterization techniques at $M_{nominal}$ and $M_{max}$ can be seen in Figure 18. At both Mach number, the strength of shock wave is reduced at optimized shapes. The shock wave is weaken at $M_{nominal}$ more compared to the shock wave of optimized airfoil at $M_{max}$ that is directly related to performance of final design.

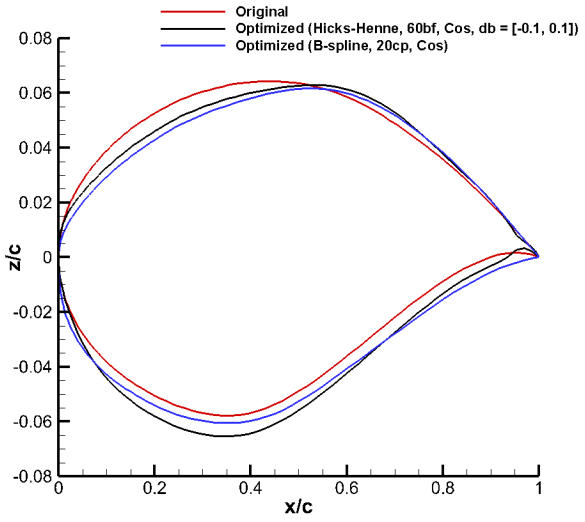


Figure 17. The comparison of original and optimized shapes (robust design).

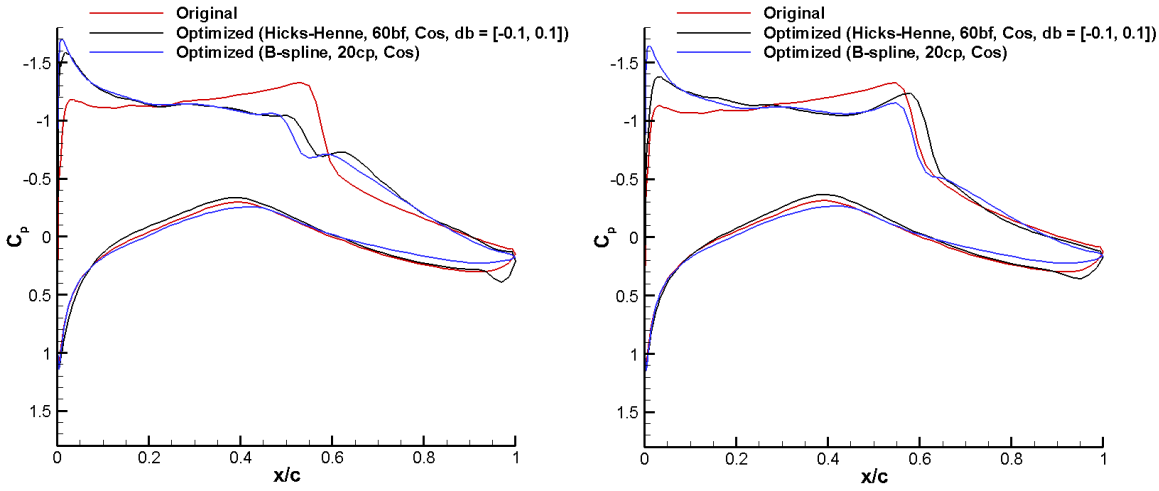


Figure 18. (a) The comparison of $C_p$ distribution of the optimal and original shape at $M_{nominal}$. (b) The comparison of $C_p$ distribution of the optimal and original shape at $M_{max}$.

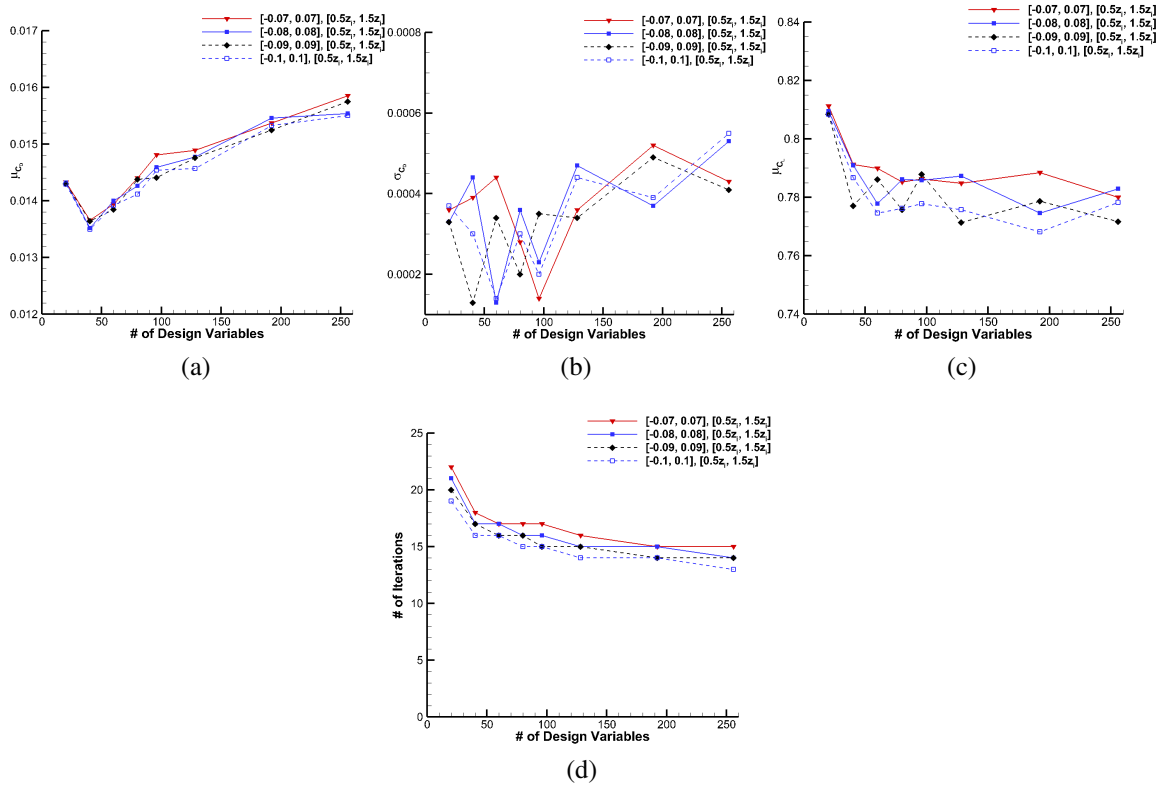


Figure 19. (a) $\mu_{C_D}$ vs. number of design variables. (b) $\sigma_{C_D}$ vs. number of design variables. (c) $\mu_{C_L}$ vs. number of design variables. (d) The number of iterations to converge vs. design variables. (The boundary interval of $[0.5z_i, 1.5z_i]$)

Figure 19 and 20 present the mean and the standard deviation of drag coefficient, the number of iterations to converge and the mean of lift coefficient under varying number of design variables with the boundary of each control point of $[0.5z_i, 1.5z_i]$ and $0.25z_i, 1.75z_i$, respectively. The cases with the lattice box of $2 \times 20$ and $2 \times 40$ have success in the reduction in $\mu_{C_D}$ and $\sigma_{C_D}$. The $\mu_{C_L}$ is smaller than $\mu_{C_{L_{Target}}}$, because the mean lift coefficient is implemented into the onjective function. The number of iterations to converge is smaller with the boundary of design variables of $0.25z_i, 1.75z_i$ than the boundary of design variables of $[0.5z_i, 1.5z_i]$. The computational cost in robust design is a significant parameter, therefore it has a vast efect on the selection of best case of FFD technique.

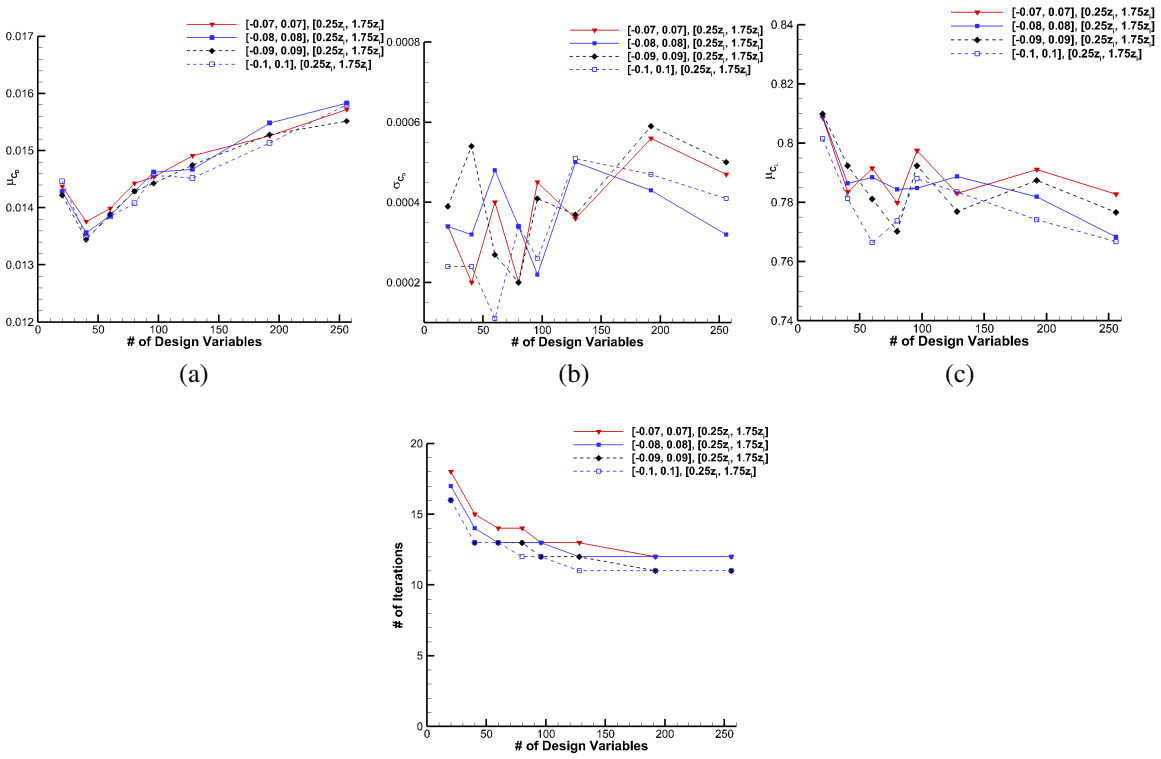


Figure 20. (a) $\mu_{C_D}$ vs. number of design variables. (b) $\sigma_{C_D}$ vs. number of design variables. (c) $\mu_{C_L}$ vs. number of design variables. (d) The number of iterations to converge vs. design variables. (The boundary interval of $[0.25z_i, 1.75z_i]$)

With Hicks-Henne parameterization technique, bump functions with CoD perform better in terms of $\mu_{C_D}$ and $\sigma_{C_D}$. Uniformly distributed bump functions with $t_2 = 10$ are advantageous in terms of computational cost. With B-spline technique, the number of control points has high impact on computational cost. In addition, the performance of optimization in terms of $\mu_{C_D}$ and $\sigma_{C_D}$ are similar at less number of control points. For robust optimization, CoD has high reduction in $\mu_{C_D}$ and $\sigma_{C_D}$ at both techniques. B-splines require more iterations to reduce $\mu_{C_D}$ to the same level as the one obtained with Hicks-Henne. Overall, Hicks-Henne is better compared to B-spline in terms of computational time and the performance of the final design.

## 3. ROBUST AND DETERMINISTIC OPTIMIZATION COMPARISON

In deterministic aerodynamic design, the airfoil shape was optimized to minimize the drag coefficient at a target $C_L$ for a certain Mach number with the angle of attack taken as a design variable, however the performance of optimized shape can significantly degrade if the Mach number deviates from its design point value in transonic flow. In robust aerodynamic design, the objective was to minimize the mean ($\mu_{C_D}$) and the variation of the drag coefficient ($\sigma_{C_D}$) at a target mean lift coefficient value ($\mu_{C_{L_{Target}}}$) to achive robustness in the performance to the variation of the Mach number in a specified range.

In Figure 21, the drag coefficient of the original, deterministic design (uniformly distributed 256bf) and robust design (cosine distributed 60bf and 20cp) under varying Mach number is presented. The interval of bump function amplitude is $[-0.01, 0.01]$ for deterministic and $[-0.1, 0.1]$ for robust design. Drag coefficient values of each shape are evaluated at the target $C_L$ value of 0.824. The $C_D$ of baseline RAE2822 shape is the highest at all Mach number values. The deterministic design is optimized at $M = 0.734$ and its $C_D$ is approximately 140 counts until $M = 0.7323$. At $M = 0.7357$ which is the closest to deterministic design point in the interval, there is a significant drop in $C_D$ and then significant rise with the increase of the Mach number. This trend clearly shows that

the deterministic optimization performs relatively poor at the off design Mach numbers. On the other hand, the airfoil obtained with the robust optimization approach exhibits a relatively flat $C_D$ over the Mach number range considered with a slight increase starting from $M = 0.7357$. The shape obtained with robust optimization (Hicks-Henne 60bf) achieves a 34 drag count reduction compared to deterministic design at $M = 0.7427$. Overall, robust design has better performance compared to deterministic design in terms of robustness and mean performance ($C_D$) at each Mach number.

In Figure 22, the comparison of original and optimized shapes for both deterministic and robust design is presented. For both designs, optimized shapes are similar in the vicinity of leading edge, however downstream of the half-chord, geometries differ vastly especially for the upper surface. Robust design provides high performance under the variation of Mach number that has a high impact on optimized shapes compared to deterministic design. Area constraint is satisfied with both designs.

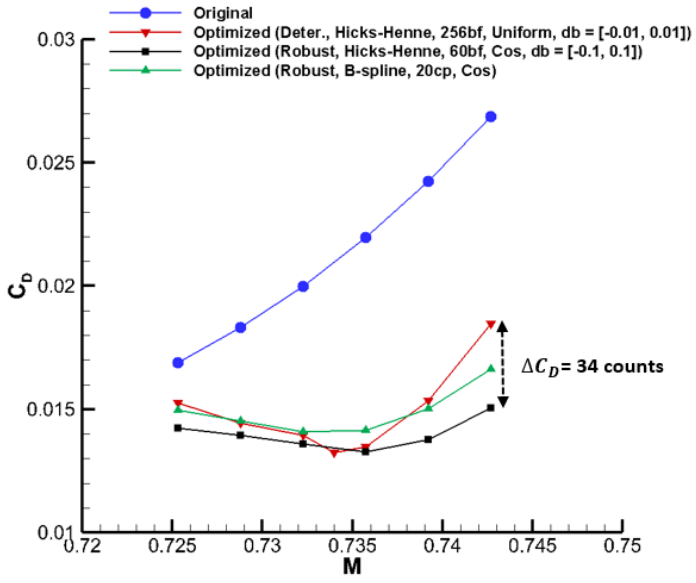


Figure 21. $C_D$ comparison of original, optimized (deterministic and robust) under varying Mach number.

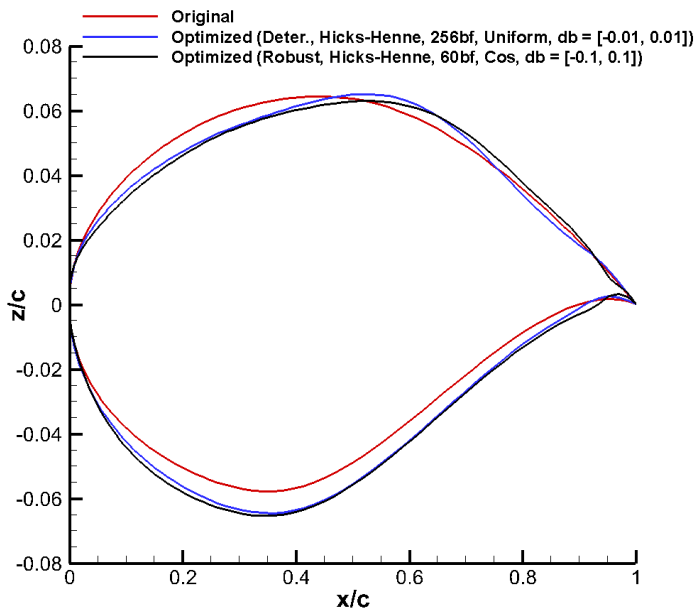


Figure 22. The comparison of original and optimized (deterministic and robust) shapes.

Figure 23 shows the Mach number contours over optimized (deterministic and robust) and original shape of RAE2822 at $M_{nominal}$ and $M_{max}$. The strength of the shock wave is reduced with both deterministic and robust designs. However, with robust design, the shock wave is weakened more compared to the deterministic design.

In Figure 24, the comparison of $C_p$ distributions of the optimal and original shapes at $M_{nominal}$ and $M_{max}$ is presented. These figures also verify the observations made from the contour plots presented above.

In both robust and deterministic optimization, the number of design variables (bump functions or control points) plays a significant role on computational time for each parameterization technique. The boundary conditions (limits) imposed at function amplitude is an important parameter for the lift and drag coefficients of optimized shape and the computational time when Hicks-Henne parameterization is used. In deterministic design of RAE2822 airfoil, B-spline parameterization with low number of control points (12, 16 and 20 uniformly distributed) and Hicks-Henne parameterization with uniformly distributed

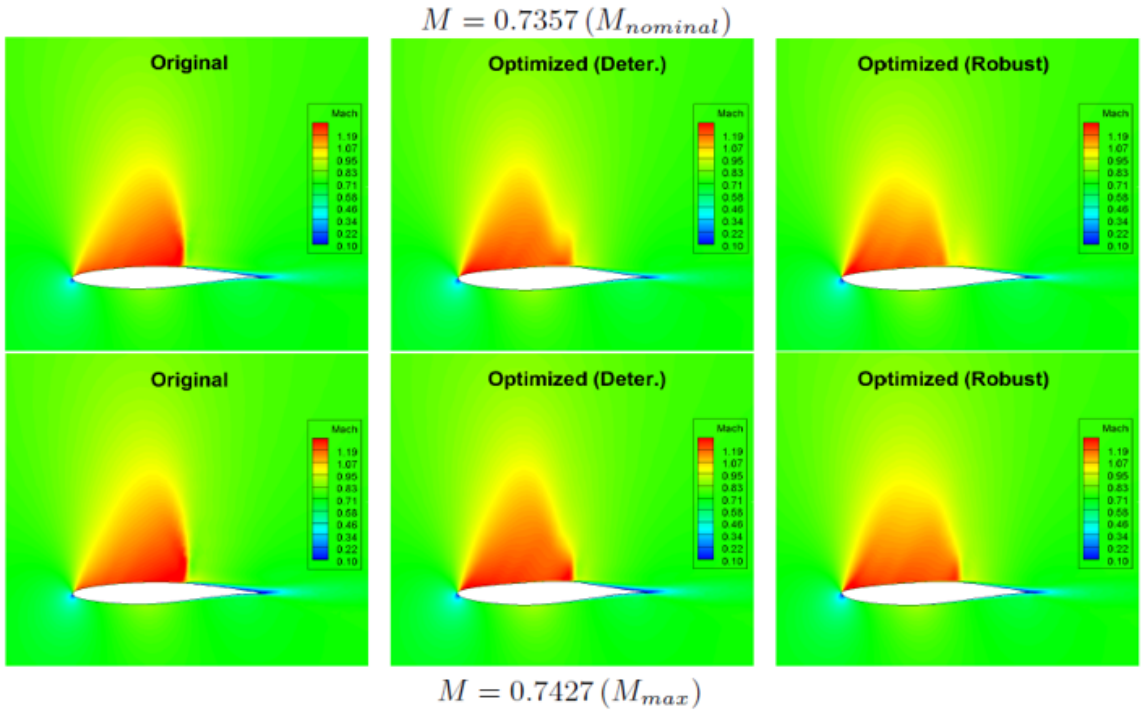


Figure 23. The contours showing Mach number over optimized and original shape of RAE2822.

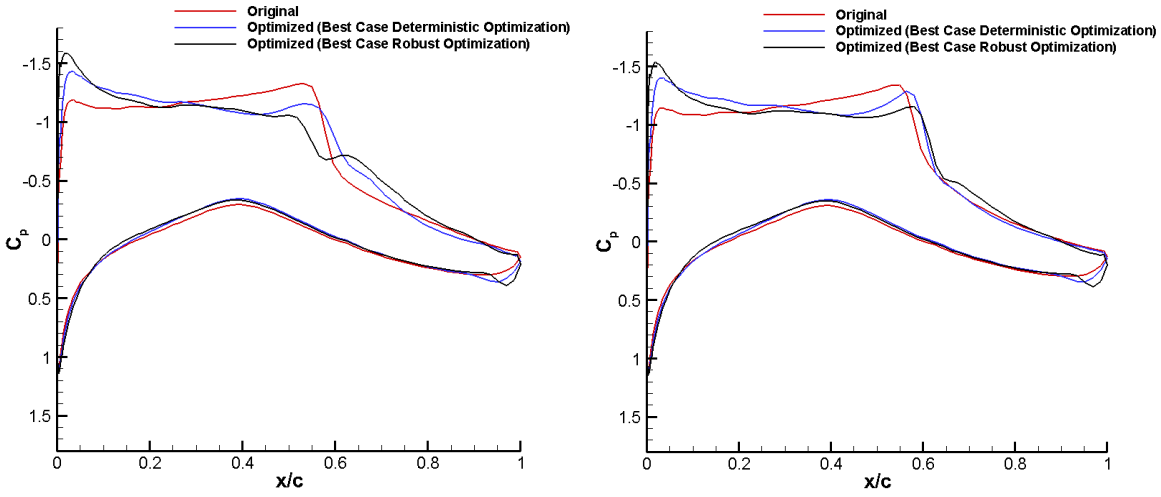


Figure 24. (a) The comparison of $C_p$ distribution of the optimal and original shape at $M_{nominal}$. (b) The comparison of $C_p$ distribution of the optimal and original shape at $M_{max}$.

function amplitude confined within the interval $[-0.01, -0.01]$ with $t_2 = 10$ are both efficient and accurate among all cases. Moreover, Hicks-Henne parameterization with large number of bump functions is found to be very efficient in terms of computational time.

In robust design, the cases with the number of bump functions between 20 and 128 show consistency in terms of the mean and standard deviation of drag coefficient for the Hicks-Henne parameterization. B-spline and Hicks-Henne bump function techniques provide better robustly optimized shapes with cosine distribution, when low number of design variables (control points or bump functions) are used. Similar to the deterministic design, the robust optimization shapes obtained with different shape parameterization techniques present different shapes because of the difference in shape parameterization methodology and constraints imposed in their implementation.

The results of the current study show that the number of design variables (control points or bump functions) and their distribution have impact on the computational cost and the aerodynamic performance metrics in both robust and deterministic design. In deterministic design, lower number control points for B-spline parameterization provides better optimum shapes, however the number of iterations to converge increases significantly. For Hicks-Henne parameterization, large number of bump functions is more effective, accurate and efficient. Uniform distribution provides better results in deterministic optimization however, cosine distribution is a better choice for robust design. Similar to deterministic design, lower number of control points for B-spline parameterization is more effective for robust design, however computational cost increases significantly. Hicks-Henne is a better technique in terms of computational cost and the performance of final design in robust design. Overall, the robust design provides better performance under the variation of Mach number.

# REFERENCES


[1] Huyse, L., "Free-form Airfoil Shape Optimization Under Uncertainty Using Maximum Expected Value and Second-order Second-moment Strategies," *NASA/CR-2001-21102*, ICASE Report No. 2001-18, NASA Langley Research Center, Hampton, Virginia, June 2001.

[2] Huyse, L., Padula, S. L., Lewis, M., and Li, W., "Probabilistic Approach to Free-Form Airfoil Shape Optimization Under Uncertainty," *AIAA Journal*, Vol. 40, No. 9, 2002, pp. 1764-1772.

[3] Vuruskan, A. and Hosder, S., "Investigation of the Effectiveness of Selected Shape Parameterization Techniques for Robust Aerodynamic Optimization", *35th AIAA Applied Aerodynamics Conference*, AIAA Aviation Forum, AIAA Paper 2017-4082, Denver, CO, June 2017.

[4] Oberkampf, W.L., Helton, J.C., Joslyn, C.A., Wojtkiewicz, S.F., and Ferson, S., "Challenge Problems: Uncertainty in System Response Given Uncertain Parameters," *Reliability Engineering and System Safety*, Vol. 85, No. 1-3, 2004, pp. 11-19.

[5] Swiler, L.P. , Paez, T., and Mayes, R., "Epistemic Uncertainty Quantification Tutorial," *Proceedings of the 27th International Modal Analysis Conference*, Society for Structural Mechanics, Orlando, FL, Feb. 2009.

[6] Helton, J.C., Johnson, J.D., and Oberkampf, W.L., "An Exploration of Alternative Approaches to the Representation of Uncertainty in Model Predictions", *Reliability Engineering and System Safety*, Vol. 85, No. 1-3, 2004, pp. 39-71.

[7] Park, G. J., Lee, T. H., Lee, K. H., and Hwang, K. H., "Robust Design: An Overview," *AIAA Journal*, Vol. 44, No. 1, 2006, pp. 181-191.

[8] Du, X. and Chen, W., "Efficient Uncertainty Analysis Methods for Multidisciplinary Robust Design," *AIAA Journal*, Vol. 40, No. 3, 2002, pp. 545-552.

[9] Nguyen, N. V., Lee, J. W., Tyan, M., and Lee, D., "Possibility-Based Multidisciplinary Optimisation for Electric-Powered Unmanned Aerial Vehicle Design," *The Aeronautical Journal*, Vol. 119, No. 1221, 2015, pp. 1397-1414.

[10] Nguyen, N. V., Lee, J. W., Lee, Y. D., and Park, H. U., "A Multidisciplinary Robust Optimisation Framework for UAV Conceptual Design," *The Aeronautical Journal*, Vol. 118, No. 1200, 2014, pp. 123-142.

[11] Hosder, S., Walters, R. W., and Balch, M., "Point-Collocation Non-Intrusive Polynomial Chaos Method For Stochastic Computational Fluid Dynamics", *AIAA Journal*, Vol. 48, No. 12, 2010, pp. 2721-2730.

[12] West T. and S. Hosder, "Uncertainty Quantification of Hypersonic Reentry Flows using Sparse Sampling and Stochastic Expansions," *Journal of Spacecraft and Rockets*, Vol. 52, No. 1, Special Section on Numerical Simulation of Hypersonic Flows, 2015, pp. 120-133.

[13] Schaefer J., West, T., Hosder, S., Rumsey, C., Carlson, J., and Kleb, W., "Uncertainty Quantification of Turbulence Model Closure Coefficients for Transonic Wall-Bounded Flows," *AIAA Journal*, Vol. 50, No. 1, 2016, pp. 195-213.

[14] Hicken, J. E. and Zingg, D. W., "Induced-Drag Minimization of Nonplanar Geometries Based on the Euler Equations," *AIAA Journal*, Vol. 48, No. 11, 2010, pp. 2564-2575.

[15] Mader, C. A. and Martins, J. R. R. A., "Stability-Constrained Aerodynamic Shape Optimization of Flying Wings," *Journal of Aircraft*, Vol. 50, No. 5, 2013, pp. 1431-1449.

[16] Lyu, Z. and Martins, J. R. R. A., "RANS-Based Aerodynamic Shape Optimization of a Blended-Wing-Body Aircraft," *21st AIAA Computational Fluid Dynamics Conference*, AIAA Paper 2013-2586, June 2013.

[17] Nielsen, E. J. and Anderson, W. K., "Aerodynamic Design Optimization on Unstructured Meshes Using the Navier–Stokes Equations," *AIAA Journal*, Vol. 37, No. 11, 1999, pp. 1411-1419.

[18] Jameson, A., Martinelli, L., and Pierce, N., "Optimum Aerodynamic Design Using the Navier–Stokes Equations,' *Theoretical and Computational Fluid Dynamics*, Vol. 10, No. 1-4, 1998, pp. 213-237.

[19] Park, G. J., Lee, T. H., Lee, K. H., and Hwang, K. H., "Robust Design: An Overview," *AIAA Journal*, Vol. 44, No. 1, 2006, pp. 181-191.

[20] Beyer, H.G. and Sendhoff, B., "Robust Optimization-A Comprehensive Survey," *Computer Methods in Applied Mechanics and Engineering*, Vol. 196, No. 33-34, 2007, pp. 3190-3218.

[21] Tang, Z. and Periaux, J., "Uncertainty Based Robust Optimization Method for Drag Minimization Problems in Aerodynamics," *Computer Methods in Applied Mechanics and Engineering*, Vol. 217, 2012, pp. 12-24.

[22] Padula, S. and Li, W., 2002, September. "Options for Robust Airfoil Optimization Under Uncertainty," *In 9th AIAA/ISSMO Symposium on Multidisciplinary Analysis and Optimization*, AIAA Paper 2002-5602, Atlanta, GA, Sep. 2012.

[23] Dodson, M. and Parks, G.T., "Robust Aerodynamic Design Optimization Using Polynomial Chaos," *Journal of Aircraft*, Vol. 46, No. 2, 2009, pp. 635-646.

[24] Padulo, M., Campobasso, M.S., and Guenov, M.D., "Novel Uncertainty Propagation Method for Robust Aerodynamic Design," *AIAA journal*, Vol. 49, No. 3, 2011, pp. 530-543.

[25] Peter, J.E. and Dwight, R.P., "Numerical Sensitivity Analysis for Aerodynamic Optimization: A Survey of Approaches," *Computers and Fluids*, Vol. 39, No. 3, 2010, pp. 373-391.

[26] Brezillon, J. and Dwight, R.P., "Applications of a Discrete Viscous Adjoint Method for Aerodynamic Shape Optimisation of 3D Configurations," *CEAS Aeronautical Journal*, Vol. 3, No. 1, 2012, pp. 25-34.

[27] Padron, A.S., Alonso, J.J., and Eldred, M.S., "Multi-Fidelity Methods in Aerodynamic Robust Optimization," *In 18th AIAA Non-Deterministic Approaches Conference*, AIAA Paper 2016-0680, San Diego, CA, Jan. 2016.

[28] Padula, S.L., Gumbert, C.R., and Li, W., "Aerospace Applications of Optimization Under Uncertainty," *Optimization and Engineering*, Vol. 7, No. 3, 2006, pp. 317-328.

[29] Huyse, L. and Lewis, R.M., "Aerodynamic Shape Optimization of Two-Dimensional Airfoils Under Uncertain Conditions," *Institute for Computer Applications in Science and Engineering*, NASA Langley Research Center, 2001.

[30] Reuther, J.J., Jameson, A., Alonso, J.J., Rimlinger, M.J., and Saunders, D., "Constrained Multipoint Aerodynamic Shape Optimization Using an Adjoint Formulation and Parallel Computers, Part 1," *Journal of Aircraft*, Vol. 36, No. 1, 1999, pp. 51-60.

[31] Chernukhin, O. and Zingg, D.W., "Multimodality and Global Optimization in Aerodynamic Design," *AIAA Journal*, Vol. 51, No. 6, 2013, pp. 1342-1354.

[32] Nemec, M., Zingg, D.W., and Pulliam, T.H., "Multipoint and Multi-objective Aerodynamic Shape Optimization," *AIAA journal*, Vol. 42, No. 6, 2004, pp. 1057-1065.

[33] Vassberg, J. C. and Jameson, A., "Influence of Shape Parameterization on Aerodynamic Shape Optimization," VKI Lecture III, April 9, 2014.

[34] Mousavi, A., Castonguay, P., and Nadarajah, S., "Survey of Shape Parameterization Techniques and its Effect on Three-Dimensional Aerodynamic Shape Optimization," *In 18th AIAA Computational Fluid Dynamics Conference*, AIAA Paper 2007-3837, Miami, FL, June 2007.

[35] Castonguay, P. and Nadarajah, S. K., "Effect of Shape Parameterization on Aerodynamic Shape Optimization," *In 45th AIAA Aerospace Sciences Meeting and Exhibit*, AIAA Paper 2007-59, Reno, NV, Jan. 2007.

[36] Song, W. and Keane, A. J., "A Study of Shape Parameterisation Methods for Airfoil Optimization," *In 10th AIAA/ISSMO Multidisciplinary Analysis and Optimization Conference*, AIAA Paper 2004-4482, Albany, NY, Aug. 31-Sept. 1, 2004.

[37] Leifsson, L. and Koziel, S., "Geometry Parameterization," *In Simulation-Driven Aerodynamic Design using Variable-Fidelity Models*, 1st ed., 2015, pp. 127-151.

[38] Kral, L. D., Mani, M., and Ladd, J. A., "Application of Turbulence Models for Aerodynamic and Propulsion Flowfields," *AIAA Journal*, Vol. 34, No. 11, 1996, pp. 2291-2298.

[39] Bardina, J. E., Huang, P. G., and Coakley, T. J., "Turbulence Modeling Validation," *28th Fluid Dynamics Conference*, June, 1997.

[40] Leifsson, L., Koziel, S., Tesfahunegn, A., Hosder, S., and Gramanzini, J., "Aerodynamic Design Optimization: Physics-Based Surrogate Approaches for Airfoil and Wing Design," *In 52nd Aerospace Sciences Meeting, AIAA SciTech Forum*, AIAA Paper 2014-0572, National Harbor, MD, Jan. 2014.

[41] Kumar, D., Miranda, J., Raisee, M., and Lacor, C., "Adjoint Based Multi-Objective Shape Optimization of a Transonic Airfoil Under Uncertainties," *5th International Conference on Engineering Optimization*, Iguassu Falls, Brazil, June 2016.

[42] Samareh, J. A., "A Survey of Shape Parameterization Techniques," *CEAS/AIAA/ICASE/NASA Langley International Forum on Aeroelasticity and Structural Dynamics*, pp. 333-344, 1999.

[43] Sripawadkul, V., Padulo, M., and Guenov, M., "A Comparison of Airfoil Shape Parameterization Techniques for Early Design Optimization," *13th AIAA/ISSMO Multidisciplinary Analysis Optimization Conference*, AIAA Paper 2010-9050, Fort Worth, Texas, Sep. 2010.

[44] Vassberg, J., "A Unified Baseline Grid About the Common Research Model Wing/Body for the Fifth AIAA CFD Drag Prediction Workshop," *In 29th AIAA Applied Aerodynamics Conference*, AIAA Paper 2011-3508, Honolulu, HI, June 2011.

[45] Vassberg, J., Dehaan, M., Rivers, M., and Wahls, R., "Development of a Common Research Model for Applied CFD Validation Studies," *In 26th AIAA Applied Aerodynamics Conference*, AIAA Paper 2008-6919, Honolulu, HI, August 2008.

[46] Lyu, Z., Kenway, G. K. W., and Martins, J. R. R. A., "Aerodynamic Shape Optimization Investigations of the Common Research Model Wing Benchmark," *AIAA Journal*, Vol. 53, No. 4, 2015, pp. 968-985.

[47] Yu, Y., Lyu, Z., Xu, Zelu and Martins J. R. R. A., "On the Influence of Optimization Algorithm and Initial Design on Wing Aerodynamic Shape Optimization,",*Aerospace Science and Technology*, Vol. 75, 2018, pp. 183-199.

[48] LeDoux, S. T., Vassberg, J. C., Young, D. P., Fugal, S., Kamenetskiy, D., Huffman, W. P., Melvin, R. G., and Smith, M. F., "Study Based on the AIAA Aerodynamic Design Optimization Discussion Group Test Cases, " *AIAA Journal*, Vol. 53, No. 7, 2015, pp. 1910-1935.

[49] Kenway, G. K. W. and Martins J. R. R. A., "Multipoint Aerodynamic Shape Optimization Investigations of the Common Research Model Wing," *AIAA Journal*, Vol. 54, No. 1, 2016, pp. 113-128.

[50] Lee, C., Koo, D., Telidetzki, K., Buckley, H., Gagnon, H., and Zingg, D. W., "Aerodynamic Shape Optimization of Benchmark Problems Using Jetstream," *53rd AIAA Aerospace Science Meetings*, AIAA SciTech Forum, AIAA Paper 2015-0262, Kissimmee, FL, Jan. 2015.

[51] Telidetzki, K., Osusky, L., and Zingg, D.W., "Application of Jetstream to a Suite of Aerodynamic Shape Optimization Problems," *In 52nd Aerospace Sciences Meeting*, AIAA Paper 2014-0571, National Harbor, MD, Jan. 2014.

[52] Lyu, Z., Kenway, G.K., and Martins, J., "RANS-Based Aerodynamic Shape Optimization Investigations of the Common Research Model Wing," *In 52nd Aerospace Sciences Meeting*, AIAA Paper 2014-0567, National Harbor, MD, Jan. 2014.

[53] Hicken, J. E. and Zingg, D. W., "Aerodynamic Optimization Algorithm with Integrated Geometry Parameterization and Mesh Movement," *AIAA Journal*, Vol. 48, No. 2, 2010, pp. 400-413.

[54] Gagnon, H. and Zingg, D. W., "Two-Level Free-Form Deformation for High-Fidelity Aerodynamic Shape Optimization," *12th AIAA Aviation Technology, Integration, and Operation (ATIO) Conference and 14th AIAA/ISSMO Multidisciplinary Analysis and Optimization Conference*, AIAA Paper 2012-5447, Indianapolis, IN, Sep. 2012.

[55] Palacios, F., Economon, T.D., Aranake, A.C., Copeland, S.R., Lonkar, A.K., Lukaczyk, T.W., Manosalvas, D.E., Naik, K.R., Padrón, A.S., Tracey, B., and Variyar, A., "Stanford University Unstructured (SU2): Open-Source Analysis and Design Technology for Turbulent Flows," *52nd Aerospace Sciences Meeting*, AIAA Paper 2014-0243, National Harbor, MD, Jan. 2014.

[56] Palacios, F., Colonno, M.R., Aranake, A.C., Campos, A., Copeland, S.R., Economon, T.D., Lonkar, A.K., Lukaczyk, T.W., Taylor, T.W., and Alonso, J.J., "Stanford University Unstructured (SU2): An Open-Source Integrated Computational Environment for Multi-Physics Simulation and Design," *51st AIAA Aerospace Sciences Meeting Including the New Horizons Forum and Aerospace Exposition*, AIAA Paper 2013-0287, Grapevine, TX, Jan. 2013.

[57] Jameson, A., Schmidt, W., and Turkel, E., "Numerical Solution of the Euler Equations by Finite Volume Methods using Runge-Kutta Time Stepping Schemes," AIAA Paper 1981-1259, 1981.

[58] AIAA Aerodynamic Design Optimization Discussion Group (2019, May 21). Retrieved from https://commonresearchmodel.larc.nasa.gov/.

[59] NASA Langley Research Center, "Turbulence Models," *Turbulence Modeling Resource* [online database], https://turbmodels.larc.nasa.gov/ [accessed 18 November 2019].

[60] Nee, V. W. and Kovasznay, L. S. G., "The Calculation of the Incompressible Turbulent Boundary Layer by a Simple Theory," *Physics of Fluids*, Vol. 12, 1968, pp. 473.

[61] Spalart, P. R. and Allmaras, S.R., "A One-Equation Turbulence Model for Aerodynamic Flows," *30th Aerospace Sciences Meeting and Exhibit*, 1992, pp. 439.

[62] Menter, F. R., "Two-Equation Eddy-Viscosity Turbulence Models for Engineering Applications," *AIAA Journal*, Vol. 32, No. 8, 1994, pp. 1598-1605.

[63] Menter, F. R., "Zonal Two-Equation k-w, Turbulence Models for Aerodynamic Flows," AIAA Paper 93-2906, 1993.

[64] Vuruskan, A. and Hosder, S., "Impact of Turbulence Models and Shape Parameterization on Robust Aerodynamic Shape Optimization," *Journal of Aircraft*, Vol. 56, No. 3, 2018, pp. 1099-1115.

[65] Carrier, G., Destarac, D., Dumont, A., Meheut, M., Din, I.S.E., Peter, J., Khelil, S.B., Brezillon, J., and Pestana, M., "Gradient-Based Aerodynamic Optimization with the elsA Software," *52nd Aerospace Sciences Meeting*, AIAA Paper 2014-0568, National Harbor, MD, Jan. 2014.

[66] Perez, R.E., Jansen, P.W., and Martins, J.R., "pyOpt: a Python-Based Object-Oriented Framework for Nonlinear Constrained Optimization", *Structural and Multidisciplinary Optimization*, Vol. 45, No. 1, 2012, pp.101-118.

[67] Wiener, N., "The Homogeneous Chaos", *American Journal of Mathematics*, Vol. 60, No. 4, 1994, pp. 897-936.

[68] Xiu, D. and Karniadakis, G.E., "Modeling Uncertainty in Flow Simulations via Generalized Polynomial Chaos," *Journal of Computional Physics*, Vol. 187, No. 1, 2003, pp. 137-167.

[69] Eldred, M.S., Webster, C.G., and Constantine, P.G., "Evaluation of Non-Intrusive Approaches for Wiener–Askey Generalized Polynomial Chaos," *10th AIAA Non-Deterministic Approaches Forum*, AIAA Paper 2008-1892, Schaumburg, IL, April 2008.

[70] Walters, R.W. and Huyse, L., "Uncertainty Analysis for Fluid Mechanics with Applications," No. ICASE 2002-1, NASA/CR-2002-211449, NASA Langley Research Center, Hampton, VA, Feb. 2002.

[71] Najm, H.N., "Uncertainty Quantification and Polynomial Chaos Techniques in Computational Fluid Dynamics," *Annual Review of Fluid Mechanics*, Vol. 41, 2009, pp. 35-52.

[72] Hosder, S. and Walters, R.W., "Non-Intrusive Polynomial Chaos Methods for Uncertainty Quantification in Fluid Dynamics," *48th AIAA Aerospace Sciences Meeting*, AIAA Paper 2010-0129, Orlando, FL, Jan. 2010.

[73] Eldred, M. S., "Design Under Uncertainty Employing Stochastic Expansion Methods," *International Journal for Uncertainty Quantification*, Vol. 1, No. 2, 2011, pp. 119-146.

[74] Hicks, R. M. and Henne, P. A., "Wing Design by Numerical Optimization," *Journal of Aircraft*, Vol. 15, 1978, pp. 407-412.

[75] Hicks, R. M., Murman, E. M., and G. N. Vanderplaats. "An Assessment of Airfoil Design by Numerical Optimization," *NASA TM X-3092*, Ames Research Center, Moffett Field, California, July 1974.

[76] Sederberg, T. W. and Parry, S. R., "Free-Form Deformation of Solid Geometric Models," *Computer Graphics*, Vol. 20, No. 4, 1986, pp. 151-160.

[77] Palacios, F., Economon, T. D., Aranake, A., Copeland, S. R., Lonkar, A. K., Lukaczyk, T. W., Manosalvas, D. E., Naik, K. R., Padron, S., Tracey, B., Variyar, A., and Alonso, J. J., "Stanford University Unstructured (SU2): Open-Source Analysis and Design Technology for Turbulent Flows," *52nd Aerospace Sciences Meeting*, AIAA SciTech Forum, AIAA Paper 2014-0243, National Harbor, MD, Jan. 2014.

[78] Economon, T. D., Alonso, J. J., Albring, T., and Gauger N. R., "Adjoint Formulation Investigations of Benchmark Aerodynamic Design Cases in SU2," *35th AIAA Applied Aerodynamics Conference*, AIAA Aviation Forum, AIAA Paper 2017-4363, Denver, CO, June 2017.

[79] Cook, P. H., McDonald, M. A., and Firmin M. C. P., "Aerofoil RAE 2822 Pressure Distributions, and Boundary Layer and Wake Measurements," AGARD Advisory Report No. 138, May 1979.

# VITA

Aslihan Vuruskan was born in Izmir, Turkey. After graduating from Izmir Atakent Anatolian High School in 2007, she began her undergraduate education at Istanbul Technical University in Istanbul. Aslihan was selected as a Co-op Intern at Turkish Aerospace Industry in 2009 and at TUSAS Engine Industry in 2011. She graduated Summa Cum Laude earning a Bachelor of Science Degree in both Aeronautical Engineering and Mechanical Engineering in 2012 and 2013, respectively. She worked as a Graduate Teaching and Research Assistant in the Department of Aeronautical Engineering in Istanbul Technical University,Turkey from 2013 to 2015. She continued her education earning a Master of Science degree in Aeronautical Engineering from Istanbul Technical University in 2014 and a Doctor of Philosophy in Aerospace Engineering from Missouri University of Science and Technology in May 2020. As a master's student, she received a scholarship from The Scientific and Technological Research Council of Turkey. As a doctoral student, she received the prestigious 2017 Amelia Earhart Fellowship from Zonta International Foundation and the 2019 AIAA Young Professionals Award from the St. Louis Section of the American Institute of Aeronautics and Astronautics (AIAA).